

**ANALYTICAL AND A NUMERICAL GROUND
RESONANCE ANALYSIS OF A CONVENTIONALLY
ARTICULATED MAIN ROTOR HELICOPTER**

Bernd Eckert

**Thesis presented at the Stellenbosch University
in partial fulfilment of the requirements for**

the degree of

Master of Science in Mechanical Engineering



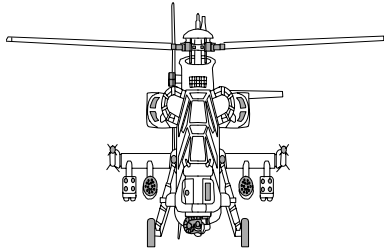
Supervisor:

Prof J.L. van Niekerk



March 2007

**ANALYTICAL AND A NUMERICAL GROUND
RESONANCE ANALYSIS OF A CONVENTIONALLY
ARTICULATED MAIN ROTOR HELICOPTER**



Master's Degree Research Project (MSc Engineering)

B. Eckert

March 2007

Mechanical Engineering Department

Stellenbosch University



Supervisor:

Prof J.L. van Niekerk

I, the undersigned, hereby declare that the work contained in this thesis is my own original work and has not previously, in its entirety or in part, been submitted at any university for a degree.

Signature:

Date:

Abstract

The helicopter is a prime example of a nonlinear multi-body dynamic system that is subjected to numerous forces and motions to which the system must react. When a helicopter, with a conventionally articulated rotor head, is resting on the ground with its rotor spinning, a condition called ground resonance can develop. Ground resonance is a specific self-excited oscillation of the helicopter and is caused by the interaction between the main rotor blades and the fuselage structure. Inertia forces of the blades perform an out-of-phase lagging motion, which reacts with the elastic landing gear of the helicopter. For certain values of the main rotor angular velocity, the frequency of these inertia forces coincides with a natural vibration frequency of the fuselage structure. If this occurs, the inertia forces of the lagging blades produce oscillations of the fuselage, which then further excite the lagging motion of the blades. This interaction is responsible for an instability of conventionally articulated main rotor helicopters, which is called ground resonance.

The ground resonance phenomenon is investigated by means of a classical analytical approach in which the ground resonance equations are derived from Euler-Bernoulli beam theory and verified with results in literature. These equations are required to discuss ground resonance stability in further detail and determine the specific regions in which the phenomenon occurs. These results are incorporated in a simplified numerical model using an elastic multiple-body dynamics analysis program called DYMORE to simulate the South African Rooivalk Combat Support Helicopter. DYMORE is a program that offers nonlinear multi-body dynamic analysis code, using the finite element method, which was specifically developed for helicopter modelling. The complexity of helicopter modelling generally requires large amounts of computing power to ensure reasonable processing time. In order to prevent excessive computational time, the numerical model will be simplified in terms of aerodynamic and structural aspects. The scope of the numerical investigation is, therefore, limited to the ground resonance phenomenon without the effect of aerodynamic forces and representing the fuselage as multi-body beam structures of specified stiffness.

The DYMORE analysis is used to investigate various circumstances in which battle damage from a single point failure (Vibration Isolation System inactive) to a multiple-point failure (Vibration Isolation System inactive, no tire damping and no shock absorber damping) may give rise to the ground resonance phenomenon. Both static and dynamic analyses are done on various components of the helicopter model to define operational conditions in which ground resonance occurs. The conditions are determined to be that the aircraft is operating at 5600 kg, main rotor speed 187 rpm, no Vibration Isolation System and no tire damping. Including no shock absorber damping aggravates the situation even further.

To model the fuselage more accurately and to reduce computational time, the Rooivalk model is redesigned in MSC ADAMS. This software package is a family of interactive motion simulation software developed to analyse the complex behaviour of mechanical assemblies. One of the sub-modules, ADAMS AIRCRAFT, can be used to build a complete, parameterized model of a new aircraft. The model templates provided by the software are based on fixed-wing aircraft and, therefore, new design templates for a helicopter airframe configuration are created. These templates are stored as subsystems that are subsequently combined into a full aircraft assembly.

A static analysis of the fuselage structure is performed to determine the uncoupled fuselage modes of vibration, which, when combined with the main rotor blade lag frequency, indicate the possible regions of ground resonance. The flexible beam elements that are required to model the blade are not available in the MSC ADAMS software package and need to be developed in a finite element model such as MSC NASTRAN and imported into ADAMS AIRCRAFT as modal neutral files. As the flexible beam elements cannot be developed or changed within the ADAMS AIRCRAFT software package, the main rotor blades are, initially, assumed to be rigid. They are modelled by nine beam elements, which are defined in terms of their mass and mass moments of inertia in a local axis system attached to the element. The local axis systems are defined by

construction frames that also define the blade twist of the main rotor blades. The beam elements are joined by fixed joints, which make the blades rigid.

The dynamic analyses performed on the full Rooivalk model with rigid blades subsequently show that the ground resonance phenomenon occurs between 275 rpm and 320 rpm, at an aircraft mass of 6258 kg, with the tire and shock absorber damping reduced to 0.001% of their fully operational value and the lead-lag damping in a single blade reduced by 20%. At 292 rpm rotor speed, the phenomenon is most pronounced. Further analyses, in which the lead-lag hinge on one of the main rotor blades is disturbed by a point torque resulting in a 0.5 rad/sec change in velocity of the blade, support the initial analyses.

Although the operational conditions for ground resonance, as predicted by the MSC ADAMS model, compare favourably with the aircraft manufacturer's prediction in terms of rotor speed (275 rpm) and main rotor blade lead-lag frequency (2.548 Hz or 16 rad/sec), an attempt is made to increase the accuracy of the blade modelling. This is done by replacing the fixed joints connecting the nine rigid beam elements with bushings. These bushings are, essentially, revolute joints for which stiffness characteristics can be specified. The stiffness characteristics, as specified for the original DYMORE blade model and the real rotor blade, are incorporated at the appropriate points of the blades where the nine beam elements join. This makes the blade semi-rigid with the same stiffness characteristics as the real blade defined at 0.777 m intervals. Various attempts at simulating the new rotor model prove to be unsuccessful as the simulation fails at balance simulation times of 6.9 seconds or less. The rotor blades deform unrealistically as MSC ADAMS assumes linear deformations. In order to simulate the nonlinear behaviour of the flexible rotor blade, it must be modelled with short flexible beams that must be developed in a separate finite element model. Highly accurate data regarding the blade construction and its material is required, which was not available at the time of this research project.



Opsomming

Die helikopter is 'n goeie voorbeeld van 'n nie-liniêre, dinamiese multiliggaamstelsel wat aan kragte en bewegings onderwerp word waarop die stelsel moet reageer. As 'n helikopter met 'n konvensioneel-geartikuleerde hoofrotorstelsel op die grond staan en die rotor draai, kan 'n toestand genaamd grondresonansie ontstaan. Grondresonansie is 'n spesifieke, selfopgewekte ossillasie van die helikopter wat veroorsaak word deur die interaksie tussen die hoofrotorstelsel en die lugraam. Die hoofrotorlemme se traagheidskragte veroorsaak 'n uit-fase volgbeweging wat die elastiese onderstel beïnvloed. By sekere waardes van die hoofrotoromwentelingsspoed stem die frekwensie van hierdie traagheidskragte met die natuurlike frekwensie van die helikopter se romp ooreen. Dit veroorsaak dat die nalopende beweging van die lemme die romp laat ossilleer, wat dan die naloopbeweging van die lemme verder vergroot. Hierdie interaksie tussen die helikopterrotor en -romp veroorsaak 'n onstabieliteit genaamd grondresonansie.

In hierdie studie word grondresonansie deur middel van 'n klassieke analise ondersoek waarin die bewegingsvergelykings deur middel van Euler-Bernoulli balkteorie herlei word. Hierdie vergelykings word gebruik om grondresonansie in verdere diepte te bespreek en om spesifieke omstandighede, wat hierdie verskynsel veroorsaak, te bepaal. Hierdie resultate word dan in 'n vereenvoudigde model van die Suid-Afrikaanse Rooivalk gevegshelikopter geïnkorporeer deur van 'n elastiese, multiliggaam, dinamiese ontledingsprogram (DYMORE) gebruik te maak. Alhoewel die DYMORE program spesifiek vir helikoptermodellering ontwikkel is, vereis die kompleksiteit van die model groot rekenaarberekeningsvermoëns om aanvaarbare verwerkingstye te verseker. Die numeriese model is daarom, in terme van lugdinamiese en strukturele aspekte, vereenvoudig ten einde oormatige berekeningstye te vermy. Die fokus van die numeriese ondersoek is aldus beperk tot die grondresonansieverskynsel met uitsluiting van die lugdinamiese kragte. Die romp word gemodelleer deur van multiliggaam balkstrukture, met gespesifiseerde styfhede, gebruik te maak.

Die DYMORE-analise word gebruik om verskillende omstandighede waar gevegskade, as gevolg van enkelpunt falings (Vibrasie Isolerings Stelsel gedeaktiveer) en meerpuntfalings (Vibrasie Isolerings Stelsel gedeaktiveer, geen banddemping en geen skokabsorbeerder-demping), tot grondresonansie kan lei, te ondersoek. Beide statiese en dinamiese analises word op verskeie komponente van die helikoptermodel uitgevoer om die bedryfsomstandighede waaronder grondresonansie voorkom, te simuleer. Daar word bepaal dat 'n helikopter met 'n gewig van 5600 kg, 'n hoofrotoromwentelingsspoed van 187 opm, Vibrasie Isolerings Stelsel gedeaktiveer en geen banddemping, tot grondresonansie lei. As die skokbreker demping verwyder word, vererger die grondresonansieverskynsel.

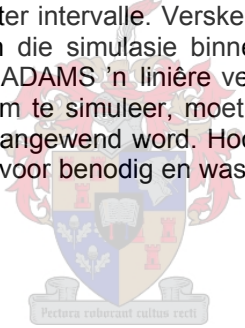
Om die vliegtuigromp meer akkuraat te modelleer en die berekeningstyd te verminder, word die Rooivalk model in MSC ADAMS herontwerp. Hierdie sagtewarepakket is 'n interaktiewe dinamiese simulasië program wat gebruik kan word om die komplekse gedrag van meganiese stelsels te simuleer. Een van die submodules, ADAMS AIRCRAFT, word gebruik om 'n volledige vliegtuigmodel te ontwikkel. Die modeltemplate wat deur die sagteware verskaf word, is gebaseer op vastevlerk vliegtuie en dit is dus noodsaaklik om template vir 'n helikopterlugraam van nuuts af te ontwerp. Die template word as substelsels geberg en dan in 'n volledige vliegtuigstelsel gekombineer.

'n Statische analise van die lugraamstruktuur word gedoen om die ontkoppelde lugraamvibrasie-modes te bepaal. Indien die frekwensies van hierdie modes gekombineer word met die hoofrotortraagheidsfrekwensie dui dit moontlike grondresonansiegebiede aan. Die buigbare balk-elemente wat benodig word om die hoofrotorlemme te modelleer is nie in die MSC ADAMS sagteware beskikbaar nie en moet dus met behulp van 'n eindige-element model soos MSC NASTRAN ontwikkel word en dan in die ADAMS AIRCRAFT sagteware, deur middel van modale-neutrale lêers, ingevoer word. Aangesien die buigbare balk-elemente nie in ADAMS AIRCRAFT ontwikkel of verander kan word nie, word die hoofrotorlemme as star benader. Hulle

word deur nege balkelemente wat deur hulle massa en massatraagheidsmomente, gekoppel aan 'n lokale assestelsel van die element, gedefinieer. Die lokale assestelsels word ook gebruik om die hoofrotorlemvervorming te beskryf. Die balk-elemente word deur vaste puntlaste aanmekaar geheg wat die rotorlem star maak.

'n Dinamiese analise op die volledige Rooivalk model met starre lemme toon aan dat 'n grondresonansieverskynsel teen 'n hoofrotoromwentelingsspoed van tussen 275 opm en 320 opm voorkom vir 'n vliegtuigmassa van 6258 kg, band- en skokbreker demping tot 0.001% van hulle oorspronklike waardes verminder en die lei-volgdemping in 'n enkele hoofrotorlem met 20% verminder. Teen 'n hoofrotoromwentelingsspoed van 292 opm kom die verskynsel die sterkste voor. Verdere analises waartydens die lei-volgs-karnier op een hoofrotorlem verstuur word deur 'n puntwringkrag wat 'n 0.5 rad/sek verandering in die lemsnelheid veroorsaak, ondersteun die oorspronklike analises.

Alhoewel die bedryfsomstandighede vir grondresonansie, soos voorspel deur die MSC ADAMS model, korreleer met die voorspellings van die vliegtuigvervaardiger, in terme van die hoofrotorlemspoed (275 opm) en die hoofrotorlem lei-volgfrequensie (2.548 Hz of 16 rad/sek), word gepoog om die akkuraatheid van die modellering te verbeter. Dit word bewerkstellig deur die vaste puntlaste wat die nege starre balk-elemente verbind te vervang met naafbusse. Hierdie busse is in essensie roterende laste waarvan die styfheidseienskappe gespesifiseer kan word. Die styfheidseienskappe word soos vir die oorspronklike DYMORE lem-model en die werklike rotorlem gespesifiseer en word by die toepaslike punte waar die nege balk-elemente heg, geïnkorporeer. Dit maak die hoofrotorlemme semi-star met dieselfde styfheidseienskappe as die werklike lem gedefinieer op 0.777 meter intervalle. Verskeie pogings om die nuwe rotormodel te simuleer was onsuksesvol aangesien die simulase binne 6.9 sekondes faal. Die rotorlemme vervorm onrealisties aangesien MSC ADAMS 'n liniêre vervorming aanvaar. Ten einde die nie-liniêre gedrag van 'n buigbare rotorlem te simuleer, moet kort, buigbare balke wat in 'n aparte eindige-element model ontwikkel is, aangewend word. Hoogs akkurate data ten opsigte van die lemkonstruksie en materiaal word hiervoor benodig en was, ten tye van hierdie navorsingsprojek, nie beskikbaar nie.



Dedicated to the loving memory of my father



Table of Contents

List of symbols.....	xi
List of figures.	xv
1. Introduction.....	1
1.1 Ground resonance.....	1
1.2 Ground resonance and the Rooivalk Combat Support Helicopter.....	2
1.3 Objective.....	3
1.4 Overview.....	4
2. Literature overview.....	5
2.1 Analytical approach.....	5
2.2 Numerical approach.....	6
2.3 Flight / ground testing.....	7
2.4 Recent developments.....	7
3. The theory of ground resonance.....	9
3.1 Introduction.....	9
3.2 Ground resonance equations.....	10
3.3 Ground resonance stability.....	34
3.3.1 Mathematical problem statement.....	34
3.3.2 Divergence stability.....	36
3.3.3 Uncoupled dynamics.....	37
3.3.4 Coupled dynamics.....	38
3.3.5 The no damping case.....	39
4. Numerical analyses with time domain simulation using a multi-body dynamics analysis program: DYMORE.....	48
4.1 General description of the DYMORE program.....	48
4.2 Detailed description of the DYMORE modules.....	48
4.2.1 The PREFEM module.....	48
4.2.2 The FEMANA module.....	49
4.2.3 The PSTFEM module.....	50
4.3 The Rooivalk Combat Support Helicopter model.....	50
4.3.1 The fuselage model.....	50
4.3.2 The rotor model.....	51
4.4 Rooivalk data for the PREFEM module.....	51
4.4.1 Global control parameters for the pre-processor.....	51
4.4.2 Global nodal co-ordinates, triads and boundary conditions.....	52
4.4.2.1 Global co-ordinates.....	52
4.4.2.2 Triads.....	52
4.4.2.3 Boundary conditions.....	53
4.4.3 Blade element definition.....	53
4.4.4 Rigid body definition.....	53
4.4.5 Prescribed displacement definition.....	53
4.4.6 Revolute joint definition.....	53
4.4.7 Time integration control parameters.....	54
4.4.8 Harmonic and user-defined time functions.....	54
4.4.8.1 Harmonic time functions.....	54
4.4.8.2 User-defined time functions.....	54
4.4.9 Dead loading cases definition.....	54
4.4.10 Gravitational forces definition.....	55
4.4.11 Elastic body definition – constant rigid body angular motion.....	55
4.4.12 Nonlinear spring and / or damper definition and properties.....	55

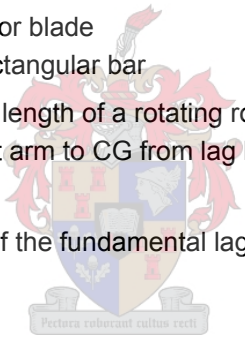
4.4.13 Cross-section definition.....	57
4.5 Static analyses of the Rooivalk model.....	58
4.5.1 The rotor.....	58
4.5.2 The fuselage.....	58
4.5.3 Comparison of uncoupled fuselage and blade frequencies.....	61
4.6 Dynamic analyses of the Rooivalk model.....	63
4.6.1 Lower static line analysis.....	63
4.6.2 Analysis with one lead-lag damper inoperative.....	64
4.6.3 Analysis with no vertical tire damping.....	65
4.6.4 Analysis with no vertical tire damping and no shock absorber damping.....	66
4.7 Summary of DYMORE analysis.....	68
5. Numerical analysis with interactive motion simulation software: MSC ADAMS.....	69
5.1 General description of the MSC ADAMS software.....	69
5.2 ADAMS / AIRCRAFT.....	69
5.2.1 Rooivalk fuselage model.....	69
5.2.1.1 Tail landing gear single post suspension template.....	69
5.2.1.2 Main landing gear trailing arm suspension template.....	70
5.2.1.2.1 Main landing gear main strut.....	70
5.2.1.2.2 Main landing gear trailing arm.....	70
5.2.1.2.3 Main landing gear shock absorbers.....	71
5.2.1.2.4 Main landing gear joints.....	71
5.2.1.2.5 Main landing gear sub-frames.....	71
5.2.1.2.6 Main landing gear communicators.....	71
5.2.1.3 Rigid fuselage template.....	72
5.2.1.4 Full fuselage assembly.....	72
5.2.2 Static analysis of the MSC ADAMS fuselage model.....	72
5.2.2.1 Modifications to the rigid fuselage.....	72
5.2.2.2 Modes of vibration.....	73
5.2.3 MSC ADAMS main rotor model.....	75
5.2.3.1 Main rotor hub.....	75
5.2.3.1.1 Hard points.....	75
5.2.3.1.2 Construction frames.....	76
5.2.3.1.3 General parts.....	76
5.2.3.1.4 Attachments and communicators.....	76
5.2.3.2 Main rotor blade.....	76
5.2.4 Dynamic analysis of the full Rooivalk model with rigid blades.....	77
5.2.5 Refinement of the MSC ADAMS main rotor model.....	78
6. Conclusions and recommendations.....	80
6.1 Conclusions.....	80
6.2 Recommendations.....	82
List of references.....	83
Appendix A DYMORE Rooivalk fuselage model.....	86
Appendix B DYMORE Rooivalk rotor model.....	87
Appendix C Rooivalk information sheet.....	88
Appendix D Rooivalk tail landing gear shock absorber.....	89
Appendix E Rooivalk main landing gear structure.....	90
Appendix F Rooivalk rigid fuselage with tail wheel assembly.....	91

Appendix G	Rooivalk rigid fuselage assembly.....	92
Appendix H	ADAMS Rooivalk fuselage model (rigid rotor body) in equilibrium configuration.....	93
Appendix I	Rooivalk fuselage model mode shapes (DYMORE).....	94
Appendix J	Rooivalk fuselage model in balance position (Denel data).....	95
Appendix K	Rooivalk fuselage mode shapes (Denel data).....	96
Appendix L	MSC ADAMS main rotor hub.....	97
Appendix M	MSC ADAMS main rotor.....	98
Appendix N	ADAMS AIRCRAFT Rooivalk model.....	99
Appendix O	Dynamic analysis of ADAMS AIRCRAFT Rooivalk model with rigid blades rotating at 275 rpm with no lead-lag disturbance.....	100
Appendix P	Dynamic analysis of ADAMS AIRCRAFT Rooivalk model with rigid blades rotating at 275 rpm with no lead-lag disturbance, no VIS, 0.001% total landing gear tire and shock absorber damping and a 20% decrease in lead-lag damping.....	103
Appendix Q	Dynamic analysis of ADAMS AIRCRAFT Rooivalk model with rigid blades rotating at 250 rpm with no lead-lag disturbance, no VIS, 0.001% total landing gear tire and shock absorber damping and a 20% decrease in lead-lag damping.....	104
Appendix R	Dynamic analysis of ADAMS AIRCRAFT Rooivalk model with rigid blades rotating at 350 rpm with no lead-lag disturbance, no VIS, 0.001% total landing gear tire and shock absorber damping and a 20% decrease in lead-lag damping.....	105
Appendix S	Dynamic analysis of ADAMS AIRCRAFT Rooivalk model with rigid blades rotating at 320 rpm with no lead-lag disturbance, no VIS, 0.001% total landing gear tire and shock absorber damping and a 20% decrease in lead-lag damping.....	106
Appendix T	Dynamic analysis of ADAMS AIRCRAFT Rooivalk model with rigid blades rotating at 292 rpm with no lead-lag disturbance, no VIS, 0.001% total landing gear tire and shock absorber damping and a 20% decrease in lead-lag damping.....	107
Appendix U	Lead-lag disturbance of main rotor blade by a 45 kN-meter point torque lead-lag disturbance.....	108
Appendix V	Dynamic analysis of ADAMS AIRCRAFT Rooivalk model with rigid blades rotating at 275 rpm with a 45 kN-meter point torque lead-lag disturbance.....	109
Appendix W	Dynamic analysis of ADAMS AIRCRAFT Rooivalk model with rigid blades rotating at 292 rpm with a lead-lag disturbance of main rotor blade by a 45kN-meter point torque, no VIS, 0.001% total landing gear tire and shock absorber damping and a 20% decrease in lead-lag damping.....	112

List of Symbols

a	width of a rectangular beam cross-section
a_i	amplitude of a harmonic $h_i(t)$ in the harmonic time function definition of DYMORE software package
A	cross-sectional area of a shock absorber piston
b	number of rotor blades
CA	centripetal acceleration on a rotating rotor blade element
c_{c_i}	critical damping value for the mode q_i
c_{ii}	modal damping
$CHEB_i$	i th coefficient of the i th Chebyshev polynomial
$CHEBPOL_i$	i th Chebyshev Polynomial
dx	length of an element of a single helicopter rotor blade
E	Young's modulus
EI_z	flexural stiffness about the z-axis
f/a	nozzle area of an orifice in a hydraulic damper
f	rotor blade lag frequency in rotating co-ordinates
$f1$	rotor blade lag frequency in fixed co-ordinates
$f2$	rotor blade lag frequency in fixed co-ordinates
$f(t)$	harmonic time function of DYMORE software package
$f_x(x)$	force on a rotating rotor blade element arising from the rotation of the blade
$f_y(x,t), f_{yR}$	external loading on a rotating rotor blade element
F_d	damping force in a hydraulic shock absorber
F_{dMLG}	damping force in a main landing gear shock absorber
F_{dTLG}	damping force in a tail landing gear shock absorber
F_{el}	elastic force in a spring
F_i	function value at i th point of the user defined time function of DYMORE software package
F_{vi}	viscous force in a damper
G	shear modulus
g	gravitational acceleration
h	height of a rectangular beam cross-section
$h_i(t)$	i th harmonic in the harmonic time function definition of DYMORE software package
h_o	rotor blade lag hinge offset
H_x	effective hub load in the positive x-direction
H_y	effective hub load in the positive y-direction

H_{x_R}	hub load in the positive x_R -direction
H_{y_R}	hub load in the positive y_R -direction
I	rotor blade lag inertia about the drag hinge
I_{xx}	fuselage mass moment of inertia in the positive x-direction
I_{yy}	fuselage mass moment of inertia in the positive y-direction
I_{zz}	fuselage mass moment of inertia in the positive z-direction
I_z	moment of inertia about the z-axis
k_{ii}	modal stiffness
k_1	dimensionless constant used in the calculation of the twist angle of a rectangular beam
K	rotor blade lag hinge stiffness
K, K_1, K_2	Southwell coefficients
$I_b = \int_0^R mr^2 dr$	characteristic rotor inertia
L, R	length of a rotor blade
L_B	length of a rectangular bar
m	mass per unit length of a rotating rotor blade
M_a	mass moment arm to CG from lag hinge of a rotor blade
$M_e = \int_0^R m\phi_e^2 dr$	modal mass of the fundamental lag mode
$m_b = \int_0^R mdr$	blade mass
m_{ii}	modal mass
$M, M+dM$	bending moments acting on a rotating rotor blade element
M_{fx}	effective fuselage modal mass in pitch at the hub
M_{fy}	effective fuselage modal mass in roll at the hub
n	blade index number
N	number of harmonics in the harmonic time function definition of DYMORE software package
$NCHEB$	number of Chebyshev polynomials
p	pressure exerted on a fluid in a hydraulic shock absorber
q	generalised co-ordinate
q_i	modal response of the i th natural vibration mode of the fuselage
Q_e	generalised external loading of the mode ϕ_e
Q_i	generalised force of the mode q_i
\bar{r}	position vector of a point on a rotor blade in the inertial space



\mathbf{r}	position vector of a point on a rotor blade in the rotating reference frame
s	Laplace variable
$s = \int_0^R m \phi_e dr$	first moment of lag mode
s_{el}	stretch of a spring
s_1	eigenvalue correction factor for small S_ξ
s_{1R}	eigenvalue of uncoupled (shaft fixed) lag motion
s_{NR}	eigenvalues of cyclic lag modes in the non-rotating frame
S_ξ	coupling parameter
\dot{s}	stretch rate of a damper
t	time
t_i	time at i th point of the user defined time function of DYMORE software package
$t^* = \Omega t$	dimensionless time variable
$T, T+dT$	axial forces tangential to the displaced blade reference line
T_i	period of a harmonic $h_i(t)$ in the harmonic time function definition of DYMORE software package
T_o	torque applied to a rectangular beam
u_{CHEB}	non-dimensional stretch of a spring in a Chebyshev approximation
u	displacement of the rotor hub in the x-direction
\ddot{u}_{hR}	component of the rotor hub acceleration \ddot{u} in the x_R -direction
u_i	contribution of the i th mode to the displacement of the hub, u (in the x-direction)
v	hub displacement in the y-direction
v_{CHEB}	non-dimensional stretch rate of a damper
\ddot{v}_{hr}	hub acceleration in the y-direction
v_i	contribution of the i th mode to the displacement of the hub, v (in the y-direction)
v_j	first fuselage roll mode on its undercarriage
$v(x,t), v_R$	lead-lag displacement of a rotating rotor blade element
$V, V+dV$	shear forces acting on a rotating rotor blade element
w	velocity of a piston in a hydraulic damper
x	space variable
x^*	specific point on a rotor blade
x_R	x-component of a position vector of a point on a rotor blade in the rotating reference frame

XH	upper bound of Chebyshev approximation
XL	lower bound of Chebyshev approximation
γ	specific gravity
θ_i	phase of a harmonic $h_i(t)$ in the harmonic time function definition of DYMORE software package
ρ	density
ϕ	angle of twist of a rectangular beam
ϕ_e	first edgewise mode shape of a rotating rotor blade
ϕ_i	ith natural vibration mode of the fuselage
ϕ_{ihx}	ith natural vibration mode of the fuselage in the x-direction
ϕ_{ihy}	ith natural vibration mode of the fuselage in the y-direction
ν	Poisson's ratio
ν_x, ν_y	dimensionless support natural frequencies
ω_e	natural frequency of mode ϕ_e in the rotating reference frame
ω_i	uncoupled natural angular frequency of the ith natural vibration mode of the fuselage
ω_j	uncoupled natural frequencies of the roll mode of the fuselage
$\omega_x, \omega_y, \omega_c$	uncoupled natural frequency of the rotor support system
ω_0	dimensional lag frequency at zero rotational speed
Ω	constant rotor angular velocity in rad/s
Ωt	dimensionless time variable for constant rotational speed
ξ	lag degree of freedom of a rotating rotor blade
ξ_o, ξ_c, ξ_s	degrees of freedom describing the motion of the rotor in the non-rotating reference frame
ξ^j	degree of freedom of the jth blade in the rotating frame
$\psi_n = \frac{2\pi n}{b}$	azimuth position of nth blade ($n = 1$ to b)
ζ_e	damping ratio associated with the mode ϕ_e
ζ_i	modal damping ratio
ζ_j	modal damping ratio of the first fuselage roll mode on its undercarriage
$\frac{2\pi}{b}$	azimuthal spacing between rotor blades
$(\cdot), (\ddot{\cdot})$	first and second time derive of the quantity within the brackets
$'(\cdot), ''(\cdot)$	first and second non-dimensional time derive of the quantity within the brackets
$(\cdot)', (\cdot)''$	first and second spatial derivatives of the quantity within the brackets

List of Figures

- Figure 1.1.1** Dissymmetry of rotor blade velocity in forward flight
- Figure 1.1.2** Unstable motion of the rotor centre of gravity
- Figure 1.1.3** Rotor centrifugal force – fuselage natural frequency interaction
- Figure 1.1.4** Devastating effect of ground resonance
- Figure 3.2.1** Side view of a helicopter on the ground indicating the positive x-direction
- Figure 3.2.2** Top view of a helicopter on the ground indicating the positive x- and y-directions
- Figure 3.2.3** Forces and moments acting on a rotating rotor blade element
- Figure 3.2.4** Centripetal acceleration acting on a blade element
- Figure 3.2.5** Acceleration components of a blade in a non-rotating reference frame
- Figure 3.2.6** Degrees of freedom ξ_C and ξ_S describing the motion of the rotor in the non-rotating frame
- Figure 3.2.7** Position vectors of a point P on a blade in the inertial space and rotating reference frame
- Figure 3.2.8** Hub load components
- Figure 3.3.1** Coleman diagram of the ground resonance solution for an articulated rotor
- Figure 3.3.2** Southwell diagram of the uncoupled fuselage and main rotor blade frequencies
- Figure 4.5.2.1** First DYMORE fuselage mode of vibration
- Figure 4.5.2.2** Second DYMORE fuselage mode of vibration
- Figure 4.5.2.3** Third DYMORE fuselage mode of vibration
- Figure 4.5.2.4** Fourth DYMORE fuselage mode of vibration
- Figure 4.5.2.5** Fifth DYMORE fuselage mode of vibration
- Figure 4.5.3.1** Comparison of uncoupled fuselage and blade frequencies
- Figure 4.6.3.1** Translation of the rotor shaft attachment point (No Vibration Isolation System and no tire damping)
- Figure 4.6.3.2** Rotation of the lead-lag hinge on the first rotor blade (No Vibration Isolation System and no tire damping)
- Figure 4.6.4.1** Translation of the rotor shaft attachment point (No Vibration Isolation System, no tire damping and no shock absorber damping)
- Figure 4.6.4.2** Rotation of the lead-lag hinge on the first rotor blade (No Vibration Isolation System, no tire damping and no shock absorber damping)
- Figure 5.2.2.2** MSC ADAMS uncoupled fuselage and blade frequencies

1. Introduction

1.1 Ground Resonance

Ground resonance is a self-excited mechanical vibration phenomenon that can occur in any fully articulated rotor system that employs lead-lag hinges. These hinges allow the individual blades the freedom to move in the plane of rotation of the main rotor. Motion opposite to the direction of rotation is known as lagging while motion in the direction of rotation is known as leading. Individual blades are allowed to lead and lag in order to compensate for drag changes that occur when the rotor's blades flap due to asymmetry of lift in forward flight.

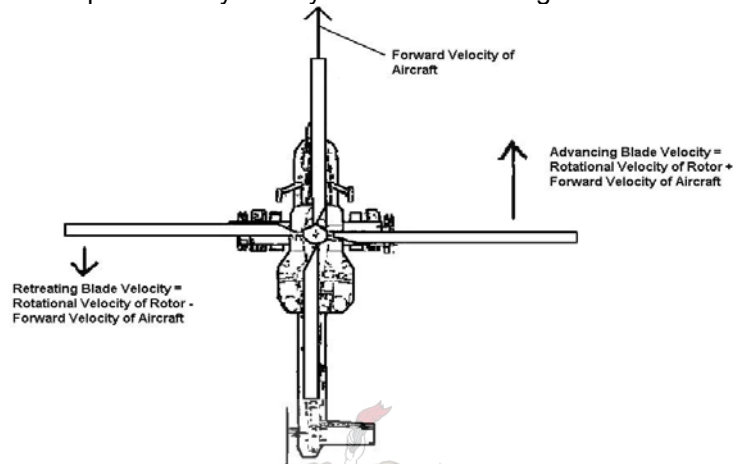


Figure 1.1.1 Dissymmetry of rotor blade velocity in forward flight

Figure 1.1.1 shows that in forward flight, the advancing blades are not only subjected to their rotational velocity but also to the forward velocity of the helicopter. These two velocities add to give the resultant velocity of the advancing blade. On the retreating blade the forward velocity of the helicopter acts opposite to the rotational velocity of the blade and the resultant velocity is the difference between the two velocities. The resultant velocity on the advancing blades is therefore much higher than on the retreating blades. As the amount of lift an aerofoil (or helicopter blade) can produce is directly proportional to the velocity of the flow across the blade, the advancing blade produces more lift than the retreating blade. This asymmetry of lift causes a difference in induced drag on the advancing and retreating blades causing them to move in their plane of rotation. This motion is damped by means of lead-lag dampers, which ensure that the centre of gravity of the blades remains inline with the rotor hub.

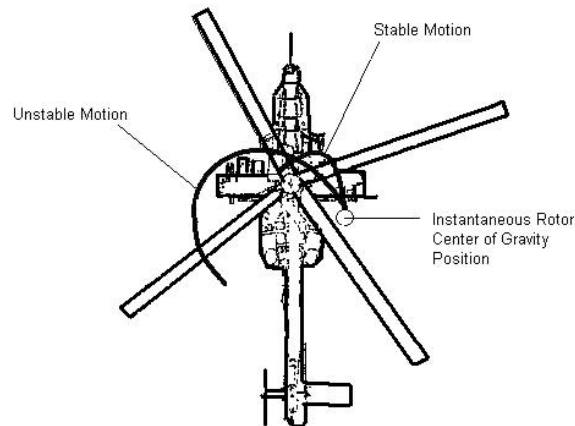


Figure 1.1.2 Unstable motion of the rotor centre of gravity

Figure 1.1.2 shows the situation where the lead-lag dampers cannot compensate for excess in-plane movement of the blades and the centre of gravity of the rotor blades is no longer aligned with the rotor hub. This is particularly dangerous when a helicopter is in contact with the ground. The misalignment of the rotor centre of gravity and the rotor hub generates an unbalanced centrifugal force at a specific frequency. Should this frequency be in phase with the natural frequency of the fuselage, the helicopter will start to rock on its landing gear (Figure 1.1.3).

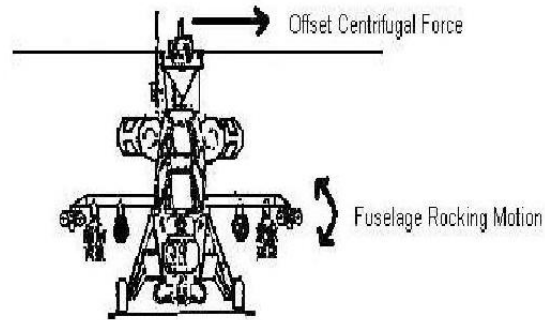


Figure 1.1.3 Rotor centrifugal force – fuselage natural frequency interaction

This fuselage frequency aggravates the unbalanced centrifugal force, which in turn aggravates the rocking motion. If unchecked, the mutually increasing excitation of the rotor and the fuselage (i.e. ground resonance) can lead to the destruction of the helicopter (Figure 1.1.4).



Figure 1.1.4 The devastating effect of ground resonance (Photo courtesy of John Fullerton and Ken Haan)

1.2 Ground Resonance and the Rooivalk Combat Support Helicopter (CSH)

The South African National Defence Force (SANDF) has, from past experience, come to realize the vital importance of a fully integrated, flexible, highly mobile and effective combat suite in the modern battle field scenario. For this reason, various mutually supportive, high mobility weapon systems have been developed to operate in medium to high threat environments and in high intensity operations. These systems include the G6 155-mm self-propelled gun, the Rooikat 105 wheeled armoured tank destroyer, the Ratel troop carrier, the Valkiri multiple rocket system and the Rooivalk Combat Support Helicopter.

Development of the Rooivalk CSH was initiated in 1976 when the initial project study was launched. One prototype, based on the airframe of an Alouette III, was built to demonstrate the feasibility and capability of local industry to build a tandem configuration helicopter. This prototype was known as the Alpha AH1 prototype. Concurrent with this development, local industry upgraded the Puma medium transport helicopter to what is now known as the Oryx medium transport helicopter. This upgrade included more powerful engines as well as upgraded gearboxes and drive trains, all of which would be invaluable for the future development of Rooivalk.

The attack helicopter program was approved in 1984 and over the following years, three Rooivalk prototypes were built: the XDM – Experimental Development Model, the ADM – Advanced Development Model and the EDM – Engineering Development Model. Although the three prototypes each had their specific role to play in the development cycle (XDM for structural testing, ADM for avionics testing as well as integration and EDM for weapons integration and aircraft qualification), they all contributed to the overall design drivers such as mobility, survivability, versatility and ease of use of the final product.

The production Rooivalk utilises a conventional semi-monocoque airframe construction of aluminium alloy and composite material as well as a conventional articulated main and tail rotor. The stepped tandem cockpits allow both the pilot, seated in the rear cockpit and the weapon systems operator, seated in the front cockpit, good all-round visibility. Dual redundancy and placement of mission critical equipment ensures good survivability while innovative features such as the Vibration Isolation System (VIS), contributes to crew comfort in all flight regimes.

The Vibration Isolation System isolates the fuselage from vibrations originating from the main rotor system. It is a passive system, which provides isolation from vertical, pitch and roll inputs at the blade passing frequency of the main rotor. Fuselage vibration without the system would typically reach 0.03 to 0.04 g. These are reduced to below 0.025 g when the system is fully operational. These low vibration levels not only ensure increased reliability of electronic equipment and crew comfort but also vastly reduce the possibility of ground resonance.

Any failure on the helicopter such as a failure of the VIS or damage to the main landing gear shock absorber (oleo strut) increases the possibility of ground resonance occurring. These two failure cases are considered during the qualification testing of a helicopter such as Rooivalk. Due to financial constraints, however, it is recognised practice to consider only single point failures during the qualification of an airborne platform. This means that a VIS failure and an oleo strut failure and their effect on ground resonance are considered separately and independently.

Due to the nature of operations and the role foreseen for Rooivalk, single point failures may not always be a reality. Battle damage can cause the failure of various systems or multiple components of a single system. As the VIS and the oleo struts are two critical components in the prevention of ground resonance, a failure of one or both must be considered to prevent the loss of an aircraft. It is therefore imperative to better understand the effect a single point failure (VIS) or multiple point failure (VIS and oleo strut) will have on the ground resonance characteristics of the Rooivalk CSH.

1.3 Objective

For most countries such as South Africa an extensive validation and qualification process for a newly developed aircraft is not possible due to financial constraints. Nevertheless, the Rooivalk CSH, being a newly developed combat helicopter system, must be qualified according to military as well as civilian standards. Due to cost implications, qualification of the Rooivalk cannot be done by flight testing alone. Extensive use of safety analyses, manufacturers' documentation, modelling and simulation must be used in the qualification process. Where possible, the analytical approach, the numerical approach and flight/ground testing are combined. Due to project commitments, financial milestones and time schedules, testing cannot continue indefinitely and

certain constraints are placed on the qualification process. An example of this is that aircraft failures are considered as single point failures alone. Very few multiple point failures are simulated or tested for qualification. Further investigation into multiple point failures during critical phases of flight such as landing, therefore needs to be investigated. This is particularly true when considering a multiple failure and its consequences in terms of ground resonance on the Rooivalk.

The objective of this research project is to investigate ground resonance by analytical and numerical means in circumstances where battle damage, such as a single point failure (Vibration Isolation System (VIS) inactive) or a multiple point failure (VIS inoperative and main landing gear oleo strut or tires damaged) may give rise to the ground resonance phenomenon.

1.4 Overview

As can be seen in section 1.1, ground resonance is caused by the interaction of the lagging motion of the helicopter's main rotor blades with a natural frequency of the structure supporting the rotor. To avoid ground resonance, lead-lag dampers are fitted to the lead-lag hinges on conventionally articulated main rotor helicopters of which the South African Rooivalk Combat Support Helicopter is a prime example. Although these dampers are effective in stabilizing the motion of the main rotor blades, there may be circumstances in which ground resonance can still occur. These circumstances may arise due to faulty maintenance of the lead-lag dampers or from a loss of damping in the landing gear shock absorbers due to battle damage. As ground resonance can be highly destructive, it is necessary to fully understand its causes. In chapter 3, the theory of ground resonance is discussed and the ground resonance equations are derived from Euler-Bernoulli beam theory in section 3.2. These equations are then used to discuss ground resonance stability in section 3.3. In chapter 4, a numerical analysis with time domain simulation, using a multi-body dynamics analysis program called DYMORE, is used to simulate the conditions in which ground resonance can occur on the Rooivalk model. Following a general and a detailed description of the DYMORE package in section 4.1 and 4.2, the construction of the Rooivalk fuselage and rotor is discussed in section 4.3. Section 4.4 describes the Rooivalk data required to run the static and dynamic analyses of section 4.5 and 4.6 while section 4.7 summarises the results of the DYMORE analyses. In order to model the fuselage more accurately and to reduce computational time, the Rooivalk model is re-designed in a new software package called MSC ADAMS as described in chapter 5. Following a general description of the MSC ADAMS software package in section 5.1, the construction of the Rooivalk fuselage model is discussed in section 5.2.1. The subsequent static analysis of the MSC ADAMS fuselage model is described in section 5.2.2 and is used to describe the modes of vibration in section 5.2.2.2. The construction of the MSC ADAMS main rotor model is described in section 5.2.3 and is combined with the fuselage model to perform dynamic analyses of the full Rooivalk model as described in section 5.2.4. The operational conditions in which ground resonance is encountered are also described in this section. Finally, conclusions and recommendations are presented in chapter 6.

2. Literature Overview

The fundamentals of vertical flight were understood well before the days of the Roman Empire, in that the ancient Chinese constructed “Chinese Tops”. Although only a toy, which consisted of a propeller on a stick, that was spun between the hands, the concept probably represented the first helicopter. The concept was taken further in the early and mid 1500’s when the Italian inventor Leonardo Da Vinci made drawings of theoretical vertical flight machines. These machines were impractical in their full-sized form as they lacked sufficient power plants. This problem was solved at the end of the 19th century with the invention of the internal combustion engine and by the beginning of the 20th century many pioneers experimented with and built full-sized models of various helicopter configurations.

One of the more important advances in the development of vertical flight was made by a Spanish engineer, Juan de la Cierva with the introduction of an articulated rotor head in an autogyro in 1923. Although this new innovation solved many problems, it created new ones as well. This became apparent in the first recorded ground resonance accident in the 1930’s when an autogyro hit a rock while taxiing. The accident attracted the attention of scientists, who eventually produced a mathematical and physical understanding of the phenomenon. They found that ground resonance could be prevented with damping and that the damping had to be applied to both the lead-lag hinges as well as the landing gear.

A full analytical analysis of the ground resonance phenomenon was done by two NASA flutter specialists, Robert Coleman and Arnold Feingold [1], who performed some of the earliest research in this field and laid the foundation for all the work that was to follow. Some of this follow-up work was done by Donham, Cardinale and Sachs [2], as well as Lytwyn, Miao and Woitch [3], who all considered both air and ground resonance. In addition, major contributions, in terms of hingeless and bearingless rotors were made by Bousman, Sharp, Ormiston [4], Hodges [5] and Dawson [6].

All of the early analyses involved various assumptions and simplifications, which resulted in linearized equations. These equations provided accurate frequency predictions but were limited in predicting the damping required to prevent ground resonance. This is particularly true for rotor systems that utilize elastomeric lag dampers, as these exhibit highly nonlinear response characteristics. In order to cater for damping as well as make ground resonance analysis and modelling more accurate, three different approaches have been followed in recent years. These approaches are the purely analytical approach, the numerical approach and physical flight / ground testing or experiments on actual aircraft. In general, the analytical and numerical approaches are combined to compliment each other, while aircraft testing is done where finances permit. The ideal situation is, of course, a combination of the three approaches.

2.1 Analytical Approach

Since Coleman and Feingold [1] laid the foundation for ground resonance analysis, various books, articles and publications have expanded on the subject. Early investigators such as Price [7] explained the properties of a helicopter that cause ground resonance and sought to establish stability criteria in which it was safe to operate. The properties that determine the stability criteria were taken to be fuselage damping, drag hinge offset, inter-blade spring stiffness, blade mass and angular velocity of the rotor. Many assumptions and simplifications were made in order to obtain analytical formulas that described the ground resonance phenomenon. Aerodynamic forces were omitted and other simplifications were generally related to the mechanical structure of the helicopter.

Researchers such as Ganiev and Pavlov [8] expanded the analysis by formulating the problem as an instability of motion of a mechanical system in conditions of nonlinear resonances by making use of nonlinear mechanics. Various phenomena were investigated in order to determine the conditions of stability.

The classical theory of ground resonance investigates the phenomenon only with two degrees of freedom. This is done by applying the dynamic parameters of the helicopter to the plane of rotation of the main rotor blades. This theory was extended by researchers such as Nahas [9] to include more degrees of freedom in order to make the analysis more realistic. Six degrees of freedom were utilized to determine the regions of instability and the theoretical results were verified on a dynamic model of a helicopter.

Making use of experiments and models to verify analytical solutions became more and more frequent and as the knowledge base of ground resonance became larger, less assumptions and simplifications were applied to the problem. Friedman [10], for example, completed an analytical study aimed at predicting the aeromechanical stability of a helicopter in ground resonance by including the aerodynamic forces acting on the helicopter. Theoretical results were, once again, compared to experimental results, which gave relatively accurate results.

Researchers, such as Tang [11], then began to concentrate on more realistic damping models in the landing gear and on the blades by making use of nonlinear dampers. Initially the lagging motion of each helicopter blade was assumed to be equal in amplitude and frequency in order to use a simplified analytical method to calculate the regions of ground resonance instability.

A radical improvement in the analysis of the ground resonance phenomenon was introduced by Bachau and Kang [12] by making use of a multi-body formulation for helicopter nonlinear dynamic analysis. In classical helicopter analysis, elastic bodies are represented in a local, rotating frame of reference, which involves separating rigid bodies and elastic motions. In the multi-body formulation, the total motion of all elastic bodies is referred to a single inertial frame. This approach allows for the development of computer models that can deal with complex multi-body configurations.

2.2 Numerical Approach

Improvement in computer technology in terms of processing speed and memory has made the computer the ideal tool for simulating the ground resonance phenomenon. The numerical approach is much cheaper than ground testing on a real aircraft and is less time consuming than the purely analytical approach. Complex structures and forces can relatively easily be modeled to represent the prevailing configuration and conditions in which ground resonance may occur.

When the United States Marine Corps decided to upgrade the capabilities of the AH-1W Super Cobra and UH-1N Huey in the late 1990's, the landing gear of both types of helicopters had to be redesigned to cope with the envisaged higher all-up weight during takeoff and landing. This would change the ground resonance characteristics of both aircraft. The excessive computational time required by the previously developed analytical software tool called "MS Dytran" precluded it as a design tool for this particular project. This led to the development of a skid landing gear dynamic analysis tool using a nonlinear hollow rectangular beam element representation, which reduced the computational time from 1 – 2 days to approximately 12 minutes. This tool, known as "LS-Dyna" allowed designers to optimize ground resonance frequency placements, while retaining the vertical stiffness requirements required for the upgraded aircraft [13].

Computer software is, however, not only utilized for aircraft upgrades, but also for flight testing and vibration analysis of in-service helicopters. As such, the Rotary Wing Directorate of the United States Naval Air Warfare Center developed a nonlinear model of the Navy's SH-60B helicopter, using a package called "Flightlab". A full dynamic model of the helicopter, including the control system, coupled dynamics of flexible rotor blades and landing gear dynamics was

implemented. The tool is used by the Naval Air Warfare Center flight test engineers for better planning of flight tests. Similarly, a dynamic finite element model involving about 60 000 degrees of freedom was developed and implemented in the United States Army's RAH-66 Comanche helicopter program in 1996. The model duplicated the vibrational characteristics of the actual aircraft very closely and was used to investigate vibration problems during the Comanche's flight test program [14].

Various other software packages are also used for vibration investigations on other helicopter types. These include "MAPLE" and "SIMULINK" for the full nonlinear simulation model of the H3 Sea King helicopter [15], "ADAMS" used by Westland Helicopters to further integrate their computer aided design and engineering [16], "ANSYS" used by the Canadian Aeronautics and Space Institute [17] and "DYMORE" developed by the Rensselaer Polytechnic Institute in Troy, New York, specifically for helicopter modelling [18].

2.3 Flight / Ground Testing

Although the numerical approach has many advantages in terms of cost, the complexity of helicopter vibrations places a large demand on computational power, which in turn often leads to excessive computational time. Furthermore, a model, no matter how accurate, cannot replace the real aircraft. It is for this reason that flight/ground testing will always remain an integral part of vibration analysis.

Investigation of the ground resonance phenomenon by flight-testing was initially the only means at researchers' disposal during the early days of helicopter development. A trial and error approach had to be adopted and researchers often learnt from very costly mistakes. Development of electronic instrumentation such as the oscillograph, however, made it possible for engineers to conduct research and find solutions to problems in a more controlled environment. In 1955 Ciastula and MacMahon [19] described one of the first test setups to investigate ground resonance. The test consisted of electromagnetic pickups feeding signals to an oscillograph.

As technology advanced more and more countries began to build research facilities, which incorporated test stands on which the physical rotor head, of the helicopter being investigated, could be tested. An example of such a facility was the research center of Brunswick, Germany [20]. The center made extensive use of wind tunnel testing to investigate ground resonance and the effect of dampers on the phenomenon.

Centers such as the one at Brunswick eventually evolved into highly sophisticated flight test centers capable of testing all aspects of helicopter flight. Nowhere has this become more obvious than in the TIGER dynamics validation program [21]. Various aspects from the main and tail rotor layout, aero-elastic and aeromechanical stability, vibrations surveys, rotor whirl tests, airframe shake tests to armament configurations were validated. All testing relating to rotor dynamics and vibration control were also completed. A validation program of such magnitude is extremely expensive, as are the facilities required to complete the validation process.

2.4 Recent Developments

As ground resonance testing on a full aircraft is so expensive, the present trend is to mainly verify numerical models with ground test data when required. This is made possible by powerful software packages that have been specifically developed for aircraft design and testing. The technological advances in terms of computing power and speed make modelling and analysis of helicopter ground resonance a viable alternative to actual, full aircraft testing. Since the late 1990's numerical ground resonance research has continued but the research done has changed its emphasis from understanding the causes and effects of ground resonance [22], [23], [24], [28] to investigating means of preventing this instability [25], [26], [27], [29], [30]. As the causes and

effects of ground resonance are well known, helicopter pilots are constantly reminded of this danger. Flight safety information journals [31] frequently discuss ground resonance to remind pilots that predicting ground resonance may be difficult and can have severe consequences. Two recent examples occurred in 2004 and 2005. In May 2004, a Seasprite helicopter aboard the New Zealand Navy frigate HMNZS Te Mana was destroyed due to ground resonance during a routine ground run. Damage to the aircraft was estimated at between 1.5 and 3 million dollars. On the 14th of December 2005 an Aerospatiale SA-319B, Alouette III helicopter, was also destroyed by ground resonance encountered during a landing attempt near Escalante, Utah, USA. Two passengers were seriously injured. As ground resonance can occur on any conventionally articulated main rotor helicopter, aviation authorities nowadays prescribe that ground resonance prevention on these helicopters must be shown either by analysis and test, by reliable service experience or by showing that a single failure will not cause ground resonance. These requirements are also applicable to a newly developed helicopter such as the Rooivalk and, therefore, the ground resonance phenomenon on this helicopter needs to be investigated.



3. The Theory of Ground Resonance

3.1 Introduction

Ground resonance is the term given to self-excited oscillations of increasing amplitude caused by the interaction of the lagging motion of the rotor blades with other modes of motion of the helicopter while it is on the ground. This phenomenon was first noticed after a drag hinge, permitting the blade to move in the plane of rotation of the rotor was introduced into the design of the helicopter's rotor hub.

Ground resonance can be seen as a dynamic instability involving the coupling of the blade lag motion with the in-plane motion of the rotor hub. This instability is characterised by a resonance of the frequency of the rotor lag motion and a natural frequency of the structure supporting the rotor. In other words, during natural vibrations of the rotor blades in the plane of rotation (relative to the drag hinges), which can arise from any impetus (wind gust, rough landing etc.), inertia forces appear in this plane. Being transmitted to the helicopter fuselage, they cause its vibration on the elastic landing gear. These inertia forces have a specific frequency, depending upon the natural frequency of the blade in the plane of rotation and the angular velocity of the rotor. The presence of the bilateral couple between vibrations of the helicopter and its blades can result in the helicopter becoming unstable at a certain angular velocity of the rotor rotation, i.e., the helicopter vibrations, once begun (as a consequence of some impetus), are not damped, but increase.

Although this might imply that ground resonance is a true resonance, it must be remembered that the phenomenon of ground resonance is in fact an instability and not a resonance. This is so because if one considers the rotor-fuselage system as a whole, there are no external excitation forces acting on this system. As the phenomenon of resonance requires external forces to be acting on a system, ground resonance cannot be classified as a true resonance. The forces taking part in the instability during ground resonance are in fact internal to the rotor-fuselage system, coming, in turn, from the fuselage and the rotor.

The hub in-plane motions are coupled with the cyclic lag modes, which correspond to lateral and longitudinal shifts of the net centre of gravity from the centre of rotation. Ground resonance is potentially very destructive and avoiding this instability is an important consideration in helicopter design. The basic requirement is that resonances of the support structure with the lag mode be kept out of the operating range of the helicopter. Generally, resonances above 120 percent normal operating speed or below 40 percent normal speed are acceptable [32 p. 668]. As the rotor has little energy at low speed, it is possible to accelerate through the low frequency resonances without a large amplitude motion occurring. In the normal operating speed range of the rotor it is, however, necessary to either avoid resonances or provide sufficient damping in the system to prevent any instability.

Before ground resonance was well understood, a helicopter design that was found to be prone to this phenomenon required extensive design modifications. This forced design engineers to work on the development of the theory of ground resonance and reliable methods of its calculation, which would permit selecting the characteristics of the structural members, determining the stability margin of the helicopter on the ground.

The classical ground resonance analysis considers four degrees of freedom. They are the longitudinal and lateral in-plane motion of the rotor hub, corresponding to the first fuselage pitch and roll modes, and the two cyclic lag degrees of freedom [32, p. 668]. Also, as the in-plane motion of the hub is the dominant factor in ground resonance and the main forces involved are structural and inertia forces, rotor aerodynamic forces play only a minor role and can therefore be neglected in the ground resonance analysis. Ignoring these forces still provides a good

description of the fundamental characteristics of ground resonance, and gives good numerical results, particularly for articulated rotors.

At present there is a theory of ground resonance which explains all the most important features of this phenomenon and permits calculating the design characteristics on which ground resonance depends. This theory arose as a result of numerous theoretical and experimental investigations of ground resonance carried out in various parts of the world. The classical theory of ground resonance is due to Coleman and Feingold [1], who established criteria, which enable unstable oscillations to be avoided.

3.2 Ground Resonance Equations

To derive the coupled lag and support equations of motion describing the ground resonance dynamics, consider a helicopter fuselage standing on the ground on its undercarriage, as indicated in the following figures:

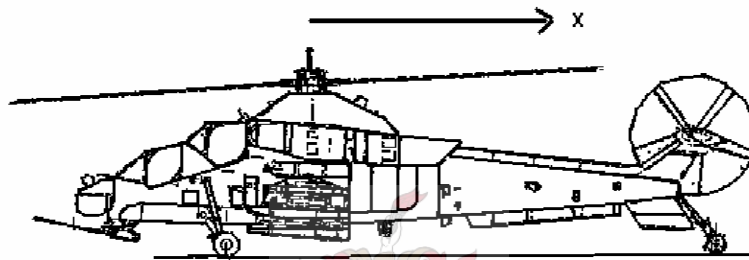


Figure 3.2.1 Side view of a helicopter on the ground indicating the positive x-direction

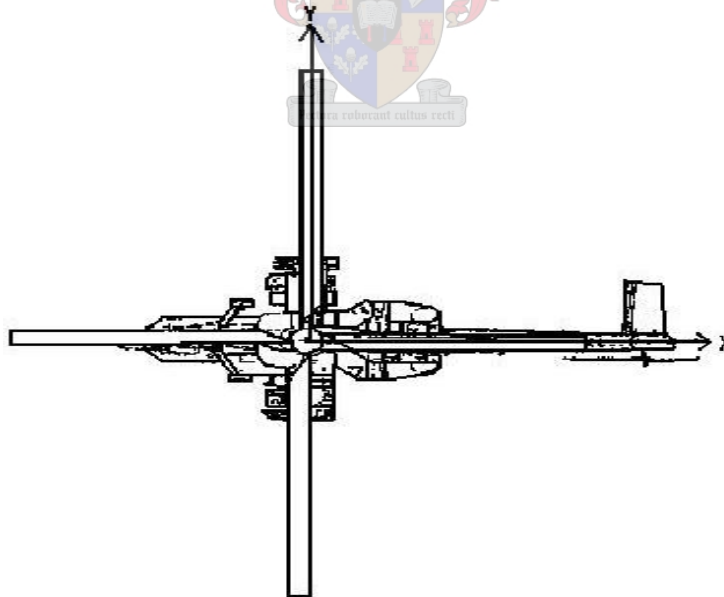


Figure 3.2.2 Top view of a helicopter on the ground indicating the positive x- and y-directions

Note: Although the rotor disc is included in figures 3.2.1 and 3.2.2, this is done solely to make the figures more understandable. Initially only the uncoupled fuselage dynamics, without the rotor will be considered.

From the mode summation method, the displacement of a specific structure under forces of excitation can be approximated by the sum of a limited number of normal modes of the system, multiplied by generalised co-ordinates. Generalised co-ordinates being a set of co-ordinates in which each co-ordinate is independent and the number of co-ordinates is just sufficient to completely specify the configuration of the system [33, p. 23]. The displacement of the rotor hub in the x-direction, u , may therefore be expressed as:

$$u = \sum_i \phi_{ihx} q_i \quad (1)$$

and the hub displacement in the y-direction, v , may be expressed as:

$$v = \sum_i \phi_{ihy} q_i \quad (2)$$

In these two expressions ϕ_i indicates the i th natural vibration mode of the fuselage, with the specific boundary condition, namely that the fuselage is resting on its undercarriage. The subscripts hx and hy indicate that the value of the i th mode shape at the hub, in the x - and y -directions respectively, is specifically being used. The modal response q_i of the i th mode is determined by its modal equation:

$$m_{ii} [\ddot{q}_i + 2\zeta_i \omega_i \dot{q}_i + \omega_i^2 q_i] = Q_i \quad (3)$$

where the notation $(\dot{})$ and $(\ddot{})$ represents the first and second time derive of the quantity within the brackets. This equation is obtained from the general equation of motion of the system by using the following quantities:

$$\omega_i = \sqrt{\frac{k_{ii}}{m_{ii}}} \Rightarrow k_{ii} = m_{ii} \omega_i^2$$

$$c_{c_i} = 2m_{ii} \omega_i$$

$$c_{ii} = c_{c_i} \zeta_i \Rightarrow c_{ii} = 2m_{ii} \omega_i \zeta_i$$

where m_{ii} is the modal mass, k_{ii} the modal stiffness, c_{ii} the modal damping and c_{c_i} the critical damping value for the mode. ζ_i is the modal damping ratio, ω_i is the natural angular frequency of the mode and Q_i is the generalised force.

Now since the contribution of the i th mode to the displacement of the hub, u (in the x -direction) i.e. u_i is given by:

$$u_i = \phi_{ihx} q_i \quad (\text{from equation (1)})$$

$$\Rightarrow q_i = \frac{u_i}{\phi_{ihx}} \Rightarrow \dot{q}_i = \frac{\dot{u}_i}{\phi_{ihx}} \Rightarrow \ddot{q}_i = \frac{\ddot{u}_i}{\phi_{ihx}}$$

Substituting these three expressions into equation (3) yields:

$$m_{ii} \left[\frac{\ddot{u}_i}{\phi_{ihx}} + 2\zeta_i \omega_i \frac{\dot{u}_i}{\phi_{ihx}} + \omega_i^2 \frac{u_i}{\phi_{ihx}} \right] = Q_i$$

$$\Rightarrow \frac{m_{ii}}{\phi_{ihx}} [\ddot{u}_i + 2\zeta_i \omega_i \dot{u}_i + \omega_i^2 u_i] = Q_i \quad (4)$$

Similarly the contribution of the i th mode to the displacement of the hub, v (in the y -direction) i.e. v_i is given by:

$$v_i = \phi_{ihy} q_i$$

and equation (3) becomes:

$$\frac{m_{ii}}{\phi_{ihy}} [\ddot{v}_i + 2\zeta_i \omega_i \dot{v}_i + \omega_i^2 v_i] = Q_i \quad (5)$$

Note: Equations (4) and (5) are essentially equivalent forms of the same equation (3), i.e. all three equations describe the same modal dynamics.

In the study of ground resonance, the fuselage modes, which couple with the in-plane rotor motion at the hub, are of interest. Therefore only these modes are included in the analysis. Typically (or classically) at least the first fuselage roll (on its undercarriage) and pitch mode (also on its undercarriage) would be included in the analysis. Although, in proceeding, only these two modes will be included, it is easy to generalise the theory and include all the fuselage modes considered to be necessary to capture the relevant dynamic effects.

Now assume that the first roll is the j th and the first pitch is the i th natural mode. The pitch mode can therefore be expressed from equation (4) as:

$$\frac{m_{ii}}{\phi_{ihx}} [\ddot{u}_i + 2\zeta_i \omega_i \dot{u}_i + \omega_i^2 u_i] = Q_i$$

or by letting $\frac{m_{ii}}{\phi_{ihx}} = M_{fx}$ (the effective fuselage modal mass in pitch at the hub) yields:

$$M_{fx} [\ddot{u}_i + 2\zeta_i \omega_i \dot{u}_i + \omega_i^2 u_i] = Q_i \quad (6)$$

and the roll-mode can be expressed from equation (5) as:

$$\frac{m_{jj}}{\phi_{jhy}} [\ddot{v}_j + 2\zeta_j \omega_j \dot{v}_j + \omega_j^2 v_j] = Q_j$$

which, when letting $\frac{m_{jj}}{\phi_{jhy}} = M_{fy}$ (the effective fuselage modal mass in roll at the hub), yields:

$$M_{fy} [\ddot{v}_j + 2\zeta_j \omega_j \dot{v}_j + \omega_j^2 v_j] = Q_j \quad (7)$$

where ω_i and ω_j are the two uncoupled (i.e. no fuselage-rotor-coupling) natural frequencies of the pitch and roll modes, respectively.

For the uncoupled rotor, consider the general elastic lead-lag motion of a single helicopter rotor blade, in particular an element of length dx as indicated in figure 3.2.3:

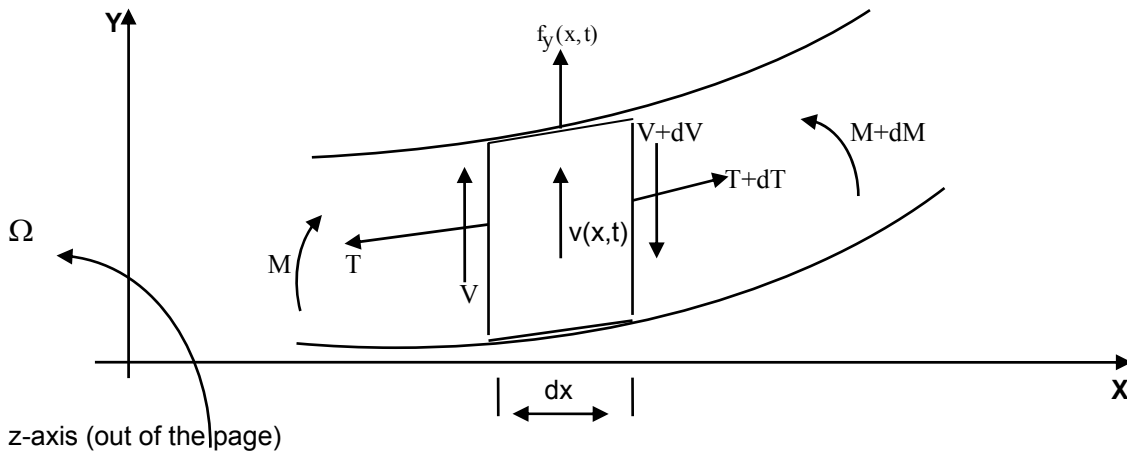


Figure 3.2.3 Forces and moments acting on a rotating rotor blade element

Let the blade and its associated axis system x - y - z be rotating with the constant rotor angular velocity Ω rad/s and let there be an external loading, $f_y(x, t)$, on the blade. The oscillatory displacement of the element in the y -direction, $v(x, t)$, is the lead-lag motion which is caused by $f_y(x, t)$. T and $T+dT$ are the axial forces tangential to the displaced blade reference line; V and $V+dV$ are the shear forces; M and $M+dM$ are the bending moments acting on the blade element and m is the mass per unit length of the blade.

If only the motion in the x - y -plane is considered, the degrees of freedom of the blade element are reduced from 6 (three of translation and three of rotation) to 3 (translation in the x - and y -directions and rotation about the z -axis).

First consider the moment equilibrium about the z -axis:

Summing the moments about a point on the reference line on the right face of the element, the moment equilibrium can be given as:

$$M + dM - M - Vdx - f_y dx \frac{dx}{2} = 0$$

$$\therefore dM - Vdx - \frac{1}{2} f_y (dx)^2 = 0$$

Since a differential element is being considered, $(dx)^2$ will be very small, so that it can be assumed that $(dx)^2 \cong 0$.

Thus,

$$dM - Vdx = 0$$

$$\therefore \frac{dM}{dx} - V = 0,$$

so that the moment equilibrium of the element, about the z -axis yields:

$$\frac{dM}{dx} = V. \quad (8)$$

Using Euler-Bernoulli beam theory, the bending moment is related to the curvature by the flexure equation, which, for the co-ordinates indicated in figure 3.2.3, is:

$$M = EI_z \frac{d^2v}{dx^2}, \quad (9)$$

where E is Young's modulus, I_z is the moment of inertia about the z-axis and EI_z is the flexural stiffness about the z-axis. Therefore:

$$V = \frac{d}{dx} (EI_z \frac{d^2v}{dx^2}) \quad (\text{from equation (8)}) \quad (10)$$

This means that the rotation of the element about the z-axis is linked to the transverse displacement 'v', as $\frac{dv}{dx}$, and effectively the degrees of freedom of the element are reduced from 3 to 2.

Now assume that the blade is rigid in extension. As a result there is no displacement-unknown associated with translation in the x-direction and the degrees of freedom of the blade element are reduced to one. Although this is so, it is still necessary to consider the x-direction equation of motion given by:

$$(T + dT) \cos\left(\frac{\partial v}{\partial x} + \delta \frac{\partial v}{\partial x}\right) - T \cos \frac{\partial v}{\partial x} + f_x(x) dx = 0$$

Since only very small displacements are being considered, $\cos(\text{small angles}) \cong 1$ and therefore:

$$T + dT - T + f_x(x) dx = 0$$

(where $f_x(x)$ is a force which arises due to the rotation of the blade)

$$\therefore dT = -mx\Omega^2 dx.$$

Now integrating from the tip of the blade $x = L$ to a point x^* on the blade yields:

$$\begin{aligned} \int_L^{x^*} dT &= - \int_L^{x^*} mx\Omega^2 dx \\ \therefore T(x^*) - T(L) &= - \int_L^{x^*} mx\Omega^2 dx \\ \therefore T(x^*) &= - \int_L^{x^*} mx\Omega^2 dx \\ \therefore T(x^*) &= \int_{x^*}^L mx\Omega^2 dx \\ \therefore T(x) &= \int_x^L mx^*\Omega^2 dx^*. \end{aligned} \quad (11)$$

Since only one degree of freedom (i.e. translation in the y-direction) remains, consider the equation of motion in the y-direction, for a fixed hub (i.e. no translation at the hub), which is given by:

$$f_y \delta x + V - (V + \delta V) + (T + \delta T) \left(\frac{\partial v}{\partial x} + \delta \frac{\partial v}{\partial x} \right) - T \frac{\partial v}{\partial x} = m \left[\frac{\partial^2 v}{\partial t^2} \delta x - \Omega^2 v \delta x \right] \quad (12)$$

Due to the rotation of the blade a centripetal acceleration, CA, arises which acts on the blade element as indicated in figure 3.2.4:

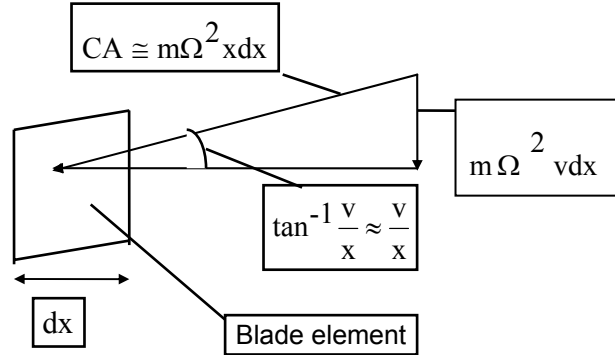


Figure 3.2.4 Centripetal acceleration acting on a blade element

This acceleration, CA, has a component, $\Omega^2 v dx$ in the negative y-direction, which gives rise to the negative term on the right hand side of equation (12).

To study ground resonance the uncoupled rotor and the uncoupled fuselage must be combined and the dynamic equations of this new, resulting system must be considered. In this new system the hub is not fixed and therefore hub acceleration must be considered. If the hub is accelerating in the y-direction, with an amount of \ddot{v}_{hr} , the elemental differential equation of motion will be:

$$f_y \delta x + V - (V + \delta V) + (T + \delta T) \left(\frac{\partial v}{\partial x} + \delta \frac{\partial v}{\partial x} \right) - T \frac{\partial v}{\partial x} = m \left(\frac{\partial^2 v}{\partial t^2} + \frac{d^2 v_{hr}}{dt^2} \right) \delta x - m \Omega^2 v \delta x \quad (13)$$

where v is measured relative to the hub.

$$\begin{aligned} \therefore f_y \delta x - \delta V + T \delta \frac{\partial v}{\partial x} + \delta T \frac{\partial v}{\partial x} + \delta T \delta \frac{\partial v}{\partial x} + m \Omega^2 v \delta x \\ = m \frac{\partial^2 v}{\partial t^2} \delta x + m \frac{d^2 v_{hr}}{dt^2} \delta x \end{aligned}$$

Now writing $T \delta \frac{\partial v}{\partial x} + \delta T \frac{\partial v}{\partial x} = \delta \left(T \frac{\partial v}{\partial x} \right)$ and ignoring the term $\delta T \delta \frac{\partial v}{\partial x}$ as it is very small, results in:

$$f_y \delta x - \delta V + \delta \left(T \frac{\partial v}{\partial x} \right) + m \Omega^2 v \delta x = m \frac{\partial^2 v}{\partial t^2} \delta x + m \frac{d^2 v_{hr}}{dt^2} \delta x$$

It therefore follows that:

$$f_y - \frac{\partial V}{\partial x} + \frac{\partial}{\partial x} \left(T \frac{\partial v}{\partial x} \right) + m\Omega^2 v = m \frac{\partial^2 v}{\partial t^2} + m \frac{d^2 v_{hr}}{dt^2} \quad (14)$$

Now substituting equations (10) and (11) into equation (14) and simplifying yields:

$$f_y - \frac{\partial^2}{\partial x^2} (EI_z \frac{\partial^2 v}{\partial x^2}) + \Omega^2 \left[\frac{\partial}{\partial x} \left(\frac{\partial v}{\partial x} \int_0^L mx^* dx^* \right) + mv \right] = m \frac{\partial^2 v}{\partial t^2} + m \frac{d^2 v_{hr}}{dt^2}$$

$$\therefore m \frac{\partial^2 v}{\partial t^2} + \frac{\partial^2}{\partial x^2} (EI_z \frac{\partial^2 v}{\partial x^2}) - \Omega^2 \left[\frac{\partial}{\partial x} \left(\frac{\partial v}{\partial x} \int_0^L mx^* dx^* \right) + mv \right] = f_y - m \frac{d^2 v_{hr}}{dt^2} \quad (15)$$

Now consider the three terms on the left hand side of equation (15). The first term is associated with an acceleration in the lead-lag direction, the second term may be considered to be a structural stiffness term, as it describes the effect of the blade bending stiffness at zero rotational speed and the third term is associated with the “centrifugal stiffening” effect and is therefore also considered to be a stiffness term.

Equation (15) is a partial differential equation with independent variables ‘x’ and ‘t’. In order to separate these variables, let the partial differential equation (15) be satisfied by functions of the form:

$$v(x, t) = \phi(x)q(t) \quad (16)$$

where $\phi(x)$ is a function of the space variable x alone and q(t) is a function of t alone. Considering the homogenous equation of equation (15), initially assuming the hub to be fixed i.e. $v_{hr} = 0$ and substituting the expression for v given in equation (16) yields:

$$m\phi \frac{\partial^2 q}{\partial t^2} + \frac{\partial^2}{\partial x^2} (EI_z \frac{\partial^2 \phi}{\partial x^2}) q - \Omega^2 \left[\frac{\partial}{\partial x} \left(\frac{\partial \phi}{\partial x} \int_0^L mx^* dx^* \right) q + m\phi q \right] = 0 \quad (17)$$

$$\therefore \frac{1}{q} \frac{\partial^2 q}{\partial t^2} = - \frac{1}{m\phi} \frac{\partial^2}{\partial x^2} (EI_z \frac{\partial^2 \phi}{\partial x^2}) + \Omega^2 \frac{1}{m\phi} \left[\frac{\partial}{\partial x} \left(\frac{\partial \phi}{\partial x} \int_0^L mx^* dx^* \right) + 1 \right] \quad (18)$$

Since the left-hand side of equation (18) is independent of x and the right hand side is independent of t, the partial derivatives can be replaced by ordinary derivatives. Furthermore, as equation (18) holds for all values of t and x, it follows that each side must be a constant. Let this

constant be $-\omega^2$. Setting the right hand side of equation (18) equal to $-\omega^2$ yields:

$$\frac{d^2}{dx^2} (EI_z \frac{d^2 \phi}{dx^2}) - \Omega^2 \left[\frac{d}{dx} \left(\frac{d\phi}{dx} \int_0^L mx^* dx^* \right) + m\phi \right] = \omega^2 m\phi$$

or

$$[EI_z \phi_i'''] - \Omega^2 \left\{ \left[\phi_i' \int_0^L mx^* dx^* \right]' + m\phi_i \right\} = \omega_i^2 m\phi_i \quad (19)$$

where ()' and ()'' are the first and second spatial derivatives of the quantity within the brackets. For the special case of span wise homogenous bending stiffness EI_z and zero rotational speed, Ω , a closed form solution, consisting of the mode shapes, ϕ_i , and their associated natural

angular frequencies, ω_i , can be found. It is therefore assumed that the solution to (19), where Ω is unequal to zero and the span wise EI_z distribution is not homogenous, can also be obtained e.g. experimentally or numerically.

To further investigate these modes, consider the boundary conditions that apply to equation (15):

At the blade tip, typically $V=0$ (20)

$$\therefore \frac{\partial}{\partial x} (EI_z \frac{\partial^2 v}{\partial x^2} (x, t) \Big|_{x=L}) = 0 \quad \text{(from equation (10))} \quad (21)$$

and $M=0$

$$\therefore EI_z \frac{\partial^2 v}{\partial x^2} (x, t) \Big|_{x=L} = 0 \quad \text{(from equation (9))} \quad (22)$$

At the root $v(0, t) = 0$ for the hub fixed case. (23)

If the blade is articulated, the root moment 'M' is zero or

$$EI_z \frac{\partial^2 v}{\partial x^2} (x, t) \Big|_{x=0} = 0 \quad (24)$$

If the blade is hingeless, the root is "clamped" and

$$\frac{\partial v}{\partial x} (0, t) = 0 \quad (25)$$

Two characteristics may be associated with the mode shapes of any vibrating system; these are self-adjointness and orthogonality. To investigate the possible self-adjointness of the modes, consider the statement of self-adjointness for this system:

$$\int_0^L \phi_j \{ [EI_z \phi_i^{''''}] - \Omega^2 \{ [\phi_i \int_x^L mx^* dx^*]' + m\phi_i \} \} dx =$$

$$\int_0^L \phi_i \{ [EI_z \phi_j^{''''}] - \Omega^2 \{ [\phi_j \int_x^L mx^* dx^*]' + m\phi_j \} \} dx$$

where ϕ_i and ϕ_j are two mode shapes that satisfy equation (18).

Now let

$$I_1 = \int_0^L \phi_j \{ [EI_z \phi_i^{''''}] - \Omega^2 \{ [\phi_i \int_x^L mx^* dx^*]' + m\phi_i \} \} dx =$$

$$\int_0^L \phi_j \{ [EI_z \phi_i^{''''}] - \Omega^2 [\phi_i \int_x^L mx^* dx^*]' \} dx - \Omega^2 \int_0^L m\phi_j \phi_i dx$$

Performing integration by parts on the first integral yields:

$$I_1 = [\phi_j \{ [EI_z \phi_i'''] - \Omega^2 \phi_i' \int_x^L mx^* dx^* \}]_0^L - \int_0^L \phi_j' \{ [EI_z \phi_i'''] - \Omega^2 \phi_i' \int_x^L mx^* dx^* \} dx - \Omega^2 \int_0^L m \phi_j \phi_i' dx \quad (26)$$

Now from equation (16) and (23):

$$v(0, t) = \phi(0)q(t) = 0 \Rightarrow \phi(0) = 0 \Rightarrow \phi_j'(0) = 0$$

$$\text{and from equation (21): } [EI_z \phi_i''']_{x=L} = 0$$

and $\int_0^L mx^* dx^* = 0$ so that the first term on the right hand side of equation (26) is equal to zero.

$$\begin{aligned} \therefore I_1 &= - \int_0^L \phi_j' \{ [EI_z \phi_i'''] - \Omega^2 \phi_i' \int_x^L mx^* dx^* \} dx - \Omega^2 \int_0^L m \phi_j \phi_i' dx = \\ &= - \int_0^L \phi_j' [EI_z \phi_i'''] dx + \Omega^2 \int_0^L \phi_j' \phi_i' \int_x^L mx^* dx^* dx - \Omega^2 \int_0^L m \phi_j \phi_i' dx \end{aligned}$$

Again performing integration by parts on the first integral yields:

$$I_1 = -[\phi_j' [EI_z \phi_i''']]_0^L + \int_0^L \phi_j'' EI_z \phi_i'' dx + \Omega^2 \int_0^L \phi_j' \phi_i' \int_x^L mx^* dx^* dx - \Omega^2 \int_0^L m \phi_j \phi_i' dx \quad (27)$$

Now from equation (25): $\phi_j'(x) \Big|_{x=0} = 0$ for a hingeless blade or from equation (24):

$\phi_i''(x) \Big|_{x=0} = 0$ for an articulated blade and from equation (22): $EI_z \phi_i''(x) \Big|_{x=L} = 0$ so

that the first term on the right hand side of equation (27) is zero. Then:

$$I_1 = \int_0^L EI_z \phi_j'' \phi_i'' dx + \Omega^2 \int_0^L \phi_j' \phi_i' \int_x^L mx^* dx^* dx - \Omega^2 \int_0^L m \phi_j \phi_i' dx$$

Similarly it can be shown that

$$I_2 = \int_0^L \phi_i \{ [EI_z \phi_j'''] - \Omega^2 \{ [\phi_j' \int_x^L mx^* dx^*] + m \phi_j \} \} dx = \int_0^L EI_z \phi_i'' \phi_j'' dx + \Omega^2 \int_0^L \phi_i' \phi_j' \int_x^L mx^* dx^* dx - \Omega^2 \int_0^L m \phi_i \phi_j' dx \quad (28)$$

$\therefore I_1 = I_2$ and self-adjointness is proven for the given system. The characteristic of orthogonality of the modes may be investigated as follows:

Multiplying equation (19) by ϕ_j and integrating yields:

$$\int_0^L \phi_j \{ [EI_Z \phi_i'''] - \Omega^2 \{ [\phi_i' \int_x^L mx * dx *]' + m \phi_i \} \} dx = \int_0^L \phi_j \omega_i^2 m \phi_i dx$$

$$= \omega_i^2 \int_0^L m \phi_i \phi_j dx$$
(29)

and

$$\int_0^L \phi_i \{ [EI_Z \phi_j'''] - \Omega^2 \{ [\phi_j' \int_x^L mx * dx *]' + m \phi_j \} \} dx = \omega_j^2 \int_0^L m \phi_i \phi_j dx$$
(30)

Subtracting (30) from (29) and taking into account that the two left-hand sides are equal due to the problem being self-adjoint yields:

$$(\omega_i^2 - \omega_j^2) \int_0^L m \phi_i \phi_j dx = 0$$
(31)

$$\therefore \int_0^L m \phi_i \phi_j dx = 0 \quad \text{for } i \neq j, \text{ in the case of no repeated roots.}$$
(32)

Now from equations (28), (30) and (32):

$$\int_0^L \phi_i \{ [EI_Z \phi_j'''] - \Omega^2 \{ [\phi_j' \int_x^L mx * dx *]' + m \phi_j \} \} dx =$$

$$\int_0^L EI_Z \phi_i'' \phi_j'' dx + \Omega^2 \int_0^L \phi_i' \phi_j' \int_x^L mx * dx * dx - \Omega^2 \int_0^L m \phi_i \phi_j dx =$$
(33)

$$\omega_j^2 \int_0^L m \phi_i \phi_j dx = 0 \quad \text{for } i \neq j$$

Equations (32) and (33) define two orthogonality relationships for the mode shapes ϕ_i and ϕ_j .

It can therefore be concluded that the problem defined by equation (18) is self-adjoint, and that the corresponding mode shapes are orthogonal in the sense of equations (32) and (33). Expressing $v(x, t)$ as the sum of a limited number of these modes, multiplying by generalised coordinates q_i yields:

$$v(x, t) = \sum_i \phi_i(x) q_i(t)$$

and substituting this into equation (15) yields:

$$\sum_i \left\{ m \phi_i \ddot{q}_i + \left[\frac{d^2}{dx^2} (EI_z \frac{d^2 \phi_i}{dx^2}) - \Omega^2 \left[\frac{d}{dx} \left(\frac{d \phi_i}{dx} \int_0^L m x^* dx^* \right) + m \phi_i \right] \right] q_i \right\} = f_y - m \frac{d^2 v_{hr}}{dt^2}$$

Multiplying by ϕ_j , integrating over the length of the blade, using equation (19) and invoking the orthogonality condition of equation (32) yields:

$$\int_0^L m \phi_i^2 dx q_i \ddot{q}_i + \omega_i^2 \int_0^L m \phi_i^2 dx q_i = \int_0^L \phi_i f_y(x, t) dx - \int_0^L m \phi_i dx \frac{d^2 v_{hr}}{dt^2} \quad (34)$$

At this point it must be noted that the orthogonality condition was derived for a fixed hub system with $v_{hr} = 0$ as assumed above equation (17). Therefore the modes of this system are not analytically accurate for the case where $v_{hr} \neq 0$. Although this is the case, it has been found that, in practice, these mode shapes are a reasonable approximation, good enough that in a Galerkin approach (used later), the modal mass and stiffness matrices are approximately diagonal.

Now introducing the first edgewise mode shape ϕ_e for ϕ_i , replacing L with the length of the

blade R, defining the modal mass $M_e = \int_0^R m \phi_e^2 dr$ (where m is the blade mass per unit span),

introducing a modal damping term, letting $\int_0^R \phi_e f_y(x, t) dr = Q_e$ (the generalised external

loading of the mode ϕ_e) and replacing the generalised co-ordinate q with ξ , equation (34) becomes:

$$M_e \ddot{\xi} + 2M_e \zeta_e \omega_e \dot{\xi} + M_e \omega_e^2 \xi = Q_e - \int_0^R m \phi_e dr \ddot{v}_{hr} = Q_e - s \ddot{v}_{hr} \quad (35)$$

where $s = \int_0^R m \phi_e dr$ (assuming that the mode shape ϕ_e of the uncoupled system is still a good approximation of the new, coupled, mode shape). ζ_e is the damping ratio associated with the mode ϕ_e and ω_e is the natural frequency of this mode in the rotating reference frame. \ddot{v}_{hr} in equation (35) can be related to the fixed system accelerations indicated in Figure 3.2.1 by the following figure:

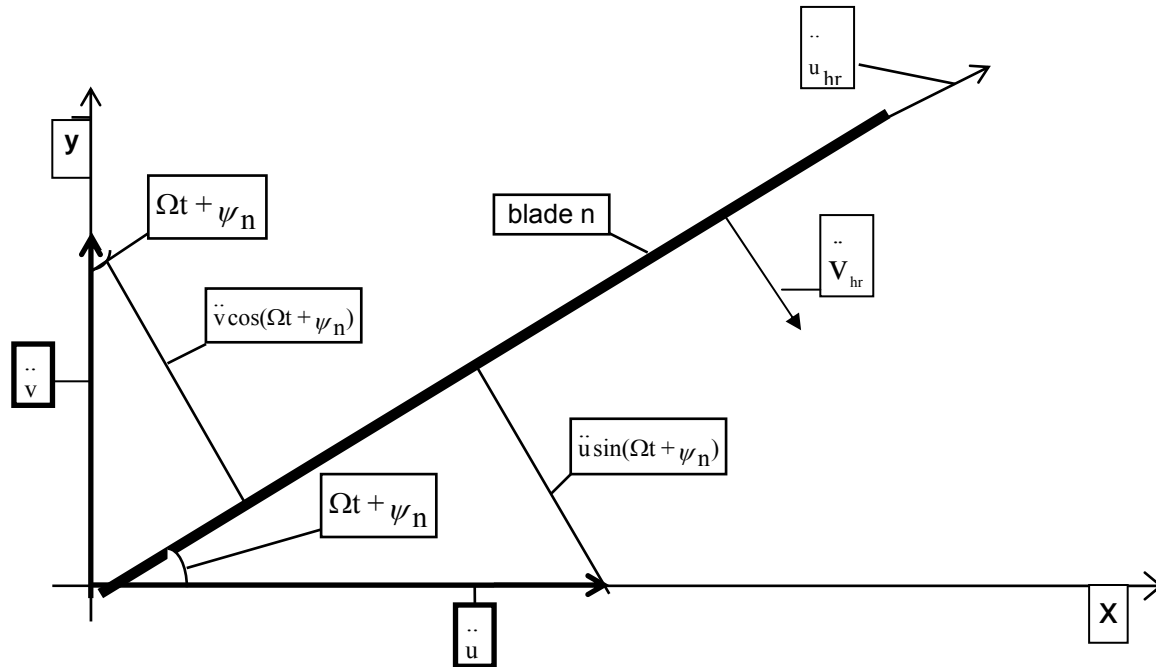


Figure 3.2.5 Acceleration components of a blade in a non-rotating reference frame

- Note:
- The symbols 'x', 'y' and 'v' now refer to the x-and y-axis and the displacement in the y-direction respectively in a non-rotating frame.
 - The direction of the acceleration \ddot{v}_{hr} is chosen to coincide with the lag degree of freedom ξ , which is defined to be positive for motion opposing the rotor rotation direction (which was anti-clockwise in figure 3.2.3).

From figure 3.2.5 it can be seen that:

$$\ddot{u}_{hr} = \ddot{u} \cos(\Omega t + \psi_n) + \ddot{v} \sin(\Omega t + \psi_n) \quad (36)$$

$$\ddot{v}_{hr} = \ddot{u} \sin(\Omega t + \psi_n) - \ddot{v} \cos(\Omega t + \psi_n)$$

and therefore equation (35) can be written as:

$$M_e \ddot{\xi} + 2M_e \zeta_e \omega_e \dot{\xi} + M_e \omega_e^2 \xi = Q_e - s \ddot{u} \sin(\Omega t + \psi_n) + s \ddot{v} \cos(\Omega t + \psi_n) \quad (37)$$

Now assume that the rotor has three or more identical blades. The rotor equation (37) is derived for a single blade but in reality the rotor responds as a whole to excitation from the non-rotating frame. It is therefore desirable to work with degrees of freedom that reflect this behaviour. For the steady state solution, the appropriate representation of the blade motion is a Fourier series, the harmonics of which describe the motion of the rotor as a whole. However, since the steady state solution is not of interest, but rather the general dynamic behaviour of the rotor, including the transient response, the appropriate transformation of the degrees of freedom and the equations of motion to the non-rotating frame is not a Fourier series but it is still of the Fourier type known as multi-blade co-ordinates [35 p 32]. For the Fourier co-ordinate transformation, consider the following:

Consider a rotor with b blades, equally spaced around the azimuth at $\Omega t + \psi_n$, where Ωt is the dimensionless time variable for constant rotational speed and $\psi_n = \frac{2\pi n}{b}$ where $\frac{2\pi}{b}$ is the azimuthal spacing between the blades. The blade index n ranges from 1 to b . Now let ξ^j be the degree of freedom in the rotating frame of the j th blade. The Fourier co-ordinate transformation is a linear transformation of the degrees of freedom from the rotating to the non-rotating frame. The following new degrees of freedom are introduced [32 p. 350, 351]:

$$\begin{aligned}\xi_0 &= \frac{1}{b} \sum_{j=1}^b \xi^j \\ \xi_c &= \frac{2}{b} \sum_{j=1}^b \xi^j \cos(\Omega t + \psi_j) \\ \xi_s &= \frac{2}{b} \sum_{j=1}^b \xi^j \sin(\Omega t + \psi_j)\end{aligned}\quad (38)$$

These degrees of freedom describe the motion of the rotor in the non-rotating frame. The corresponding inverse transformation is given by:

$$\xi^n = \xi_0 + \xi_c \cos(\Omega t + \psi_n) + \xi_s \sin(\Omega t + \psi_n) + \dots \quad (39)$$

The physical interpretation of the ξ_c and ξ_s terms in equation (39) are indicated in figure 3.2.6:

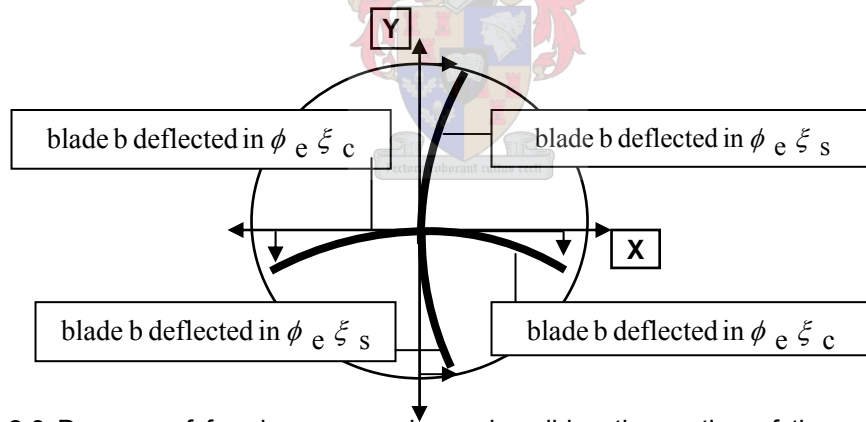


Figure 3.2.6 Degrees of freedom ξ_c and ξ_s describing the motion of the rotor in the non-rotating frame

Now taking the time derivatives of equation (39) yields:

$$\dot{\xi}^n = \dot{\xi}_0 + (\dot{\xi}_c + \Omega \xi_s) \cos(\Omega t + \psi_n) + (\dot{\xi}_s - \Omega \xi_c) \sin(\Omega t + \psi_n) + \dots \quad (40)$$

and

$$\begin{aligned}\ddot{\xi}^n &= \ddot{\xi}_0 + (\ddot{\xi}_c + 2\Omega \dot{\xi}_s - \Omega^2 \xi_c) \cos(\Omega t + \psi_n) \\ &+ (\ddot{\xi}_s - 2\Omega \dot{\xi}_c - \Omega^2 \xi_s) \sin(\Omega t + \psi_n) + \dots\end{aligned}\quad (41)$$

Now let $\dot{\xi}_{\dot{c}} = \dot{\xi}_c + \Omega \xi_s$ and $\dot{\xi}_{\dot{s}} = \dot{\xi}_s - \Omega \xi_c$ (42)

then equation (40) can be written as:

$$\dot{\xi}^n = \dot{\xi}_0 + \dot{\xi}_c \cos(\Omega t + \psi_n) + \dot{\xi}_s \sin(\Omega t + \psi_n) + \dots \quad (43)$$

and let $\ddot{\xi}_{\dot{c}} = \ddot{\xi}_c + 2\Omega \dot{\xi}_s - \Omega^2 \xi_c$ and $\ddot{\xi}_{\dot{s}} = \ddot{\xi}_s - 2\Omega \dot{\xi}_c - \Omega^2 \xi_s$ (44)

then equation (41) can be written as:

$$\ddot{\xi}^n = \ddot{\xi}_0 + \ddot{\xi}_c \cos(\Omega t + \psi_n) + \ddot{\xi}_s \sin(\Omega t + \psi_n) + \dots \quad (45)$$

Since equation (43) is of the same form as equation (39), $\dot{\xi}_c$ and $\dot{\xi}_s$ can be rewritten by using equations (38) and (42) as:

$$\dot{\xi}_c = \frac{2}{b} \sum_{j=1}^b \dot{\xi}^j \cos(\Omega t + \psi_j) = \dot{\xi}_c + \Omega \xi_s \quad (46)$$

and

$$\dot{\xi}_s = \frac{2}{b} \sum_{j=1}^b \dot{\xi}^j \sin(\Omega t + \psi_j) = \dot{\xi}_s - \Omega \xi_c \quad (47)$$

Similarly, since equation (45) is of the same form as equation (39) and by using equations (38) and (44) yields:

$$\ddot{\xi}_{\dot{c}} = \frac{2}{b} \sum_{j=1}^b \ddot{\xi}^j \cos(\Omega t + \psi_j) = \ddot{\xi}_c + 2\Omega \dot{\xi}_s - \Omega^2 \xi_c \quad (48)$$

and

$$\ddot{\xi}_{\dot{s}} = \frac{2}{b} \sum_{j=1}^b \ddot{\xi}^j \sin(\Omega t + \psi_j) = \ddot{\xi}_s - 2\Omega \dot{\xi}_c - \Omega^2 \xi_s \quad (49)$$

Equations (48) and (49) are equivalent to those given in [32, p 355].

Equation (37) is the differential equation of motion of the first lead-lag mode of a single blade. To obtain a set of equations for all the blades in terms of the multi-blade coordinates:

a) Multiply equation (37) by $\sin(\Omega t + \psi_n)$ and sum over all the blades i.e.:

$$M_e \sum_{j=1}^b \ddot{\xi}^j \sin(\Omega t + \psi_j) + 2M_e \zeta_e \omega_e \sum_{j=1}^b \dot{\xi}^j \sin(\Omega t + \psi_j) + M_e \omega_e^2 \sum_{j=1}^b \xi^j \sin(\Omega t + \psi_j) = \sum_{j=1}^b Q_e^j \sin(\Omega t + \psi_j) - s \ddot{u} \sum_{j=1}^b \sin^2(\Omega t + \psi_j) + s \ddot{v} \sum_{j=1}^b \sin(\Omega t + \psi_j) \cos(\Omega t + \psi_j) \quad (50)$$

Using equations (38), (47) and (49), and the identities:

$$\sum_{j=1}^b \sin^2(\Omega t + \psi_j) = \sum_{j=1}^b \cos^2(\Omega t + \psi_j) = \frac{b}{2}$$

and

(51)

$$\sum_{j=1}^b \sin(\Omega t + \psi_j) \cos(\Omega t + \psi_j) = 0$$

equation (50) can be re-written as:

$$\begin{aligned} & \frac{b}{2} [M_e (\ddot{\xi}_s - 2\Omega \dot{\xi}_c - \Omega^2 \xi_s) + 2M_e \zeta_e \omega_e (\dot{\xi}_s - \Omega \xi_c) + M_e \omega_e^2 \xi_s] = \\ & \sum_{j=1}^b Q_e^j \sin(\Omega t + \psi_j) - \frac{b}{2} s \ddot{u} \end{aligned} \quad (52)$$

b) Multiply equation (37) by $\cos(\Omega t + \psi_j)$ and sum over all the blades. This yields:

$$\begin{aligned} & M_e \sum_{j=1}^b \ddot{\xi}^j \cos(\Omega t + \psi_j) + 2M_e \zeta_e \omega_e \sum_{j=1}^b \dot{\xi}^j \cos(\Omega t + \psi_j) + M_e \omega_e^2 \sum_{j=1}^b \xi^j \cos(\Omega t + \psi_j) = \\ & \sum_{j=1}^b Q_e^j \cos(\Omega t + \psi_j) - s \ddot{u} \sum_{j=1}^b \sin(\Omega t + \psi_j) \cos(\Omega t + \psi_j) + s \ddot{v} \sum_{j=1}^b \cos^2(\Omega t + \psi_j) \end{aligned} \quad (53)$$

Substituting equations (38), (46) and (48) into equation (53) and using the same identities given in equation (51) yields:

$$\begin{aligned} & \frac{b}{2} [M_e (\ddot{\xi}_c + 2\Omega \dot{\xi}_s - \Omega^2 \xi_c) + 2M_e \zeta_e \omega_e (\dot{\xi}_c + \Omega \xi_s) + M_e \omega_e^2 \xi_c] = \\ & \sum_{j=1}^b Q_e^j \cos(\Omega t + \psi_j) + \frac{b}{2} s \ddot{v} \end{aligned} \quad (54)$$

Dividing equations (52) and (54) by $\frac{b}{2}$, they can be summarised in matrix form as:

$$\begin{aligned} & M_e \begin{bmatrix} 1 & 0 \\ 0 & 1 \end{bmatrix} \begin{bmatrix} \ddot{\xi}_c \\ \ddot{\xi}_s \end{bmatrix} + \begin{bmatrix} 2\zeta_e \omega_e & 2\Omega \\ -2\Omega & 2\zeta_e \omega_e \end{bmatrix} \begin{bmatrix} \dot{\xi}_c \\ \dot{\xi}_s \end{bmatrix} + \begin{bmatrix} \omega_e^2 - \Omega^2 & 2\Omega \zeta_e \omega_e \\ -2\Omega \zeta_e \omega_e & \omega_e^2 - \Omega^2 \end{bmatrix} \begin{bmatrix} \xi_c \\ \xi_s \end{bmatrix} \\ & + s \begin{bmatrix} -1 & 0 \\ 0 & 1 \end{bmatrix} \begin{bmatrix} \ddot{v} \\ \ddot{u} \end{bmatrix} = \begin{bmatrix} Q_{ec} \\ Q_{es} \end{bmatrix} \end{aligned} \quad (55)$$

where

$$Q_{e_c} = \frac{2}{b} \sum_{j=1}^b Q_e^j \cos(\Omega t + \psi_j)$$

and

$$Q_{e_s} = \frac{2}{b} \sum_{j=1}^b Q_e^j \sin(\Omega t + \psi_j)$$

It must be noted that neither ω_e nor $\omega_e - \Omega$ (even though natural frequencies of the decoupled blade system in the rotating and non-rotating frames) is a natural frequency of the coupled system.

Thus far the equations of motion for the rotor lag degrees of freedom, including the influence of the hub motion, have been considered, without considering specific hub loads that arise due to the blade rotation. To analyse these loads consider the in-plane shear forces acting at the rotor hub. To do this, consider an axis system similar to the one in figure 3.2.3 as indicated by figure 3.2.7:

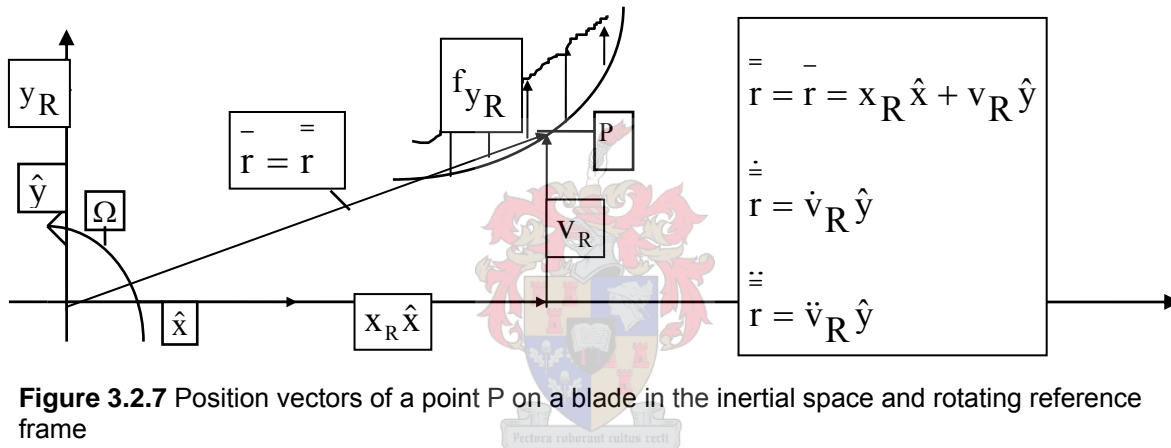


Figure 3.2.7 Position vectors of a point P on a blade in the inertial space and rotating reference frame

In Figure 3.2.7, $\hat{z} = \hat{x} \times \hat{y}$, \bar{r} is the vector in the inertial space and \tilde{r} is the vector in the rotating reference frame.

Note: a) v_R is the same as $v(x,t)$ given in figure 3.2.3 and is denoted as such in order to distinguish this displacement from others previously used.

b) In the sketch \bar{r} and \tilde{r} coincide such that $\tilde{r} = \bar{r} = x_R \hat{x} + v_R \hat{y}$.

c) $\dot{\tilde{r}}$ and $\ddot{\tilde{r}}$ denote the first and second time derivative of the position vector \tilde{r} in the rotating frame.

The axis system in figure 3.2.7 is rotating with the blade. A general displacement v_R in this axis system may be expressed as a vector $v_R \hat{y}$. Now since the position vector of point P is given by

$\bar{r} = x_R \hat{x} + v_R \hat{y}$, the velocity of P is $\dot{\bar{r}} = \bar{\omega} \times \bar{r} + \dot{x}_R \hat{x} + \dot{v}_R \hat{y} = \bar{\omega} \times \bar{r} + v_{\dot{R}} \hat{y} = \bar{\omega} \times \bar{r} + \dot{\tilde{r}}$, where $\bar{\omega} = \Omega \hat{z}$ in the sketch. The velocity due to v_R , in the inertial system can be given by:

$$\Omega \hat{z} \times (v_R \hat{y} + x_R \hat{x}) + \dot{v}_R \hat{y} = (\Omega x_R + \dot{v}_R) \hat{y} - \Omega v_R \hat{x}$$

Similarly, since the second time derivative of \bar{r} can be given by $\ddot{\bar{r}} = \ddot{r} + 2\dot{\bar{\omega}} \times \bar{r} + \dot{\bar{\omega}} \times \dot{\bar{r}} + \bar{\omega} \times (\bar{\omega} \times \bar{r})$, the acceleration due to v_R in the inertial system can be given by:

$$\ddot{v}_R \hat{y} + 2\Omega \hat{z} \times \dot{v}_R \hat{y} + \dot{\Omega} \hat{z} \times (x_R \hat{x} + v_R \hat{y}) + \Omega \hat{z} \times (\Omega \hat{z} \times (x_R \hat{x} + v_R \hat{y})) =$$

(as Ω is constant $\Rightarrow \dot{\Omega} = 0$)

$$\ddot{v}_R \hat{y} - 2\Omega \dot{v}_R \hat{x} + \Omega \hat{z} \times (\Omega x_R \hat{y} - \Omega v_R \hat{x}) =$$

$$\ddot{v}_R \hat{y} - 2\Omega \dot{v}_R \hat{x} - \Omega^2 x_R \hat{x} - \Omega^2 v_R \hat{y} =$$

$$-(\Omega^2 x_R + 2\Omega \dot{v}_R) \hat{x} + (\ddot{v}_R - \Omega^2 v_R) \hat{y}$$

The axial load due to $-\Omega^2 x_R \hat{x}$ cancels those of all the other blades and may therefore be neglected in the hub load calculation. The hub load in the positive x_R -direction can therefore be given by:

$$H_{x_R} = \int_0^R 2\Omega \dot{v}_R m dx_R - \int_0^R m \ddot{u}_{hR} dx_R$$

where \ddot{u}_{hR} is the component of the rotor hub acceleration \ddot{u} in the x_R -direction. Therefore in terms of the generalized mass and generalized coordinate ξ :

$$H_{x_R} = -2\Omega \int_0^R m \phi_e dr \dot{\xi} - \int_0^R m dr \ddot{u}_{hR} \quad (56)$$

$$\therefore H_{x_R} = -2\Omega s \dot{\xi} - m_b \ddot{u}_{hR}$$

where $m_b = \int_0^R m dr$ is the blade mass.

Note: The first term on the right hand side of equation (56) is taken as negative since $\phi_e \dot{\xi}$ is taken to be positive in the opposite direction to v_R in figure 3.2.7.

The hub load in the positive y_R -direction is given by:

$$H_{y_R} = \int_0^R f y_R - m(\ddot{v}_R - \Omega^2 v_R - \ddot{v}_{hR}) dx_R$$

$$\therefore H_{y_R} = \int_0^R f y_R dr + \int_0^R m \phi_e dr (\ddot{\xi} - \Omega^2 \xi) + \int_0^R m dr \ddot{v}_{hR}$$

$$\therefore H_{y_R} = \int_0^R f_{y_R} dr + s(\ddot{\xi} - \Omega^2 \xi) + m_b \ddot{v}_{hR} \quad (57)$$

Note: Again the change in sign of the second term on the right hand side of the second equation above arises from v_R and $\phi_e \xi$ acting in opposite directions.

Now using the expressions for \ddot{u}_{hR} and \ddot{v}_{hR} given in equation (36) and substituting these into equations (56) and (57) yields:

$$H_{x_R} = -2\Omega s \dot{\xi} - m_b \ddot{u} \cos(\Omega t + \psi_n) - m_b \ddot{v} \sin(\Omega t + \psi_n) \quad (58)$$

and

$$H_{y_R} = \int_0^R f_{y_R} dr + s(\ddot{\xi} - \Omega^2 \xi) + m_b \ddot{u} \sin(\Omega t + \psi_n) - m_b \ddot{v} \cos(\Omega t + \psi_n) \quad (59)$$

Now consider the sketch in figure 3.2.8:

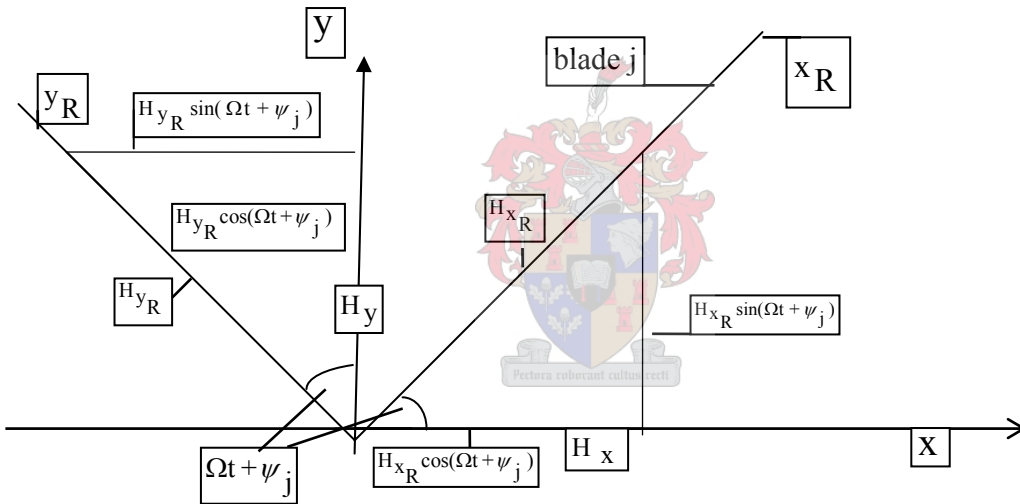


Figure 3.2.8 Hub load components

To obtain the effective load in the x-direction, the component of H_{x_R} and H_{y_R} in the x-direction must be considered and summed over all the blades. This, as can be seen from figure 3.2.8, yields:

$$H_x = \sum_{j=1}^b [H_{x_R}^j \cos(\Omega t + \psi_j) - H_{y_R}^j \sin(\Omega t + \psi_j)] \quad (60)$$

Now using the expressions for H_{x_R} and H_{y_R} given in equations (58) and (59) and substituting these into equation (60) yields:

$$\begin{aligned}
H_X &= \sum_{j=1}^b [(-2\Omega s \dot{\xi}^j - m_b \ddot{u} \cos(\Omega t + \psi_j) - m_b \ddot{v} \sin(\Omega t + \psi_j)) \cos(\Omega t + \psi_j) \\
&\quad - (\int_0^R f_{yR}^j dr + s(\ddot{\xi}^j - \Omega^2 \xi^j) + m_b \ddot{u} \sin(\Omega t + \psi_j) - m_b \ddot{v} \cos(\Omega t + \psi_j)) \sin(\Omega t + \psi_j)] \\
\therefore H_X &= \sum_{j=1}^b [-2\Omega s \dot{\xi}^j \cos(\Omega t + \psi_j) - \int_0^R f_{yR}^j dr \sin(\Omega t + \psi_j) - s(\ddot{\xi}^j - \Omega^2 \xi^j) \sin(\Omega t + \psi_j) \\
&\quad - m_b \ddot{u} (\sin^2(\Omega t + \psi_j) + \cos^2(\Omega t + \psi_j))]
\end{aligned}$$

now as $\sin^2(\Omega t + \psi_j) + \cos^2(\Omega t + \psi_j) = 1$

$$\begin{aligned}
\therefore H_X &= \sum_{j=1}^b [-2\Omega s \dot{\xi}^j \cos(\Omega t + \psi_j) - \int_0^R f_{yR}^j dr \sin(\Omega t + \psi_j) \\
&\quad - s \ddot{\xi}^j \sin(\Omega t + \psi_j) + s \Omega^2 \xi^j \sin(\Omega t + \psi_j) - m_b \ddot{u}]
\end{aligned} \tag{61}$$

Now by using the expression for $\sum_{j=1}^b \xi_j^j \cos(\Omega t + \psi_j)$ given by equation (46), writing

$$\sum_{j=1}^b \int_0^R f_{yR}^j dr \sin(\Omega t + \psi_j) \text{ as } F_{XS}, \text{ using the expression for } \sum_{j=1}^b \ddot{\xi}^j \sin(\Omega t + \psi_j) \text{ given}$$

by equation (49), using the expression for $\sum_{j=1}^b \xi^j \sin(\Omega t + \psi_j)$ given by equation (38), writing

$$\sum_{j=1}^b m_b \ddot{u} = b m_b \ddot{u} \text{ and substituting these into equation (61) yields:}$$

$$\begin{aligned}
H_X &= -2\Omega s \frac{b}{2} (\dot{\xi}_c + \Omega \xi_s) - F_{XS} - s \frac{b}{2} (\ddot{\xi}_s - 2\Omega \dot{\xi}_c - \Omega^2 \xi_s - \Omega^2 \xi_s) - b m_b \ddot{u} \\
\therefore H_X &= -s \frac{b}{2} \ddot{\xi}_s - b m_b \ddot{u} - F_{XS}
\end{aligned} \tag{62}$$

Similarly from figure 3.2.8, the effective load in the y-direction can be given by:

$$H_y = \sum_{j=1}^b [H_{xR}^j \sin(\Omega t + \psi_j) + H_{yR}^j \cos(\Omega t + \psi_j)]$$

which by using equations (58) and (59) and simplifying can be written as:

$$\therefore H_y = \sum_{j=1}^b [-2\Omega s \dot{\xi}^j \sin(\Omega t + \psi_j) + \int_0^R f_{yR}^j dr \cos(\Omega t + \psi_j)]$$

$$+ s \ddot{\xi}^j \cos(\Omega t + \psi_j) - s \Omega^2 \xi^j \cos(\Omega t + \psi_j) - m_b \ddot{v}] \quad (63)$$

Now using equations (38), (47), (48), writing $\sum_{j=1}^b \int_0^R f_{yR}^j dr \cos(\Omega t + \psi_j) = F_{yc}$, letting

$\sum_{j=1}^b m_b \ddot{v} = b m_b \ddot{v}$ and substituting into equation (63) yields:

$$H_y = -2\Omega s \frac{b}{2} (\dot{\xi}_s - \Omega \xi_c) + F_{yc} + s \frac{b}{2} (\ddot{\xi}_c + 2\Omega \dot{\xi}_s - \Omega^2 \xi_c) - s \Omega^2 (\frac{b}{2} \xi_c) - b m_b \ddot{v}$$

$$\therefore H_y = s \frac{b}{2} \ddot{\xi}_c - b m_b \ddot{v} + F_{yc} \quad (64)$$

The hub loads H_x and H_y now need to be added to Q_i and Q_j respectively in equations (6) and (7). Actually H_x and H_y first need to be multiplied by the fuselage mode shapes ϕ_{ihx} and ϕ_{ihy} respectively. These modes may however be normalised such that ϕ_{ihx} and ϕ_{ihy} are both unity. Then H_x and H_y can be directly used in equations (6) and (7). These equations then become:

$$M_{fx} [\ddot{u}_i + 2\zeta_i \omega_i \dot{u}_i + \omega_i^2 u_i] = Q_i - s \frac{b}{2} \ddot{\xi}_s - b m_b \ddot{u}_i - F_{xs}$$

$$\therefore (M_{fx} + b m_b) \ddot{u}_i + 2\zeta_i \omega_i M_{fx} \dot{u}_i + M_{fx} \omega_i^2 u_i + s \frac{b}{2} \ddot{\xi}_s = Q_i - F_{xs} \quad (65)$$

and

$$M_{fy} [\ddot{v}_j + 2\zeta_j \omega_j \dot{v}_j + \omega_j^2 v_j] = Q_j + s \frac{b}{2} \ddot{\xi}_c - b m_b \ddot{v}_j + F_{yc}$$

$$\therefore (M_{fy} + b m_b) \ddot{v}_j + 2\zeta_j \omega_j M_{fy} \dot{v}_j + M_{fy} \omega_j^2 v_j - s \frac{b}{2} \ddot{\xi}_c = Q_j + F_{yc} \quad (66)$$

Note: In equations (65) and (66), the Q_i and Q_j represent the generalised force in which the hub loads H_x and H_y are not included and therefore Q_i and Q_j of equations (6) and (7) are not the same as those in (65) and (66).

Equations (55), (65), and (66) can now be summarised in matrix form as:

$$\mathbf{M}\ddot{\mathbf{u}} + \mathbf{C}\dot{\mathbf{u}} + \mathbf{K}\mathbf{u} = \mathbf{f} \quad (67)$$

where the bold capital letters represent matrices and the bold small letters represent column vectors such that:

$$\mathbf{M} = \begin{bmatrix} M_{fx} + b m_b & 0 & 0 & s \frac{b}{2} \\ 0 & M_{fy} + b m_b & -s \frac{b}{2} & 0 \\ 0 & -s & M_e & 0 \\ s & 0 & 0 & M_e \end{bmatrix}$$

$$\mathbf{C} = \begin{bmatrix} 2\zeta_i \omega_i M_{fx} & 0 & 0 & 0 \\ 0 & 2\zeta_j \omega_j M_{fy} & 0 & 0 \\ 0 & 0 & 2\zeta_e \omega_e M_e & 2\Omega M_e \\ 0 & 0 & -2\Omega M_e & 2\zeta_e \omega_e M_e \end{bmatrix}$$

$$\mathbf{K} = \begin{bmatrix} M_{fx} \omega_i^2 & 0 & 0 & 0 \\ 0 & M_{fy} \omega_j^2 & 0 & 0 \\ 0 & 0 & (\omega_e^2 - \Omega^2) M_e & 2\Omega \zeta_e \omega_e M_e \\ 0 & 0 & -2\Omega \zeta_e \omega_e M_e & (\omega_e^2 - \Omega^2) M_e \end{bmatrix}$$

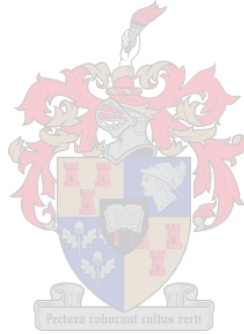
$$\mathbf{f} = \begin{bmatrix} Q_i - F_{xs} \\ Q_j + F_{ys} \\ Q_{e_c} \\ Q_{e_s} \end{bmatrix}^T$$

$$\ddot{\mathbf{u}} = \begin{bmatrix} \ddot{u}_i \\ \ddot{v}_j \\ \ddot{\xi}_c \\ \ddot{\xi}_s \end{bmatrix}^T$$

$$\dot{\mathbf{u}} = \begin{bmatrix} \dot{u}_i \\ \dot{v}_j \\ \dot{\xi}_c \\ \dot{\xi}_s \end{bmatrix}^T$$

and

$$\mathbf{u} = \begin{bmatrix} u_i \\ v_j \\ \xi_c \\ \xi_s \end{bmatrix}^T$$



In ground resonance $\mathbf{f} = \mathbf{0}$, which leaves the following coupled lag and support equations of motion describing ground resonance dynamics:

$$(M_{fx} + bm_b) \ddot{u}_i + s \frac{b}{2} \ddot{\xi}_s + 2\zeta_i \omega_i M_{fx} \dot{u}_i + M_{fx} \omega_i^2 u_i = 0$$

$$(M_{fy} + bm_b) \ddot{v}_j - s \frac{b}{2} \ddot{\xi}_c + 2\zeta_j \omega_j M_{fy} \dot{v}_j + M_{fy} \omega_j^2 v_j = 0$$

$$-s \ddot{v}_j + M_e \ddot{\xi}_c + 2\zeta_e \omega_e M_e \dot{\xi}_c + 2\Omega M_e \dot{\xi}_s + (\omega_e^2 - \Omega^2) M_e \xi_c + 2\Omega \zeta_e \omega_e M_e \xi_s = 0$$

$$s \ddot{u}_i + M_e \ddot{\xi}_s - 2\Omega M_e \dot{\xi}_c + 2\zeta_e \omega_e M_e \dot{\xi}_s - 2\Omega \zeta_e \omega_e M_e \xi_c + (\omega_e^2 - \Omega^2) M_e \xi_s = 0$$

These equations can be normalised by dividing the lag equations by the characteristic rotor inertia $I_b = \int_0^R m r^2 dr$ and dividing the support equations by $\frac{b}{2} I_b$. This yields the following four equations:

$$\begin{aligned} \frac{(M_{fx} + bm_b)}{\frac{b}{2}l_b} \ddot{u}_i + \frac{s}{\frac{b}{2}l_b} \ddot{\xi}_s + \frac{2\zeta_i \omega_i M_{fx}}{\frac{b}{2}l_b} \dot{u}_i + \frac{M_{fx} \omega_i^2}{\frac{b}{2}l_b} u_i &= 0 \\ \frac{(M_{fy} + bm_b)}{\frac{b}{2}l_b} \ddot{v}_j - \frac{s}{\frac{b}{2}l_b} \ddot{\xi}_c + \frac{2\zeta_j \omega_j M_{fy}}{\frac{b}{2}l_b} \dot{v}_j + \frac{M_{fy} \omega_j^2}{\frac{b}{2}l_b} v_j &= 0 \\ -\frac{s}{l_b} \ddot{v}_j + \frac{M_e}{l_b} \ddot{\xi}_c + \frac{2\zeta_e \omega_e M_e}{l_b} \dot{\xi}_c + \frac{2\Omega M_e}{l_b} \dot{\xi}_s + \frac{(\omega_e^2 - \Omega^2) M_e}{l_b} \xi_c + \frac{2\Omega \zeta_e \omega_e M_e}{l_b} \xi_s &= 0 \\ \frac{s}{l_b} \ddot{u}_i + \frac{M_e}{l_b} \ddot{\xi}_s - \frac{2\Omega M_e}{l_b} \dot{\xi}_c + \frac{2\zeta_e \omega_e M_e}{l_b} \dot{\xi}_s - \frac{2\Omega \zeta_e \omega_e M_e}{l_b} \xi_c + \frac{(\omega_e^2 - \Omega^2) M_e}{l_b} \xi_s &= 0 \end{aligned}$$

Now letting

$$\begin{aligned} S_\xi^* &= \frac{s}{l_b} ; \quad l_\xi^* = \frac{M_e}{l_b} ; \quad M_x^* = \frac{(M_{fx} + bm_b)}{\frac{b}{2}l_b} ; \quad M_y^* = \frac{(M_{fy} + bm_b)}{\frac{b}{2}l_b} ; \\ C_\xi^* &= \frac{2\zeta_e \omega_e}{\Omega} ; \quad C_x = \frac{2\zeta_i \omega_i M_{fx}}{\Omega} ; \quad C_y = \frac{2\zeta_j \omega_j M_{fy}}{\Omega} ; \quad C_x^* = \frac{C_x}{M_{fx} + bm_b} ; \\ C_y^* &= \frac{C_y}{M_{fy} + bm_b} ; \quad \omega_i^2 = \frac{M_{fx} + bm_b}{M_{fx}} \omega_x^2 ; \quad \omega_j^2 = \frac{M_{fy} + bm_b}{M_{fy}} \omega_y^2 , \end{aligned}$$

the preceding equations become:

$$\begin{aligned} M_x^* \ddot{u}_i + S_\xi^* \ddot{\xi}_s + \frac{\Omega C_x}{\frac{b}{2}l_b} \dot{u}_i + \frac{M_{fx} (M_{fx} + bm_b) \omega_x^2}{M_{fx} \frac{b}{2}l_b} u_i &= 0 \\ M_y^* \ddot{v}_j - S_\xi^* \ddot{\xi}_c + \frac{\Omega C_y}{\frac{b}{2}l_b} \dot{v}_j + \frac{M_{fy} (M_{fy} + bm_b) \omega_y^2}{M_{fy} \frac{b}{2}l_b} v_j &= 0 \end{aligned} \tag{68}$$

$$-S_\xi^* \ddot{v}_j + l_\xi^* \ddot{\xi}_c + \Omega C_\xi^* l_\xi^* \dot{\xi}_c + 2\Omega l_\xi^* \dot{\xi}_s + (\omega_e^2 - \Omega^2) l_\xi^* \xi_c + \Omega^2 C_\xi^* l_\xi^* \xi_s = 0$$

$$S_\xi^* \ddot{u}_i + l_\xi^* \ddot{\xi}_s - 2\Omega l_\xi^* \dot{\xi}_c + \Omega C_\xi^* l_\xi^* \dot{\xi}_s - \Omega^2 C_\xi^* l_\xi^* \xi_c + (\omega_e^2 - \Omega^2) l_\xi^* \xi_s = 0$$

for which the first two equations can be rewritten as:

$$M_x^* \ddot{u}_i + S_\xi^* \ddot{\xi}_s + \frac{\Omega C_x^* (M_{fx} + bm_b)}{\frac{b}{2} l_b} \dot{u}_i + M_x^* \omega_x^2 u_i = 0$$

$$M_y^* \ddot{v}_j - S_\xi^* \ddot{\xi}_c + \frac{\Omega C_y^* (M_{fy} + bm_b)}{\frac{b}{2} l_b} \dot{v}_j + M_y^* \omega_y^2 v_j = 0$$
(69)

In the equations of (68), the first and second time derivatives of the variables u_i , v_j , ξ_c and ξ_s are all with respect to dimensional time. If the dimensionless time variable $t^* = \Omega t$ is introduced, then:

$$dt^* = \Omega dt$$

$$\therefore dt = \frac{1}{\Omega} dt^*$$

$$\therefore \dot{u}_i = \frac{du_i}{dt} = \frac{du_i}{\frac{1}{\Omega} dt^*} = \Omega \frac{du_i}{dt^*}$$

In a similar fashion:

$$\ddot{u}_i = \Omega^2 \frac{d^2 u_i}{dt^{*2}}, \quad \dot{v}_j = \Omega \frac{dv_j}{dt^*}, \quad \ddot{v}_j = \Omega^2 \frac{d^2 v_j}{dt^{*2}}, \quad \dot{\xi}_c = \Omega \frac{d\xi_c}{dt^*},$$

$$\ddot{\xi}_c = \Omega^2 \frac{d^2 \xi_c}{dt^{*2}}, \quad \dot{\xi}_s = \Omega \frac{d\xi_s}{dt^*} \text{ and } \ddot{\xi}_s = \Omega^2 \frac{d^2 \xi_s}{dt^{*2}}.$$

Now introducing the non-dimensional time derivatives:

$$\dot{u}_i = \frac{du_i}{dt^*}, \quad \ddot{u}_i = \frac{d^2 u_i}{dt^{*2}}, \quad \dot{v}_j = \frac{dv_j}{dt^*}, \quad \ddot{v}_j = \frac{d^2 v_j}{dt^{*2}},$$

$$\dot{\xi}_c = \frac{d\xi_c}{dt^*}, \quad \ddot{\xi}_c = \frac{d^2 \xi_c}{dt^{*2}}, \quad \dot{\xi}_s = \frac{d\xi_s}{dt^*}, \quad \ddot{\xi}_s = \frac{d^2 \xi_s}{dt^{*2}}$$

and using equations (68), equations (69) can be rewritten as:

$$M_x^* \Omega^2 \ddot{u}_i + S_\xi^* \Omega^2 \ddot{\xi}_s + \Omega C_x^* M_x^* \Omega \dot{u}_i + M_x^* \omega_x^2 u_i = 0$$

$$M_y^* \Omega^2 \ddot{v}_j - S_\xi^* \Omega^2 \ddot{\xi}_c + \Omega C_y^* M_y^* \Omega \dot{v}_j + M_y^* \omega_y^2 v_j = 0$$

$$-S_\xi^* \Omega^2 \ddot{v}_j + l_\xi^* \Omega^2 \ddot{\xi}_c + \Omega C_\xi^* l_\xi^* \Omega \dot{\xi}_c + 2\Omega l_\xi^* \Omega \dot{\xi}_s$$

$$+ (\omega_e^2 - \Omega^2) l_\xi^* \xi_c + \Omega^2 C_\xi^* l_\xi^* \xi_s = 0$$
(70)

$$S_{\xi}^* \Omega^2 \ddot{u}_i + l_{\xi}^* \Omega^2 \ddot{\xi}_S - 2\Omega l_{\xi}^* \dot{\xi}_c + \Omega C_{\xi}^* l_{\xi}^* \dot{\xi}_S - \Omega^2 C_{\xi}^* l_{\xi}^* \xi_c + (\omega_e^2 - \Omega^2) l_{\xi}^* \xi_S = 0 .$$

Dividing equation (70) by Ω^2 and introducing the new variables:

$$\nu_e^2 = \frac{\omega_e^2}{\Omega^2} , \nu_x^2 = \frac{\omega_x^2}{\Omega^2} \text{ and } \nu_y^2 = \frac{\omega_y^2}{\Omega^2} , \text{ leads to:}$$

$$\begin{aligned} M_x^* \ddot{u}_i + S_{\xi}^* \ddot{\xi}_S + C_x^* M_x^* \dot{u}_i + M_x^* \nu_x^2 u_i &= 0 \\ M_y^* \ddot{v}_j - S_{\xi}^* \ddot{\xi}_c + C_y^* M_y^* \dot{v}_j + M_y^* \nu_y^2 v_j &= 0 \\ -S_{\xi}^* \ddot{v}_j + l_{\xi}^* \ddot{\xi}_c + C_{\xi}^* l_{\xi}^* \dot{\xi}_c + 2l_{\xi}^* \dot{\xi}_S + (\nu_e^2 - 1) l_{\xi}^* \xi_c + C_{\xi}^* l_{\xi}^* \xi_S &= 0 \quad (71) \\ S_{\xi}^* \ddot{u}_i + l_{\xi}^* \ddot{\xi}_S - 2l_{\xi}^* \dot{\xi}_c + C_{\xi}^* l_{\xi}^* \dot{\xi}_S - C_{\xi}^* l_{\xi}^* \xi_c + (\nu_e^2 - 1) l_{\xi}^* \xi_S &= 0 . \end{aligned}$$

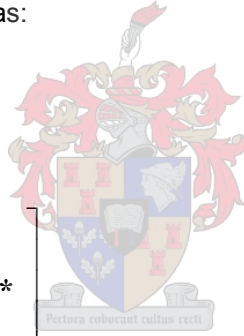
which in a matrix form can be written as:

$$\mathbf{M}^* \ddot{\mathbf{u}} + \mathbf{C}^* \dot{\mathbf{u}} + \mathbf{K}^* \mathbf{u} = \mathbf{0} \quad (72)$$

where:

$$\mathbf{M}^* = \begin{bmatrix} l_{\xi}^* & 0 & -S_{\xi}^* & 0 \\ 0 & l_{\xi}^* & 0 & S_{\xi}^* \\ -S_{\xi}^* & 0 & M_y^* & 0 \\ 0 & S_{\xi}^* & 0 & M_x^* \end{bmatrix} ,$$

$$\mathbf{C}^* = \begin{bmatrix} l_{\xi}^* C_{\xi}^* & 2l_{\xi}^* & 0 & 0 \\ -2l_{\xi}^* & l_{\xi}^* C_{\xi}^* & 0 & 0 \\ 0 & 0 & M_y^* C_y^* & 0 \\ 0 & 0 & 0 & M_x^* C_x^* \end{bmatrix} ,$$



$$\mathbf{K}^* = \begin{bmatrix} I_{\xi}^* (v_e^2 - 1) & I_{\xi}^* C_{\xi}^* & 0 & 0 \\ -I_{\xi}^* C_{\xi}^* & I_{\xi}^* (v_e^2 - 1) & 0 & 0 \\ 0 & 0 & M_y^* v_y^2 & 0 \\ 0 & 0 & 0 & M_x^* v_x^2 \end{bmatrix},$$

$$\ddot{\mathbf{u}} = [\ddot{\xi}_c, \ddot{\xi}_s, \ddot{v}_j, \ddot{u}_i]^T, \quad \dot{\mathbf{u}} = [\dot{\xi}_c, \dot{\xi}_s, \dot{v}_j, \dot{u}_i]^T,$$

$$\mathbf{u} = [\xi_c, \xi_s, v_j, u_i]^T.$$

which coincides with the matrix equation of [32, p 670, 671].

3.3 Ground Resonance Stability

3.3.1 Mathematical Problem Statement

Equation (72) represents a 4X4 second order eigenvalue problem, which can be used to investigate ground resonance stability. The problem can be stated mathematically as:

$$\left| \lambda^2 \mathbf{M}^* + \lambda \mathbf{C}^* + \mathbf{K}^* = \mathbf{0} \right| \quad (73)$$

The characteristic polynomial in λ , which is obtained from equation (73) can be written as:

$$\sum_{k=0}^8 \alpha_k \lambda^k = 0 \quad (74)$$

where

$$\alpha_8 = I_{\xi}^{*2} M_y^* M_x^* - I_{\xi}^* S_{\xi}^{*2} (M_y^* + M_x^*) + S_{\xi}^{*4}$$

$$\alpha_7 = I_{\xi}^* (I_{\xi}^* M_y^* M_x^* (2C_{\xi}^* + C_y^* + C_x^*) - S_{\xi}^{*2} (C_{\xi}^* (M_y^* + M_x^*) + M_y^* C_y^* + M_x^* C_x^*))$$

$$\alpha_6 = 1_{\xi}^* (1_{\xi}^* M_y^* M_x^* (C_{\xi}^{*2} + 2C_{\xi}^* (C_y^* + C_x^*) + 2\nu_e^2 + C_y^* C_x^* + \nu_y^2 + \nu_x^2 + 2) - S_{\xi}^{*2} (C_{\xi}^* (M_y^* C_y^* + M_x^* C_x^*) + \nu_e^2 (M_y^* + M_x^*) + M_y^* (\nu_y^2 - 1) + M_x^* (\nu_x^2 - 1)))$$

$$\alpha_5 = 1_{\xi}^* (1_{\xi}^* M_y^* M_x^* (C_{\xi}^{*2} (C_y^* + C_x^*) + 2C_{\xi}^* (\nu_e^2 + C_y^* C_x^* + \nu_y^2 + \nu_x^2 + 1) + 2\nu_e^2 (C_y^* + C_x^*) + C_y^* (\nu_x^2 + 2) + C_x^* (\nu_y^2 + 2)) - S_{\xi}^{*2} (C_{\xi}^* (M_y^* \nu_y^2 + M_x^* \nu_x^2) + (M_y^* C_y^* + M_x^* C_x^*) (\nu_e^2 - 1)))$$

$$\alpha_4 = 1_{\xi}^* (1_{\xi}^* M_y^* M_x^* (C_{\xi}^{*2} (C_y^* C_x^* + \nu_y^2 + \nu_x^2 + 1) + 2C_{\xi}^* (\nu_e^2 (C_y^* + C_x^*) + C_y^* (\nu_x^2 + 1) + C_x^* (\nu_y^2 + 1)) + \nu_e^4 + 2\nu_e^2 (C_y^* C_x^* + \nu_y^2 + \nu_x^2 - 1) + 2C_y^* C_x^* + \nu_y^2 (\nu_x^2 + 2) + 2\nu_x^2 + 1 + S_{\xi}^{*2} (M_y^* \nu_y^2 + M_x^* \nu_x^2) (1 - \nu_e^2)))$$

$$\alpha_3 = 1_{\xi}^{*2} M_y^* M_x^* (C_{\xi}^{*2} (C_y^* (\nu_x^2 + 1) + C_x^* (\nu_y^2 + 1) + 2C_{\xi}^* (\nu_e^2 (C_y^* C_x^* + \nu_y^2 + \nu_x^2) + C_y^* C_x^* + \nu_y^2 (\nu_x^2 + 1) + \nu_x^2) + \nu_e^4 (C_y^* + C_x^*) + 2\nu_e^2 (C_y^* (\nu_x^2 + 1) + C_x^* (\nu_y^2 + 1) + C_y^* (2\nu_x^2 + 1) + C_x^* (2\nu_y^2 + 1)))$$

$$\begin{aligned}
\alpha_2 &= l_\xi^{*2} M_y^* M_x^* (C_\xi^{*2} (C_y^* C_x^* + \nu_y^2 (\nu_x^2 + 1) + \nu_x^2) \\
&\quad + 2C_\xi^* (C_y^* \nu_x^2 + \nu_y^2 C_x^*) (\nu_e^2 + 1) \\
&\quad + \nu_e^4 (C_y^* C_x^* + \nu_y^2 + \nu_x^2) \\
&\quad - 2\nu_e^2 (C_y^* C_x^* + \nu_y^2 (1 - \nu_x^2) + \nu_x^2) \\
&\quad + C_y^* C_x^* + \nu_y^2 (2\nu_x^2 + 1) + \nu_x^2) \\
\alpha_1 &= l_\xi^{*2} M_y^* M_x^* (C_\xi^{*2} (C_y^* \nu_x^2 + \nu_y^2 C_x^*) + 2C_\xi^* \nu_y^2 \nu_x^2 (\nu_e^2 + 1) \\
&\quad + (C_y^* \nu_x^2 + \nu_y^2 C_x^*) (\nu_e^4 - 2\nu_e^2 + 1)) \\
\alpha_0 &= l_\xi^{*2} ((\nu_e^2 - 1)^2 + C_\xi^{*2}) M_y^* \nu_y^2 M_x^* \nu_x^2
\end{aligned}$$

The solution of this eighth order polynomial gives eight eigenvalues, some of which may appear as complex conjugate pairs. From the sign of the real parts, the ground resonance stability can be judged.

3.3.2 Divergence Instability

Considering a divergence-type instability, the following must be noted:

A divergence-instability occurs when a real root of the characteristic equation passes through the origin of the plane, which contains all the eigenvalues of a system. The divergence stability boundary is thus defined by the requirement that one root be $\lambda = 0$, for which the characteristic equation, which according to equation (74) is only possible if $\alpha_0 = 0$, i.e. if

$$l_\xi^{*2} [(\nu_e^2 - 1)^2 + C_\xi^{*2}] M_y^* \nu_y^2 M_x^* \nu_x^2 = 0$$

An alternative, but equivalent, definition of the stability boundary is that $\det(\mathbf{K}^*) = 0$, for which it can be seen, from equation (72), that the same expression, as the one above, is obtained. The criterion for a system, in which divergent instability does not occur, is that $\det(\mathbf{K}^*) > 0$, which means that the quantity on the left-hand side of the above equation must always be positive. Therefore:

$$l_\xi^{*2} [(\nu_e^2 - 1)^2 + C_\xi^{*2}] M_y^* \nu_y^2 M_x^* \nu_x^2 > 0$$

The above equation is always satisfied (assuming that, simultaneously $\nu_e \neq 1$ and $C_\xi^* \neq 0$) and therefore, under these assumptions, a divergence type instability is not possible for this system [32, p 671].

Note: The assumption that, simultaneously $\nu_e \neq 1$ and $C_{\xi}^* \neq 0$ is reasonable for typical helicopters as ω_e is unlikely to be equal to Ω and ζ_e or ω_e are unlikely to be equal to zero.

3.3.3 Uncoupled Dynamics

Consider the uncoupled dynamics, which can be obtained by setting S_{ξ}^* equal to zero. Although

this is not physically possible, from the definition of S_{ξ}^* , it is assumed to be zero in order to investigate its effect. The uncoupled hub motion consists of damped oscillations with natural frequencies ν_x and ν_y , which is given by the first two expressions in equation (71). Assuming

$S_{\xi}^* = 0$, dividing the first equation by M_x^* and dividing the second equation by M_y^* yields:

$$\ddot{u}_1 + C_x^* \dot{u}_1 + \nu_x^2 u_1 = 0$$

and (75)

$$\ddot{v}_j + C_y^* \dot{v}_j + \nu_y^2 v_j = 0$$

which, in terms of the Laplace variable, s , can be written as:

$$s^2 + C_x^* s + \nu_x^2 = 0$$
(76)

and

$$s^2 + C_y^* s + \nu_y^2 = 0$$
(77)

For equation (76), it follows that:

$$s_{1,2} = \frac{-C_x^* \pm \sqrt{C_x^{*2} - 4\nu_x^2}}{2} = \frac{-C_x^*}{2} \pm \sqrt{\left(\frac{C_x^*}{2}\right)^2 - \nu_x^2}$$

$$\therefore s_{1,2} = \frac{-C_x^*}{2} \pm i \sqrt{\nu_x^2 - \left(\frac{C_x^*}{2}\right)^2}$$
(78)

and similarly for equation (77):

$$s_{1,2} = \frac{-C_y^*}{2} \pm i \sqrt{\nu_y^2 - \left(\frac{C_y^*}{2}\right)^2}$$
(79)

For both equations (78) and (79) light damping is assumed.

The uncoupled lag motion is also a damped oscillation given by equation (35), which is in a dimensional form. Dividing equation (35) by $\Omega^2 M_e$, rewriting $2\zeta_e \omega_e = \Omega C_{\xi}^*$ and $\nu_e = \frac{\omega_e}{\Omega^2}$,

letting $s = \int_0^R m \phi_e dr = 0$, $Q_e = 0$ and introducing the non-dimensional time derivatives, as previously, yields:

$$\ddot{\xi} + C_{\xi}^* \dot{\xi} + \nu_e^2 \xi = 0$$

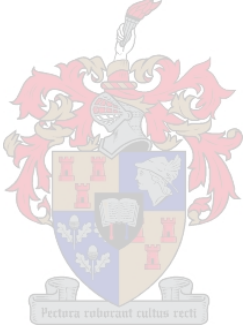
Using exactly the same procedure as for equations (76) and (77), gives:

$$s^2 + C_{\xi}^* s + \nu_e^2 = 0 \text{ from which follows:}$$

$$s_{1,2R} = \frac{-C_{\xi}^*}{2} \pm i \sqrt{\nu_e^2 - \left(\frac{C_{\xi}^*}{2}\right)^2} \quad (80)$$

in the rotating frame.

In the non-rotating reference frame, there are two cyclic lag modes, with eigenvalues $s_{NR} = s_{1R} \pm i$ [32, p 672]. Thus for $S_{\xi}^* = 0$ the characteristic equation factors into a product of the rotor and support characteristic equations with the solutions:

$$s = \begin{cases} -\frac{C_{\xi}^*}{2} + i \sqrt{\nu_e^2 - \left(\frac{C_{\xi}^*}{2}\right)^2} \pm i \\ -\frac{C_y^*}{2} + i \sqrt{\nu_y^2 - \left(\frac{C_y^*}{2}\right)^2} \\ -\frac{C_x^*}{2} + i \sqrt{\nu_x^2 - \left(\frac{C_x^*}{2}\right)^2} \end{cases} \quad (81)$$


and their complex conjugates.

Since all of these roots of the characteristic equation have negative real parts, they all lie to the left of the imaginary axis (i.e. the left half of the s-plane). This implies that the uncoupled rotor and support motion is stable and a ground resonance instability can only be due to the inertial coupling when $S_{\xi}^* \neq 0$. When there is no damping and $S_{\xi}^* = 0$ as well, it can be seen from equation (81) that the solution is $s = \pm i\omega$ for frequencies $\omega = \nu_e \pm 1, \nu_x$ and ν_y .

3.3.4 Coupled Dynamics

The coupling of the rotor and support is determined, as was seen above, by the parameter R
 $s = \int_0^R m \phi_e dr$ (not to be confused with the Laplace variable 's'). For an articulated rotor, with a relatively homogenous spanwise mass distribution, s is the product of the blade mass, a constant, which depends on how ϕ_e was normalised, and the radial distance of the blade centre of gravity from the lead-lag hinge. Consider the following ratio:

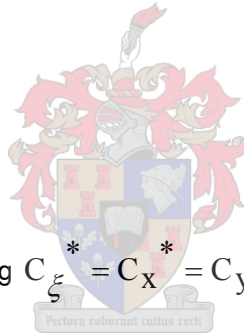
$$\frac{S_{\xi}^{*2}}{(I_{\xi}^{*} M_y^{*})} = \frac{\frac{s^2}{l_b^2}}{\frac{M_e}{l_b} \frac{M_{fy} + bm_b}{\frac{b}{2} l_b}} = \frac{b}{2} \frac{s^2}{M_e (M_{fy} + bm_b)} \cong \frac{b}{2} \frac{s^2}{M_e M_{fy}} \quad (\text{as the support mass})$$

is much larger than the blade mass). Here again $I_{\xi}^{*} = \frac{M_e}{l_b}$ and $M_e = \int_0^R m \phi_e^2 dr$. Since 's' is

associated with the blade mass, the ratio $\frac{S_{\xi}^{*2}}{(I_{\xi}^{*} M_y^{*})}$ can be seen as an approximate ratio

between the rotor mass and the support mass, which will be quite small. While an exact analytical solution of the eighth order ground resonance characteristic equation is not possible, useful results can be obtained on the basis of this assumption i.e, that S_{ξ}^{*} is small (really that

$$\frac{S_{\xi}^{*2}}{(I_{\xi}^{*} M_y^{*})} \ll 1) \quad [32, p 673].$$



3.3.5 The No Damping Case

The No Damping Case requires setting $C_{\xi}^{*} = C_x^{*} = C_y^{*} = 0$ in equation (74) and yields:

$$\sum_{k=0}^8 \alpha_k \lambda^k = 0 \quad \text{with}$$

$$\alpha_8 = I_{\xi}^{*2} M_y^{*} M_x^{*} - I_{\xi}^{*} S_{\xi}^{*2} (M_y^{*} + M_x^{*}) + S_{\xi}^{*4}$$

$$\alpha_7 = 0$$

$$\alpha_6 = I_{\xi}^{*2} M_y^{*} M_x^{*} (2v_e^2 + v_y^2 + v_x^2 + 2) -$$

$$S_{\xi}^{*2} (v_e^2 (M_y^{*} + M_x^{*}) + M_y^{*} (v_y^2 - 1) + M_x^{*} (v_x^2 - 1))$$

$$\alpha_5 = 0$$

$$\alpha_4 = l_\xi^{*2} M_y^* M_x^* (\nu_e^4 + 2\nu_e^2(\nu_y^2 + \nu_x^2 - 1) + \nu_y^2(\nu_x^2 + 2) + 2\nu_x^2 + 1) + S_\xi^{*2} (M_y^* \nu_y^2 + M_x^* \nu_x^2)(1 - \nu_e^2)$$

$$\alpha_3 = 0$$

$$\alpha_2 = l_\xi^{*2} M_y^* M_x^* (\nu_e^4(\nu_y^2 + \nu_x^2) - 2\nu_e^2(\nu_y^2(1 - \nu_x^2) + \nu_x^2) + \nu_y^2(2\nu_x^2 + 1) + \nu_x^2)$$

$$\alpha_1 = 0$$

$$\alpha_0 = l_\xi^{*2} (\nu_e^2 - 1)^2 M_y^* \nu_y^2 M_x^* \nu_x^2$$

Replacing λ by the Laplace variable 's' and dividing by $l_\xi^{*2} M_y^* M_x^*$ yields:

$$\sum_{k=0}^8 \alpha_k s^k = 0 \quad \text{with} \quad (82)$$

$$\alpha_8 = 1 - \frac{S_\xi^{*2}}{l_\xi^{*2} M_y^* M_x^*} (M_y^* + M_x^*) + \frac{S_\xi^{*4}}{l_\xi^{*2} M_y^* M_x^*}$$

$$\alpha_7 = 0$$

$$\alpha_6 = 2\nu_e^2 + \nu_y^2 + \nu_x^2 + 2 - \frac{S_\xi^{*2}}{l_\xi^{*2} M_y^* M_x^*} (\nu_e^2(M_y^* + M_x^*) + M_y^*(\nu_y^2 - 1) + M_x^*(\nu_x^2 - 1))$$

$$\alpha_5 = 0$$

$$\alpha_4 = \nu_e^4 + 2\nu_e^2(\nu_y^2 + \nu_x^2 - 1) + \nu_y^2(\nu_x^2 + 2) + 2\nu_x^2 + 1 + S_\xi^{*2} (M_y^* \nu_y^2 + M_x^* \nu_x^2)(1 - \nu_e^2)$$

$$\alpha_3 = 0$$

$$\alpha_2 = \nu_e^4(\nu_y^2 + \nu_x^2) - 2\nu_e^2(\nu_y^2(1 - \nu_x^2) + \nu_x^2) + \nu_y^2(2\nu_x^2 + 1) + \nu_x^2$$

$$\alpha_1 = 0$$

$$\alpha_0 = (\nu_e^2 - 1)^2 \nu_y^2 \nu_x^2$$

The eigenvalues of this polynomial with real coefficients must appear as complex conjugate pairs, as was the case for equation (74). As can be seen from equation (82), the characteristic equation for the no damping case is actually a polynomial in s^2 as $\alpha_k = 0$ for $k=1,3,5,7$. Letting $s = i\omega$ or $s^2 = -\omega^2$ yields a polynomial in ω^2 that also has real coefficients. Since equation (82) can be written as a polynomial in ω^2 with real coefficients, the roots $(\omega^2)_j$ are of the form

$\omega^2 = \theta \pm i\zeta$. Therefore $\omega = \pm\sqrt{\theta \pm i\zeta}$ and it follows that complex solutions of the characteristic equation with zero damping will occur in groups of four roots, symmetric about both the real and imaginary s-axes and there will be one root in each quadrant of the s-plane. Since two of these roots will be in the right half-plane ($\text{Re}(s) > 0$), such complex solutions correspond to an unstable system. Furthermore, there is no way that the system can be stable, with all the roots in the left half-plane. The requirement of symmetry about the imaginary axis will be satisfied, however, if all the roots are on the imaginary axis, which corresponds to neutral stability. Neutral stability is the best that can be achieved when there is no damping in the rotor or support [32, p 674].

Before substituting $s = i\omega$ into equation (82), it is convenient to re-write most of equation (82) in terms of s^2 as in [32, p. 674], which yields:

$$[(s^2 + \nu_e^2 - 1)^2 + 4s^2](s^2 + \nu_y^2)(s^2 + \nu_x^2) - \frac{S_\xi^{*2}}{I_\xi^* M_y^* M_x^*} s^4 [M_y^* (s^2 + \nu_y^2) + M_x^* (s^2 + \nu_x^2)] + \frac{S_\xi^{*4}}{I_\xi^{*2} M_y^* M_x^*} s^8 = 0 \quad (83)$$

Equation (82) and (83) are two equivalent forms of the same equation. Now substituting $s = i\omega$ into equation (83) yields:

$$[(\nu_e^2 - 1 - \omega^2)^2 - 4\omega^2](\nu_y^2 - \omega^2)(\nu_x^2 - \omega^2) - \frac{S_\xi^{*2}}{I_\xi^* M_y^* M_x^*} \omega^4 [M_y^* (\nu_y^2 - \omega^2) + M_x^* (\nu_x^2 - \omega^2)] + \frac{S_\xi^{*4}}{I_\xi^{*2} M_y^* M_x^*} \omega^8 = 0 \quad (84)$$

To obtain an analytical solution of equation (84) it is assumed that the coupling parameter S_ξ is small. The roots for small coupling should then near the exact solution for $S_\xi = 0$:

$\omega = \nu_e \pm 1, \nu_x$ or ν_y , which was obtained from equation (81) with no damping and $S_\xi^* = 0$ for uncoupled dynamics.

As the coupling parameter S_ξ is assumed small, it will not be equal to zero and a correction factor needs to be added to the uncoupled roots. Letting the correction factor be $S_\xi^{*2} s_1$ and

considering the solution near $\omega = \nu_X$, the eigenvalues can be written as $\omega^2 = \nu_X^2 + S_\xi^{*2} s_1$.

Then equation (84) becomes:

$$[(\nu_e^2 - 1 - (\nu_X^2 + S_\xi^{*2} s_1))^2 - 4(\nu_X^2 + S_\xi^{*2} s_1)](\nu_y^2 - (\nu_X^2 + S_\xi^{*2} s_1))(\nu_X^2 - (\nu_X^2 + S_\xi^{*2} s_1)) - (\nu_e^2 - 1 - (\nu_X^2 + S_\xi^{*2} s_1))(\nu_X^2 + S_\xi^{*2} s_1)^2 \frac{S_\xi^{*2}}{I_\xi^* M_y^* M_x^*} [M_y^* (\nu_y^2 - (\nu_X^2 + S_\xi^{*2} s_1)) + M_x^* (\nu_X^2 - (\nu_X^2 + S_\xi^{*2} s_1))] + \frac{S_\xi^{*4}}{I_\xi^{*2} M_y^* M_x^*} (\nu_X^2 + S_\xi^{*2} s_1)^4 = 0$$

Neglecting the terms of S_ξ^{*} of higher order than 2, results in:

$$[(\nu_e^4 - 2\nu_e^2 - 2\nu_e^2 \nu_X^2 + 1 + 2\nu_X^2 + \nu_X^4 - 4\nu_X^2)](\nu_y^2 - \nu_X^2)(-S_\xi^{*2} s_1) - (\nu_e^2 - 1 - \nu_X^2) \nu_X^4 \frac{S_\xi^{*2}}{I_\xi^* M_y^* M_x^*} [M_y^* (\nu_y^2 - \nu_X^2)] = 0$$

Dividing by S_ξ^{*2} yields:

$$[\nu_e^4 - 2\nu_e^2 - 2\nu_e^2 \nu_X^2 + 1 + 2\nu_X^2 + \nu_X^4 - 4\nu_X^2](\nu_y^2 - \nu_X^2)(-s_1) - (\nu_e^2 - 1 - \nu_X^2) \nu_X^4 \frac{1}{I_\xi^* M_y^* M_x^*} [M_y^* (\nu_y^2 - \nu_X^2)] = 0$$

and then to the lowest order of S_ξ^{*2} or S_ξ^{*2} the characteristic equation is:

$$[(\nu_e^2 - 1 - \nu_X^2)^2 - 4\nu_X^2](\nu_y^2 - \nu_X^2)(-s_1) - (\nu_e^2 - 1 - \nu_X^2) \nu_X^4 \frac{1}{I_\xi^* M_y^* M_x^*} M_y^* (\nu_y^2 - \nu_X^2) = 0$$

$$\therefore s_1 = -\frac{1}{I_\xi^* M_x^*} \frac{(\nu_e^2 - 1 - \nu_X^2) \nu_X^4}{(\nu_e^2 - 1 - \nu_X^2)^2 - 4\nu_X^2}$$

Now since $\omega^2 = \nu_X^2 + S_\xi^{*2} s_1$:

$$\omega^2 = \nu_x^2 - \frac{S_\xi^{*2}}{I_\xi^* M_X^*} \frac{(\nu_e^2 - 1 - \nu_x^2) \nu_x^4}{(\nu_e^2 - 1 - \nu_x^2)^2 - 4\nu_x^2}$$

$$\therefore \omega^2 = \nu_x^2 \left[1 - \frac{(\nu_e^2 - 1 - \nu_x^2) \nu_x^2}{(\nu_e^2 - 1 - \nu_x^2)^2 - 4\nu_x^2} \frac{S_\xi^{*2}}{I_\xi^* M_X^*} \right] \quad (85)$$

The order S_ξ^{*2} solution near $\omega = \nu_y$ is similar. For the solution near $\omega = \nu_e \pm 1$, using

$\omega^2 = (\nu_e \pm 1)^2 + S_\xi^{*2} s_1$, and following the same procedure as previously, the characteristic equation, to the lowest order in S_ξ^{*2} can be given by:

$$s_1 2\nu_e [\nu_y^2 - (\nu_e \pm 1)^2] [\nu_x^2 - (\nu_e \pm 1)^2]$$

$$+ (\nu_e \pm 1)^5 \frac{1}{I_\xi^* M_Y^* M_X^*} \{M_Y^* [\nu_y^2 - (\nu_e \pm 1)^2] + M_X^* [\nu_x^2 - (\nu_e \pm 1)^2]\} = 0$$

Then solving for s_1 and using $\omega^2 = (\nu_e \pm 1)^2 + S_\xi^{*2} s_1$ yields:

$$\omega^2 = (\nu_e \pm 1)^2 \left[1 - \frac{(\nu_e \pm 1)^3}{2\nu_e} \frac{M_Y^* [\nu_y^2 - (\nu_e \pm 1)^2] + M_X^* [\nu_x^2 - (\nu_e \pm 1)^2]}{[\nu_y^2 - (\nu_e \pm 1)^2] [\nu_x^2 - (\nu_e \pm 1)^2]} \frac{S_\xi^{*2}}{I_\xi^* M_Y^* M_X^*} \right] \quad (86)$$

Now consider the limit $\Omega = 0$, where Ω is the rotor speed. The dimensional lag frequency is given by: $\omega_e^2 = K_1 + K_2 \Omega^2$ [32, p. 673] and the dimensional lag frequency at zero rotational speed, ω_0 , is given by: $\omega_0 = \sqrt{K_1}$. The dimensionless support natural frequencies, ν_x and ν_y , vary inversely with the rotor speed for a fixed dimensional frequency and therefore become infinite in the limit $\Omega = 0$. Now the solution near $\omega = \nu_x$ (equation (85)) in a dimensional form can be written as:

$$\frac{\omega^2}{\Omega^2} = \frac{\omega_x^2}{\Omega^2} \left[1 - \frac{\left(\frac{\omega_e^2}{\Omega^2} - 1 - \frac{\omega_x^2}{\Omega^2}\right) \frac{\omega_x^2}{\Omega^2}}{\left(\frac{\omega_e^2}{\Omega^2} - 1 - \frac{\omega_x^2}{\Omega^2}\right)^2 - 4 \frac{\omega_x^2}{\Omega^2}} \frac{S_\xi^{*2}}{I_\xi^* M_X^*} \right]$$

$$\therefore \frac{\omega^2}{\Omega^2} = \frac{\omega_x^2}{\Omega^2} - \frac{\left(\frac{\omega_e^2 - \Omega^2 - \omega_x^2}{\Omega^2}\right) \frac{\omega_x^4}{\Omega^4}}{\left(\frac{\omega_e^2 - \Omega^2 - \omega_x^2}{\Omega^2}\right)^2 - 4 \frac{\omega_x^2}{\Omega^2}} \frac{S_\xi^{*2}}{I_\xi^* M_X^*}$$

$$\therefore \frac{\omega^2}{\Omega^2} = \frac{\omega_x^2}{\Omega^2} - \frac{\frac{(\omega_e^2 - \Omega^2 - \omega_x^2) \omega_x^4}{\Omega^6}}{\frac{(\omega_e^2 - \Omega^2 - \omega_x^2)^2 - 4\omega_x^2 \Omega^2}{\Omega^4}} \frac{S_\xi^{*2}}{I_\xi^* M_X^*}$$

and then in the limit $\Omega = 0$:

$$\omega^2 = \lim_{\Omega \rightarrow 0} \omega_x^2 - \frac{(\omega_e^2 - \Omega^2 - \omega_x^2) \omega_x^4}{(\omega_e^2 - \Omega^2 - \omega_x^2)^2 - 4\omega_x^2 \Omega^2} \frac{S_\xi^{*2}}{I_\xi^* M_X^*}$$

$$= \omega_x^2 - \frac{\omega_x^4}{(\omega_e^2 - \omega_x^2)} \frac{S_\xi^{*2}}{I_\xi^* M_X^*}$$

$$\therefore \omega^2 = \omega_x^2 - \frac{\omega_x^4}{(\omega_0^2 - \omega_x^2)} \frac{S_\xi^{*2}}{I_\xi^* M_X^*} \quad (\omega_e \approx \omega_0 \text{ as } \Omega \rightarrow 0)$$

and therefore the solution near $\omega = \omega_x$ in the limit $\Omega = 0$ can be given by:

$$\omega^2 = \omega_x^2 \left[1 + \frac{\omega_x^2}{(\omega_x^2 - \omega_0^2)} \frac{S_\xi^{*2}}{I_\xi^* M_X^*} \right] \quad (87)$$

in terms of dimensional frequencies. Hence the solution ω^2 is increased at low rotor speed, if $\omega_x > \omega_0$ and decreased if $\omega_x < \omega_0$.

Following the same procedure i.e. writing equation (86) in a dimensional form, taking the limit $\Omega \rightarrow 0$ and remembering that $\omega_e \approx \omega_0$ as $\Omega \rightarrow 0$, the solution near $\omega = \omega_e^2 \pm \Omega$, can be given by:

$$\omega^2 = \omega_0^2 \left[1 - \frac{\omega_0^2}{2} \frac{M_y^* [\omega_y^2 - \omega_0^2] + M_x^* [\omega_x^2 - \omega_0^2]}{(\omega_y^2 - \omega_0^2)(\omega_x^2 - \omega_0^2)} \frac{S_\xi^{*2}}{I_\xi^* M_X^* M_y^*} \right] \quad (88)$$

in terms of dimensional frequencies.

The direction of the shift in ω^2 depends on the magnitude of the lag frequency at zero rotational speed, ω_0 relative to the support frequencies ω_x and ω_y .

Now consider the limit of large rotor speed. In terms of the dimensionless frequencies, ν_x and ν_y approach zero proportionally to Ω^{-1} and the solution near $\omega = \nu_x$ for Ω approaching infinity, from equation (85), is given by:

$$\omega^2 = \nu_x^2 \left[1 - \frac{\nu_x^2}{\nu_e^2 - 1} \frac{S_\xi^{*2}}{I_\xi^* M_x^*} \right] \quad (89)$$

so that the solution ω^2 is increased if $\nu_e < 1$.

The solution near $\omega = \nu_e \pm 1$, for Ω approaching infinity, is obtained by letting ν_x and ν_y approach zero in equation (86), which yields:

$$\omega^2 = (\nu_e \pm 1)^2 \left[1 - \frac{(\nu_e \pm 1)^3}{2\nu_e} \frac{[-M_y^* (\nu_e \pm 1)^2 - M_x^* (\nu_e \pm 1)^2]}{(-(\nu_e \pm 1)^2)(-(\nu_e \pm 1)^2)} \frac{S_\xi^{*2}}{I_\xi^* M_x^* M_y^*} \right]$$

$$\therefore \omega^2 = (\nu_e \pm 1)^2 \left[1 + \frac{(\nu_e \pm 1)}{2\nu_e} (M_y^* + M_x^*) \frac{S_\xi^{*2}}{I_\xi^* M_x^* M_y^*} \right] \quad (90)$$

so ω^2 is increased for the $\omega = \nu_e + 1$ solution and also for the $\omega = \nu_e - 1$ solution if $\nu_e > 1$.

Finally consider the limit $\omega = 0$, for which the characteristic equation (84) becomes:

$$[(\nu_e^2 - 1)^2] \nu_y^2 \nu_x^2 = 0 \quad (\text{considering only the positive lag frequency}) \quad (91)$$

$$\therefore \nu_e = 1$$

With the rotor speed as a parameter, the $\omega = 0$ solution defines where the roots intercept the Ω -axis, namely at the rotor speed for which $\nu_e = 1$. The same result is obtained in the uncoupled ($S_\xi^* = 0$) case for $\omega = \nu_e - 1$. This result shows that the low frequency lag mode root intercepts the Ω -axis at the same point for all values of S_ξ .

Plotting the dimensional frequencies ω (the roots of the characteristic equation) as a function of the rotor speed, Ω , yields the graphical ground resonance solution for the case of no damping in a form known as a Coleman diagram. The dimensional solution for the uncoupled case ($S_\xi = 0$) is $\omega = \omega_x, \omega_y, \Omega \pm \omega_e$, plus the corresponding negative frequencies, which give a total of eight roots. (The negative solutions for ω are the mirror images of the positive solutions, and are therefore not plotted). The solution for $S_\xi > 0$ can be sketched using the previous results for the

influence of small S_ξ in the limits $\Omega = 0$ and $\Omega = \infty$, given by equations (87) to (91). Figure 3.3.1 represents the Coleman diagram for an articulated rotor. This sketch is the typical result for

small coupling ($\frac{S_\xi}{I_\xi M_y} \ll 1$) [32, p. 678].

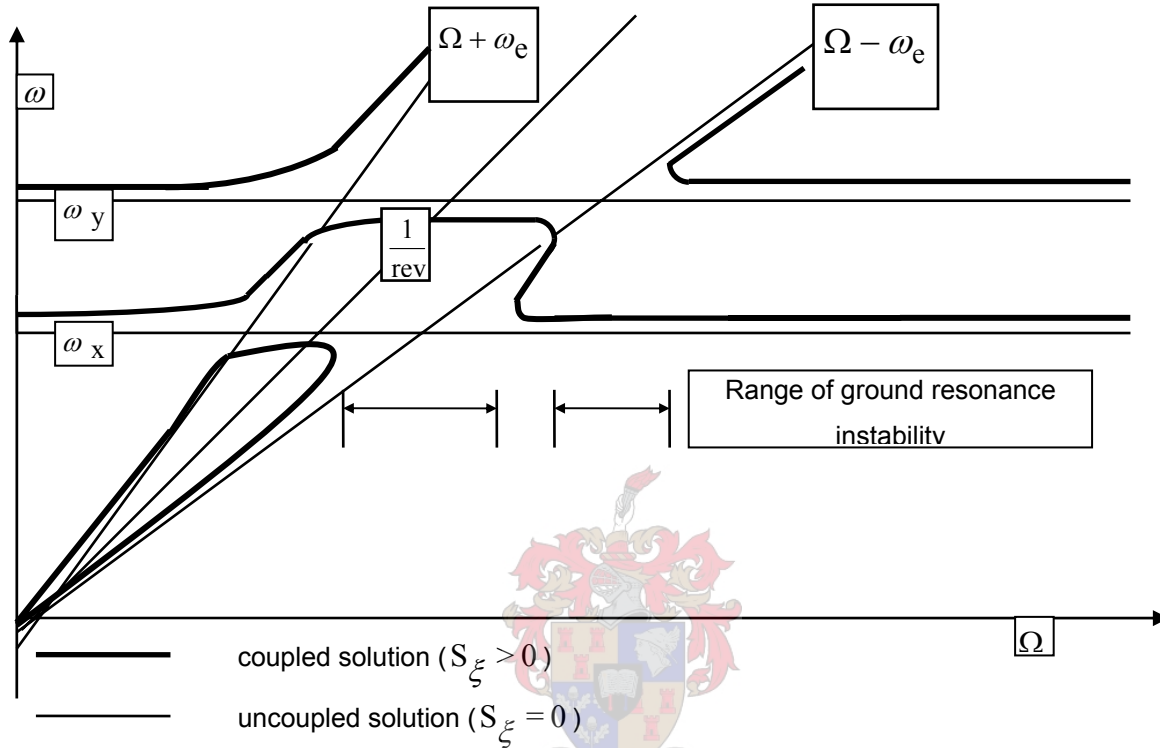


Figure 3.3.1 Coleman diagram of the ground resonance solution for an articulated rotor

The uncoupled roots for the support modes are the horizontal lines at $\omega = \omega_x$ and $\omega = \omega_y$, and the uncoupled roots for the rotor are the low and high frequency rotor modes at $\omega = \omega_e \pm \Omega$. For $S_\xi > 0$, the solution is displaced from the uncoupled frequencies, as indicated in Figure 3.3.1. There are two ranges of Ω where only two positive real solutions for ω exist, occurring around the frequency coalescence of the low frequency lag mode ($\Omega - \omega_e$) with a support mode (ω_x or ω_y). The characteristic equation has four complex solutions in these ranges, which indicates that the system is unstable if the rotating natural frequency ω_e is below $\frac{1}{\text{rev}}$. Thus the placement of the rotor lag frequency determines whether or not a ground resonance instability can occur.

Another commonly used graphical representation of the uncoupled fuselage and blade frequencies is the Southwell diagram of an articulated rotor with lead-lag springs and dampers shown in figure 3.3.2.

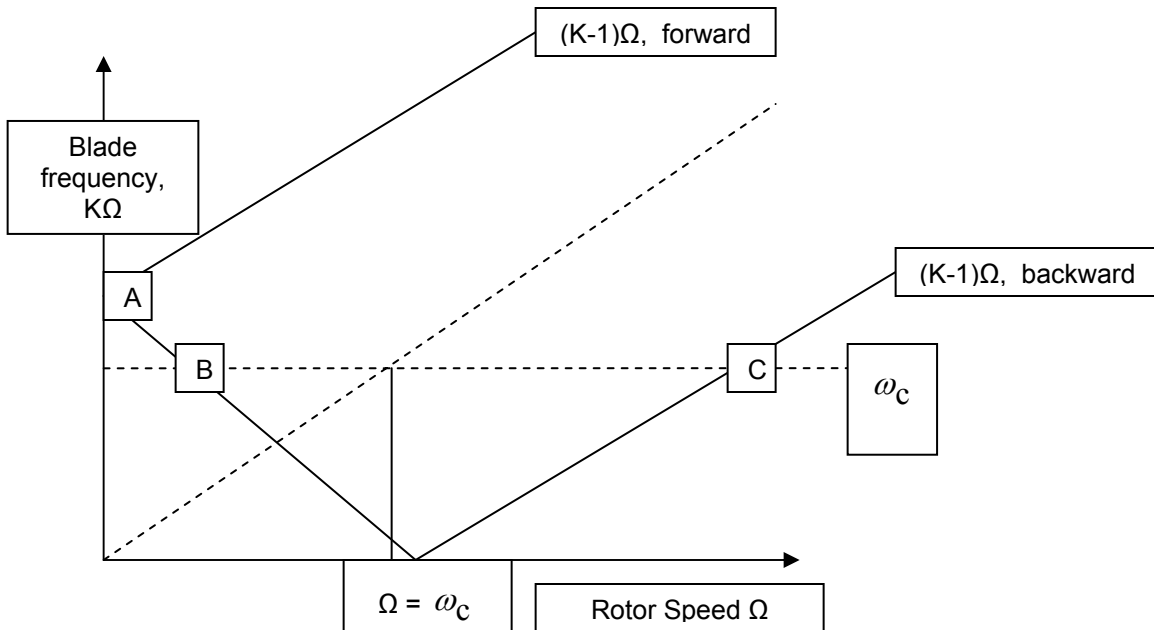


Figure 3.3.2 Southwell diagram of the uncoupled fuselage and main rotor blade frequencies

In figure 3.3.2 the horizontal line labelled ω_c represents one of the natural frequencies of the rotor support system. The point A represents the blade frequency when the rotor is stationary and is higher than the constant fuselage frequency. As the rotor speed increases, the backward lag motion $(K-1)\Omega$ intersects the fuselage frequency at B and C. Point B cannot lead to instability and ground resonance, if it occurs, it is only associated with point C [35, p382]. This fact is used in the later numerical analysis to determine the main rotor speed at which ground resonance may occur in the Rooivalk model.

Ground resonance stability with articulated rotors is achieved by providing a sufficient level of damping of the rotor lag motion and of the support motion. Instabilities can also be avoided by a proper placement of the natural frequencies of the airframe to avoid resonances, but usually there are too many other constraints on the structural design for this to be a practical means of handling the ground resonance problem. For articulated rotors, various basic means of combating ground resonance exist. These include:

- 1) The installation of special dampers on the lag hinges of the rotor blades which damp the blade vibrations in the plane of rotation.
- 2) The introduction of special damping elements in the design of the shock absorber strut or the proper selection of the characteristics of the hydraulic resistance of the shock absorber struts in forward and reverse strokes, and also the characteristics of rigidity of the shock absorber struts and pneumatic tires.

The proper selection of the characteristics of the blade dampers and the characteristics of the rigidity and damping of the landing gear is the main purpose of performing calculations on a specific helicopter to avoid ground resonance.

4. Numerical Analysis with Time Domain Simulation using a Multi-body Dynamics Analysis Program: DYMORE

4.1 General Description of the DYMORE Program

The DYMORE (Dynamic Modal Reduction) program was developed by the Centre of Excellence in Rotorcraft Technology, Rensselaer Polytechnic Institute in Troy, New York during 1994. The program affords a nonlinear multi-body dynamic analysis, using a finite element method and was specifically developed for helicopter modelling. The most important element of the DYMORE program is the advanced beam element, which is used to model, both the fuselage and the rotor structure as well as their various sub-components that may play a role in the analysis. All interconnecting bodies are treated as essentially elastic bodies.

The program itself consists of three modules, namely PREFEM, FEMANA, PSTFEM, and a pre-processor module called CROSEC. The CROSEC module performs a two dimensional cross-sectional finite element analysis of beam cross-sections in order to compute the sectional stiffness and mass properties of the beams. The CROSEC module is, however, not a prerequisite for the dynamic analysis to be performed, as the cross-sectional stiffness and inertia properties of the beams can be supplied directly to the program, should they be known.

For the analysis of the Rooivalk model, the values were supplied by Aerospatiale and interpolated to coincide with specific nodal points of the beams representing the rotor blades. The blade that is simulated in this manner is the Super Puma blade, 332A.04.11.0024.01, as implemented on the Rooivalk Combat Support Helicopter. The required values are supplied to the PREFEM module in the appropriate fields allocated for them.

PREFEM together with FEMANA and PSTFEM comprise the three main independent program units allowing for pre-processing, the actual finite element analysis and post-processing. These three units communicate through a series of unformatted binary files, each containing essential information for the subsequent program unit. The PREFEM unit defines all of the elements of the structure to be analysed, the FEMANA unit performs the actual finite element analysis, both for the static as well as the dynamic case and the PSTFEM unit performs the post processing of the finite element analysis. All three of the main modules require specific inputs and in some instances these inputs are required in a predetermined format. A more detailed description of each of these modules is therefore required.

4.2 Detailed Description of the DYMORE Modules

4.2.1 The PREFEM Module

This module is the first independent program unit and acts as the pre-processing module for the finite element analysis in which all of the elements of the three-dimensional model are defined. The module consists of 21 blocks, in which the following parameters are defined:

- a. Global control parameters for the pre-processor
- b. Global nodal co-ordinates, sets of three mutually orthogonal unit vectors (triads) and boundary conditions
- c. Variable node number blade elements, which are naturally curved and twisted iso-parametric beam elements that include transverse shearing and torsional warping deformations
- d. Rigid bodies (concentrated inertia assigned to a single node of the model, which have no stiffness contribution)
- e. Flexible joints (concentrated stiffnesses between two nodes of the model with no inertial contribution)

- f. Prescribed displacements in which the time history of specific displacement components of the model are prescribed
- g. Linear constraints amongst various displacement components of the model
- h. Revolute joints (elements that enforce a constraint between the rotations of two nodes of the model along a given vector)
- i. Prismatic joints (elements that enforce a constraint between the displacement of two nodes of the model)
- j. Universal joints (elements that enforce a constraint between the rotations of two nodes of the model by allowing two relative rotations and constraining a third)
- k. Sliding joints (elements that enforce a constraint between the displacement of several nodes of the model)
- l. Link elements (elements that enforce a constraint between the translations of two nodes of the model)
- m. Time integration control parameters, time step size, harmonic and user defined functions used to describe the time evolution of applied loads or prescribed displacements
- n. Dead loading cases in which the orientation of the loading is fixed in space
- o. Gravitational forces
- p. Characteristics of each elastic body
- q. Nonlinear spring and/or damper properties
- r. Physical air properties and standard aerofoil coefficients
- s. Properties of airfoils
- t. Lifting rotor elements
- u. Aerodynamic reference lines and air stations

From these parameters PREFEM calculates a global connectivity array of the described problem and all the data required to generate the structural and air load elements is evaluated. The output file created by the PREFEM module serves as the input file for the FEMANA module [18].

4.2.2 The FEMANA Module

This DYMORE module performs the actual finite element static and dynamic analysis. In the quasi-static analysis, the loading on the model consists of specified dead loads, spin rate and aerodynamic loading. The program calculates the static equilibrium position of the structure under the applied loads. FEMANA can then calculate the natural frequencies about this steady equilibrium position if required by the user. Dynamic analysis is performed with step by step time integration under time varying loads. This is done by means of two different time integration schemes, both of which are related to the preservation of the total energy of the system in order to guarantee the unconditional stability of the integration process.

The first scheme, the normal energy preserving time integration scheme, may suffer from convergence problems when the complexity of the constrained multi-body system increases. Therefore, a second integration scheme, which is based on an energy-decaying scheme as introduced by Bachau and Theron [36], is offered by DYMORE, which alleviates this potential problem.

The input data for the FEMANA module is organised into three blocks. The first block defines the title line, the second block defines the initial conditions for the analysis with a restart option and the third block defines the time step control parameters. FEMANA can, therefore, analyse structures where the initial displacements and velocities at all nodes are zero or where the initial conditions have been determined by a previous analysis, thus providing the restart option as determined in block two. The convergence of the iterative process is monitored in block three, by computing an energy norm. When this norm becomes smaller than the requested convergence tolerance within the maximum selected number of iterations, the solution has converged. The maximum number of iteration steps is dictated by the nonlinear nature of the system and, in order

to control the size of the output file, a certain archival rate has to be specified [18]. The FEMANA output file serves as the input file for the PSTFEM module.

4.2.3 The PSTFEM Module

This module performs the post-processing of the finite element analysis. Displacements, velocities, accelerations, aerodynamic properties and internal variables can be printed according to the user's choice. A time history of user selected variables can also be printed and plotted.

The post-processor can provide two different types of output. The first option provides information on the complete configuration of all bodies. The displacements and rotations of all nodes of the body, as well as forces and velocities for all elements of the model, can be provided. The resultant output file is extremely large and, therefore, this option is generally only used for small, simple models with a small number of time steps.

The second option provides the user with the ability to select the time history for selected components of the model. These selected outputs, called output requests, relate to either system configuration components or components of quantities internal to elastic elements or constraints.

4.3 The Rooivalk Combat Support Helicopter Model

The Rooivalk Combat Support Helicopter is modelled by means of two major structures, the fuselage and the rotor. Both structures consist of a number of four-noded beam elements of varying cross-sections and lengths. Nineteen beams are used to describe the fuselage and 25 beams define the rotor. The cross-sectional properties in terms of the stiffness properties with respect to the shear centre, mass properties with respect to the local axis system and the coordinates in the local axis system are determined for each of these beams in order to make the model representative of the real helicopter. The main and tail landing gear oleo struts (shock absorbers) are modelled with rectilinear spring/damper sets, while the tires (both on the main and tail wheels) are modelled with rectilinear spring sets in all three cardinal directions of the global axis system. Revolute joints, connected by short, very stiff beams represent the flap, lead-lag and pitch hinges. A rectilinear damper provides lead-lag damping. A revolute joint allowing for the rotation of the main rotor connects the rotor and fuselage.

4.3.1 The Fuselage Model

The fuselage is represented by 19 very stiff, interconnecting beam elements and is considered to be a rigid body. The beams represent the physical fuselage structure while joints, springs and dampers represent the dynamic components of the structure. There are 69 nodes associated with the structure as can be seen in Appendix A. The model is fully three dimensional with six degrees of freedom, three in translation and three in rotation. The global axis system for the structure is defined in such a way that the x-axis is aligned with the longitudinal axis of the aircraft, indicating the positive direction towards the tail. The y-axis is aligned with the normal axis of the fuselage with its positive direction upward towards the rotor. The z-axis coincides with the aircraft's lateral axis with its positive direction to the left when the fuselage is viewed from the rear.

The main landing gear shock absorbers and tires are modelled separately. Rectilinear spring/damper elements, connected to the fuselage with ball joints, represent the main landing gear oleo struts and are represented by the zigzag lines between nodes 45 and 46 as well as 51 and 63 in Appendix A. The tire characteristics are represented by three springs in the cardinal directions of the global axis system connecting nodes 41 and 42, 41 and 43 as well as 41 and 44. The springs are constrained at nodes 42, 43 and 44, which represent the ground surface on which the tire is resting. The main landing gear wheel hub is located at node 41. Similarly, the other main wheel hub is located at node 59 and its tire characteristics are, once again, represented by the springs connecting node 59 with nodes 60, 61 and 62, which are also constrained.

The tail landing gear shock absorber and tires are modelled in the same manner as the main landing gear. A rectilinear spring/damper combination represents the tail landing gear oleo strut between nodes 24 and 27 and the springs between node 30 (location of the tail wheel hub) and nodes 31, 32 and 33 represent the tail wheel tire characteristics. These nodes indicate the contact point between the tire and the ground and are, therefore, also constrained.

The hinges in both the main and tail landing gear are modelled with revolute joint constraint elements at nodes 36 and 54 (main landing gear) as well as node 19 (tail landing gear). These joints allow freedom of rotation around the global z-axis. The total mass and inertia of the fuselage is located at the aircraft's centre of gravity located at node 66 and the shaft of the four-bladed rotor is attached to the fuselage at node 69.

4.3.2 The Rotor Model

The four-bladed rotor is modelled with 24 beam elements and is connected to the fuselage by a single beam element between nodes 69 and 75 as can be seen in Appendix B. This beam element represents the rotor shaft, about which the rotor spins and is inclined at an angle of 5 degrees towards the nose of the aircraft. The four blades are identical and are modelled with three four-noded beam elements each of which is 2.333 meters in length giving a total blade length of seven meters. The beam elements are situated between nodes 85 and 96, 106 and 117, 127 and 138, 148 and 159 respectively. In Appendix C the total rotor diameter is given as 15.58 meters, giving a rotor radius of 7.79 meters of which 7 meters comprises the blade itself. In the remaining 0.79 meters, three revolute joints interconnected by very stiff beams model the three hinges of the articulated rotor head. The revolute joints representing the flap hinges are situated at nodes 78 to 80, 99 to 101, 120 to 122 and 141 to 143 respectively. Nodes 81 to 83, 102 to 104, 123 to 125 and 144 to 146 represent the revolute joints for the lead-lag hinges whereas nodes 84 to 86, 105 to 107, 126 to 128 and 147 to 149 represent the revolute joints for the pitch bearings on each blade. Nodes 85, 106, 127 and 148 correspond to the zero blade reference points, which correspond to the position of the boltholes where the blades are attached to the rotor hub.

Each blade of the rotor is considered to be an elastic body consisting of three beam elements. The cross-sectional properties of each blade are entered directly into the PREFEM module from data derived from an Aerospatale document [37]. For each blade the centre of mass, the shear centre and the centroid of each cross-section is assumed to be co-located at the same position. The cross-bending stiffness and cross-shear stiffness of each section is taken to be zero and aerodynamic effects relating to the rotor are ignored. This is considered to be a reasonable assumption as the aerodynamic effects on ground resonance are negligible.

4.4 Rooivalk Data for the PREFEM Model

As described in paragraph 4.2.1, the PREFEM module consists of 21 blocks in which various parameters are defined. For the Rooivalk model the following parameters are defined and entered in their appropriate form:

4.4.1 Global Control Parameters for the Pre-Processor

Number of nodes in the model:	159
Number of triads:	63
Number of bodies:	2
Analysis type:	0 (Static Analysis) or 2 (Dynamic Analysis, Energy Decaying Scheme)
Number of time steps:	1 to 3000 (as required by different analyses)
Number of harmonic time functions:	1
Number of user defined time functions:	1
Number of prescribed loading cases:	0 (Static Analysis) or 1 (Dynamic Analysis)

Number of cross-sections:	14
Number of spring property sets:	13
Scaling factor for constraints:	10^5
Number of beam elements:	44
Number of rigid bodies:	1
Number of rectilinear spring/damper elements:	12
Number of prescribed displacements:	5
Number of revolute joints:	16
Round-off error:	10^{-14}

4.4.2 Global Nodal Co-ordinates, Triads and Boundary Conditions

4.4.2.1 Global Co-ordinates

The global co-ordinates of all 159 nodes are determined from technical drawings supplied by Denel Aviation [38]. Where the nodes do not correspond to defined points on the drawings, the co-ordinates are interpolated at regular intervals between two known stations. Other given station co-ordinates that coincide with a node of the model are entered directly into the PREFEM module. Nodal co-ordinates for the main and tail wheel configuration are calculated assuming that the aircraft is in the lower static line position (5600 kg basic weight). Tail wheel radius is 0.218 m while the main wheel radius is 0.3075 m.

The rotor shaft is modelled by a single beam of 1.32 m length consisting of 4 nodes and is inclined at 5° from the normal axis towards the nose of the aircraft. The rotor hub radius is 0.79 m with the flap hinge at 0.21 m, the lead-lag hinge at 0.27 m and the pitch change hinge at 0.79 m from the centre of the rotor. The four blades are each modelled with three four-noded beams giving a blade length of 7 m and a rotor radius of 7.79 m. The nodes of the blade are equally spaced at a distance of 0.77778 m from each other. The change in angle of the blade (blade twist) is described by defining a specific triad at each node of the blade and progressively reducing the angle of rotation of the triad around the x-axis from the blade root to the blade tip.

4.4.2.2 Triads

Sixty-three triads are defined for the entire model, 12 for the fuselage and 51 for the main rotor. The large difference in the number of triads between the two main bodies of the structure arises from the fact that the fuselage is considered to be a rigid body while the rotor is an elastic body.

Twelve triads, therefore, fully describe the orientation of the 19 beam elements of the fuselage and the three revolute joints representing the moveable main and tail landing gear struts. The triads of the beam elements are defined in such a way that the x-axis, of the local axis system, is aligned with the longitudinal axis of the beam (i.e. its length). The triads used in the revolute joints are orientated such that the rotation of the joint takes place around the z-axis of the triad. All triads are defined by a rotation matrix consisting of the three direction cosines of three orthogonal unit vectors, which, in most cases, can be determined directly from the technical drawings of the Rooivalk [38]. The orientation of the triads used for the main landing gear struts and shock absorber attachments are calculated by making use of Euler angles and then entered into the PREFEM module in the required format.

Fifty-one triads are required to fully describe the rotor model in terms of 25 beam elements and 13 revolute joints. The beam elements model the rotor shaft, the rotor hub and the four blades while the revolute joints model the rotor shaft rotation as well as the flap, lead-lag and pitch hinges of the rotor. Triads are also defined for each node of the rotor blade to simulate the blade twist, again making use of Euler angles.

4.4.2.3 Boundary Conditions

There are six degrees of freedom at each node: the three components of the displacement vector and the three components of the conformal rotation vector, all of which are measured in the global axis system. Boundary conditions can be applied to any of the degrees of freedom by either defining the degree of freedom as unconstrained, constrained or slaved. When a node is unconstrained, it is considered to be an unknown of the problem. Nodes that do not change their displacement or rotation are constrained (nodes 31 to 33, 42 to 44 and 60 to 62 in Appendix A, which represent the surface on which the helicopter is resting). If any degree of freedom of a node is constrained in such a way that it is identical to the corresponding degree of freedom at another node, that node is slaved to the other node (the second node of each revolte joint is slaved to the first node in terms of its displacement).

4.4.3 Blade Element Definition

In this block 44 beam elements are defined and linked to either the fuselage or the rotor by means of a body reference number (body 1: fuselage and body 2: main rotor). Each beam element is defined by four equally spaced nodes of which the first and second node represent the end points of the beam and the other two nodes are internal to the beam. An orientation triad is defined at each active node element in such a way that the cross-section of the beam is located in the plane defined by the y- and z-axis of the triad. One cross-section description is also referenced at each active node of the element.

4.4.4 Rigid Body Definition

The fuselage is defined as a rigid body with its reference point located at the fuselage centre of gravity (node 66 in Appendix A). A local co-ordinate system is defined to describe the rigid body with its origin at the reference point. The fuselage mass is calculated at 5054.2 kg. This is obtained by subtracting the blade mass of 465.8 kg (supplied by Denel Aviation [39]) and the rotor shaft/hub mass of 80 kg (estimated) from the total mass of the aircraft in the lower static line position of 5600 kg given on the Denel Aviation technical drawings [38].

4.4.5 Prescribed Displacement Definition

A time history of a specific displacement component is defined in this block. The displacement component is described by the first node assigned to the prescribed displacement and a specific degree of freedom. A second node is assigned the degree of freedom corresponding to the Lagrange multiplier used to enforce the prescribed displacement constraint. Therefore only the first degree of freedom of the second node is used and the last five degrees of freedom are constrained [18]. A prescribed displacement is defined at nodes 86 and 87, 107 and 108, 128 and 129 as well as 149 and 150 (Appendix B) by means of the absolute value of a constant time function, simulating the lead-lag motion of the blades. The torque of the main rotor head is also prescribed at nodes 71 and 72 by means of a user defined time function.

4.4.6 Revolte Joint Definition

Sixteen revolte joints are used to represent the 'hinge type' structures in the model, three for the fuselage and 13 for the main rotor. Revolte joints at nodes 19 to 21 facilitate the rotation of the tail landing gear strut around the global z-axis while the two revolte joints at nodes 36 to 38 and 54 to 56 allow for the rotation of the main landing gear struts, also around the global z-axis (Appendix A). The joint at node 69 to 71 allows for the rotation of the main rotor at its attachment to the fuselage. Nodes 78 to 80, 99 to 101, 120 to 122 and 141 to 143 represent the flap hinges, nodes 81 to 83, 102 to 104, 123 to 125 and 144 to 146 represent the lead-lag hinges and nodes 84 to 86, 105 to 107, 126 to 128 and 147 to 149 represent the pitch change mechanism at each blade of the four-bladed rotor (Appendix B).

The first two nodes define the revolute joint and the three rotational degrees of freedom at each node are affected by the joint. The third node is assigned the degrees of freedom corresponding to the Lagrange multipliers used to enforce the kinematic constraint at the joint and the relative rotation of the joint. Therefore only the first four degrees of freedom are used and the last two degrees of freedom are constrained [18].

Each revolute joint is also defined by a specific triad associated to the joint in such a way that the axis of rotation of the joint corresponds to the z-axis of the specific local triad. A property set for the torsional spring and viscous damper in the revolute joint can also be defined for each joint and this is applied to the four lead-lag hinges of the main rotor model.

4.4.7 Time Integration Control Parameters

In this block the initial time, final time and the time step size is selected as required by the analysis to be performed. If the iterative solution process fails to converge another attempt is made at half the time step size. This process is repeated for a user-defined number of times. Two time-stepping procedures are available, one of constant time step size and one of an adaptive time step size. If the adaptive time step procedure is selected, a desired local error during each time-stepping procedure and the maximum allowable error for each time step must be defined. The reference energy level and maximum number of time step rejects are also defined in this block.

4.4.8 Harmonic and User Defined Time Functions

4.4.8.1 Harmonic Time Functions

Harmonic time functions consist of the superposition of N harmonics. In each case, entries for the amplitude a_i , the period T_i and the phase θ_i for each harmonic are required. The harmonic time function is then given by:

$$f(t) = \sum_{i=1}^N h_i(t) = \sum_{i=1}^N a_i \sin 2\pi \left(\frac{t}{T_i} + \theta_i \right)$$

If the period $T_i = 0$, the corresponding harmonic is a constant such that $h_i(t) = a_i$ and the phase θ_i is not used. The harmonic time function for the lead-lag motion of the blade is given by $0.292587 \sin 2\pi (\text{TIME} / 0 + 0)$ giving a lead-lag angle of 16.76° .

4.4.8.2 User Defined Time Functions

User defined functions are piece-wise linear functions of time. Entries are required for a specific time and its associated function value. The user defined time function is then specified by N couples of values $[t_i, F_i]$. Linear variation in time is then assumed between each of these points.

One user defined time function describes the torque of the main rotor experienced at node 71 and 72 (Appendix B) and is defined as a prescribed rotation in the prescribed displacement block of the PREFEM module.

4.4.9 Dead Loading Cases Definition

A dead load is a load of which the direction is fixed in space and the magnitude is user defined. Both force and moment loads can act at any specified node. The first three load components correspond to the components of the force vector while the last three components correspond to the components of the moment vector. All loading components are measured in the global axis system. One dead loading case is applied to the rotor model at node 82, part of the lead-lag

hinge of the first rotor blade as a moment load disturbing the lead-lag hinge by one radian per second in the direction of rotation. This disturbance represents the external impulse that disturbs the lead-lag motion of the rotor blade, which may lead to ground resonance.

4.4.10 Gravitational Forces Definition

The components of the gravity vector are defined so that gravity acts in the negative y-direction of the global axis system.

4.4.11 Elastic Body Definition – Constant Rigid Body Angular Motion

A rigid body rotation is assigned to each body of the model and each body is allowed to rotate about a fixed point. A node about which the rotation takes place is identified and the three components of the constant angular velocity vector, in the global axis system, is specified. This rigid body rotation is only used when performing a static analysis. For the dynamic analysis this rigid body rotation is ignored. For the fuselage of the Rooivalk model (body 1), the angular velocity about node 75 (Appendix B) is zero while the rotor angular velocity is 19.63 radians per second in a clockwise direction when viewed from above.

4.4.12 Nonlinear Spring and/or Damper Definition and Properties

A total of 12 rectilinear spring/damper elements are defined for the fuselage of the Rooivalk model. These elements define the main and tail landing gear shock absorbers as well as the main and tail wheel tire characteristics. Each element is defined by two nodes between which the spring or damper operates, the body to which it is associated, the spring or damper property set that is to be used and the length of the element.

The same input format is used to define the properties of an elastic spring or viscous damper for either extensional or torsional behaviour. An elastic spring property set defines the nonlinear relationship between the elastic force F_{el} and the stretch s_{el} of the spring. This relationship is defined by a Chebyshev approximation of the form:

$$F_{el}(s_{el}) = \sum_{i=1}^{NCHEB} CHEB_i \cdot CHEBPOL_{i-1}(u_{CHEB})$$

where $CHEB_i$ are the coefficients of the Chebyshev polynomial [30]. $CHEBPOL_i$ and u_{CHEB} is the non-dimensional stretch defined as:

$$u_{CHEB} = \frac{2s_{el} - (XH + XL)}{(XH - XL)}$$

with XL and XH being the lower and upper bounds defining the range over which the approximation is valid.

A viscous damper property set defines the nonlinear relationship between the viscous force F_{vi} and the stretch rate \dot{s} of the damper. This relationship is defined by a Chebyshev approximation of the form:

$$F_{vi}(\dot{s}) = \sum_{i=1}^{NCHEB} CHEB_i \cdot CHEBPOL_{i-1}(v_{CHEB})$$

where the non-dimensional stretch rate v_{CHEB} is defined as:

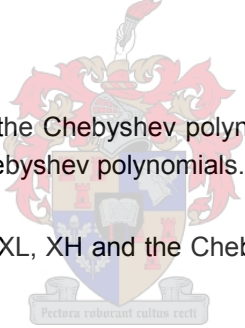
$$v_{\text{CHEB}} = \frac{2\dot{s} - (XH + XL)}{(XH - XL)}$$

with XL and XH being the lower and upper bounds defining the range over which the approximation is valid.

For a torsional elastic spring or damper the stretch and stretch rate s_{e1} and \dot{s} are replaced by the angular twist and twist rate while the elastic and viscous forces are replaced by the elastic and viscous moment respectively.

To enter the spring property sets in their required format, the following procedure is followed:

1. Extract data points from graphs of main landing gear shock absorber characteristics [41], main landing gear dynamic tire diagram [41], tail landing gear shock absorber characteristics [42] and tail landing gear dynamic tire diagram [42] and enter these data points into "Tablecurve" [43].
2. Use "Tablecurve" software to obtain a polynomial approximation of the extracted data points.
3. Determine XL and XH for the spring property set.
4. Use the definition of the non-dimensional stretch u_{CHEB} to express the x-polynomial approximation in terms of u_{CHEB} .
5. Determine the coefficients of the Chebyshev polynomial by a process of long division of the polynomial in u_{CHEB} by the Chebyshev polynomials.
6. Enter the values obtained for XL, XH and the Chebyshev polynomial coefficients into the PREFEM module.



The spring property sets for the main landing gear tires lateral and longitudinal stiffness characteristics are estimated by modifying values found for the "Advanced Chinook" Tandem Helicopter [44]. This is done by comparing the vertical stiffness of both tires (the Rooivalk vertical tire stiffness is approximately 50% of that of the Chinook tire) and then reducing the Chinook lateral and longitudinal stiffness by 50% to approximate the Rooivalk main wheel tire stiffness, both laterally and longitudinally. As the main wheel of the Rooivalk is approximately 1.5 times the diameter of the tail wheel, the tail wheel tire lateral and longitudinal stiffness is reduced by a third of those calculated for the main wheel tires. The lead-lag spring stiffness is supplied by Denel Aviation [39].

The damping properties of the main and tail landing gear shock absorbers are calculated from literature [45]. The following formula is used:

$$\frac{F_d}{A} = p = \frac{\gamma}{2g} F_d w^2 \frac{A^2}{(\sum f/a)^2} \Rightarrow F_d = \frac{1}{2} \rho w^2 \frac{A^3}{(\sum f/a)^2}$$

where F_d is the damping force of the shock absorber, ρ is the density of the fluid in the damper, w is the cylinder velocity, A is the cross-sectional area of the piston and f/a is the effective orifice for the flow. Using data provided by Denel Aviation [41,42] the following function for the damping in the main wheel shock absorbers is found:

$$F_{dMLG} = 1.42413 * 10^{12} w^2$$

Similarly the damping force in the tail landing gear shock absorber is given by:

$$F_{dTLG} = 3.42328 * 10^{12} w^2$$

These functions are converted into Chebyshev polynomials and entered into the PREFEM module.

4.4.13 Cross-section Definition

The physical properties of the beam elements that represent the model are defined in this block and the equivalent stiffness and mass properties of a specific cross-section are defined. The axial stiffness, the two bending and the two shear stiffnesses in the lead-lag and flapping directions, the torsional stiffness, the mass distribution and the mass moments of inertia about the three axes of the local axis system are entered directly into the PREFEM module. The centre of mass, the shear centre and the centroid location are declared as well.

Fourteen cross-sections are thus defined for the rigid beams of the fuselage, the rotor hub, the three hinges of each blade and the rotor blade itself. The rigid beams of the fuselage are assumed to be identical and, therefore, only one cross-section is required to define the physical beam properties. The rotor hub beams are defined by three cross-sections while the rotor blade contains 7 cross-sections. The axial stiffness and bending stiffnesses at different stations from the rotor hub to the blade tip are supplied by Denel Aviation [37].

As no torsional and shear stiffness information is included in this document, these quantities are calculated. The angle of twist of a rectangular bar of length L_B can be expressed as:

$$\phi = \frac{T_o L_B}{GJ}$$

with $J = k_1 a h^3$, where ϕ is the angle of twist, T_o is the torque applied to the bar, L_B is the length, G is the shear modulus, k_1 is a dimensionless constant and a and h are the cross-

sectional dimensions of the bar such that $\frac{a}{h} \geq 1$ [46]. The factor $GJ = G k_1 a h^3$ is the torsional rigidity or stiffness of the bar/beam, which is now calculated from the Denel Aviation data [37] by assuming a cross-section of $a = 0.6$ m and $h = 0.1$ m, taking $k_1 = 0.299$ (table 4.3, p 271, [46])

and calculating G with $G = \frac{E}{2(1+\nu)}$ ($\nu = 0.3$ and equation 2.24, p 56, [46]).

The shear stiffnesses are calculated using Timoshenko beam theory, which is an improvement on the Bernoulli-Euler beam theory in that it also considers out-of-plane rotations of the cross-sections. Timoshenko introduced a factor on the transverse shearing stiffness terms, which is $\frac{5}{6}$

in the case of a rectangular cross-section so that the shearing stiffness is equal to $\frac{5}{6}GA$.

Assuming the same cross-sectional area as for the torsional stiffness, the shearing stiffness in the flapping and lead-lag directions (assumed equal) is now calculated from the data supplied by Denel Aviation [37].

The mass distribution and mass moment of inertia information is interpolated from tables provided in the same document and is then entered in the appropriate fields of the PREFEM module. The centre of gravity location, shear centre location as well as the centroid location are assumed to be the same and the cross-shear and cross-bending stiffness are zero. Although possible, the aerodynamic effects of the rotor are not taken into account as their contribution to the ground resonance phenomenon is assumed to be negligible.

With all the required data supplied to the pre-processor, the FEMANA module of the DYMORE program can now perform the finite element analysis of the system to be investigated. Both static and dynamic analyses are performed.

4.5 Static Analyses of the Rooivalk Model

4.5.1 The Rotor

In the rotor model of the Rooivalk each blade is assumed to be identical in terms of length, twist and cross-sectional properties. In order to verify the correct construction of the model, a static analysis is done on each blade. If each of the blades is identical then this analysis must yield equal eigenvalues for each blade under the same set of conditions. Each blade is analysed independently in that four analyses are done, one for each blade. In each case the fuselage and three rotor blades are fully constrained and the single blade is rotated by means of a rigid body rotation at an arbitrarily chosen angular velocity of 275 rpm (28.8 rads/sec) in zero gravity conditions. In order to prevent any flapping motion, the flap hinges of the rotor model are constrained with very stiff springs. A prescribed loading case and a prescribed displacement that act on the rotor are not used in the static analyses but are included in the later dynamic analyses.

Each single blade system has 124 degrees of freedom of which the first nine eigenvalues are determined. The analysis shows that the real part of all these eigenvalues are extremely small (in the order of 10^{-7} and 10^{-8}), which means that the variance in the above real parts is negligible. As the imaginary parts of the calculated eigenvalues are identical it can be deduced that the blades that are modelled for the rotor are, in fact, identical.

In a final year project study done at the Department of Mechanical Engineering of the Stellenbosch University [49], the same rotor blade model was used to demonstrate the effects of utilizing the CROSEC module of DYMORE. In this study, a number of characteristic properties of the blade beam cross-sections are compared to cross-sectional properties supplied by Aerospatiale [37]. It is shown that, in terms of mass distribution, tension stiffness, flap bending stiffness and lead-lag bending stiffness, the Rooivalk blade model coincides well with the Aerospatiale information and the blade model, therefore, sufficiently matches the real rotor blade. It is thus deemed suitable for further use.

4.5.2 The Fuselage

A static analysis is done on the fuselage to determine its mode shapes. In this analysis only the fuselage is modelled with 19 beam elements consisting of a total of 69 nodes. The beam elements vary only in length and orientation but are identical in terms of their cross-sectional properties. Three revolute joints represent the moveable main and tail landing gear strut attachments and 8 rectilinear spring/damper sets are used to describe the tail and main landing gear shock absorbers as well as the tires.

Five eigenvalues are determined for the system from which the first five modes of vibration are plotted. The first mode of vibration occurs at 8.070 rad/sec and is predominantly a rolling mode as can be seen in figure 4.5.2.1.

1ST MODE OF VIBRATION FOR FREQUENCY : 8.07001 RAD/S (FRONT VIEW)

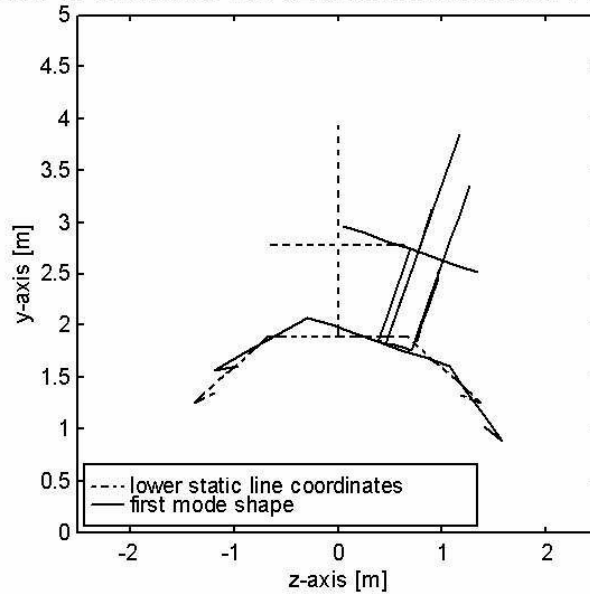


Figure 4.5.2.1 First fuselage mode of vibration

The second mode of vibration occurs at 8.228 rad/sec and is purely a pitching mode as can be seen in figure 4.5.2.2.

2ND MODE OF VIBRATION FOR FREQUENCY : 8.22814 RAD/S (FRONT VIEW)

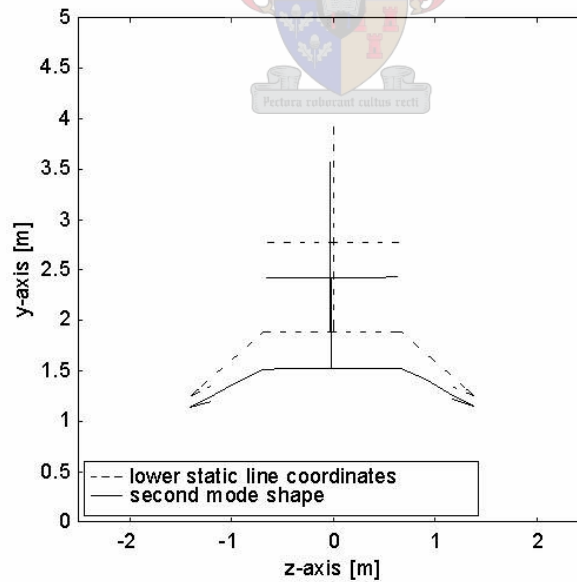


Figure 4.5.2.2 Second fuselage mode of vibration

The third vibration mode, shown in figure 4.5.2.3, is predominantly a yawing mode and occurs at 12.481 rad/sec. A small amount of pitch can also be seen.

3RD MODE OF VIBRATION FOR FREQUENCY : 12.4805 RAD/S (FRONT VIEW)

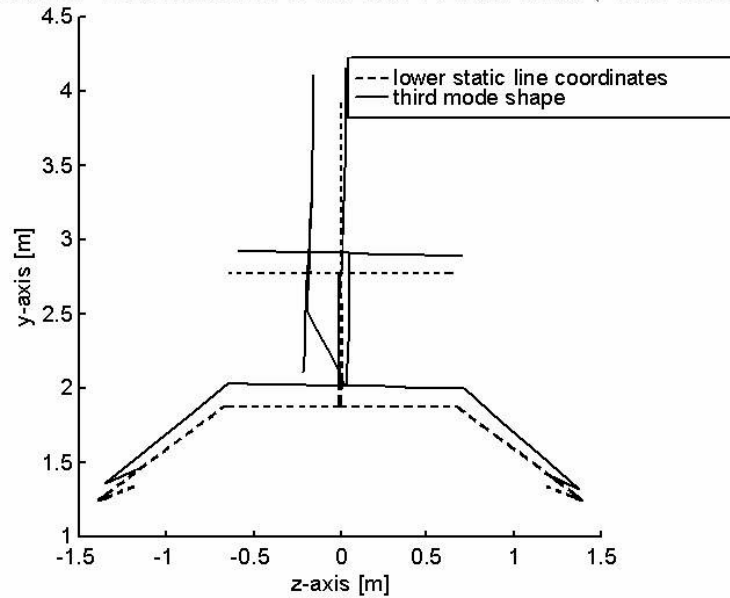


Figure 4.5.2.3 Third fuselage mode of vibration

The fourth vibration mode occurs at 55.308 rad/sec and is predominantly a rolling mode with a small amount of pitch as shown in figure 4.5.2.4.

4TH MODE OF VIBRATION FOR FREQUENCY : 55.3080 RAD/S (FRONT VIEW)

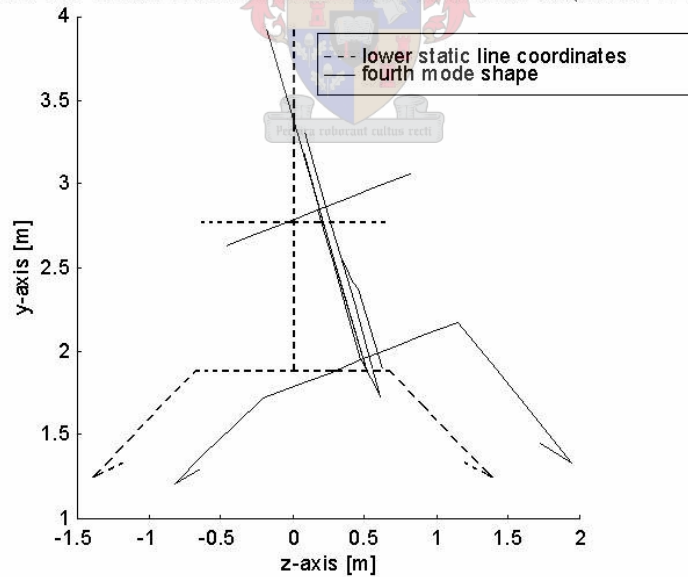


Figure 4.5.2.4 Fourth fuselage mode of vibration

The last mode that is investigated occurs at 79.021 rad/sec and is a combined mode with both pitch and yaw as shown in figure 4.5.2.5.

5TH MODE OF VIBRATION FOR FREQUENCY : 79.0214 RAD/S (REAR VIEW)

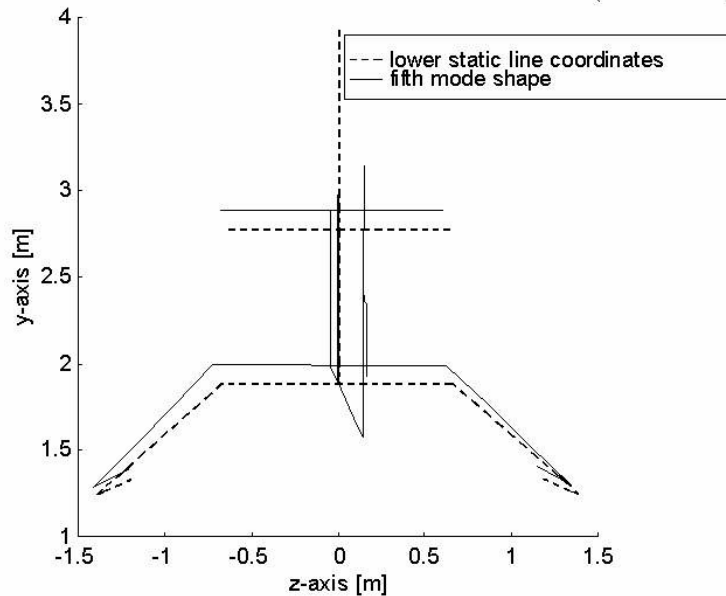


Figure 4.5.2.5 Fifth fuselage mode of vibration

The first two vibration modes in roll and pitch are the two uncoupled fuselage modes that will predominantly influence the ground resonance phenomenon as it is these modes that represent the uncoupled roots for the support modes, which are represented by the horizontal lines at $\omega = \omega_x$ and $\omega = \omega_y$ and ω_c as shown in figure 3.3.1 and figure 3.3.2.

4.5.3 Comparison of Uncoupled Fuselage and Blade Frequencies

To determine possible regions of instability, the frequencies of the first two vibration modes of the fuselage must be compared to the uncoupled lag frequency of the rotor blade. Information obtained from Denel Aviation [47] shows that the blade frequencies can be calculated by means of the following equation:

$$f = \sqrt{\frac{\Omega^2 h_o M_a m_b}{I} + \frac{K}{I}}$$

where f is the rotor blade lag frequency

Ω is the constant rotor angular velocity in rad/s

h_o is the rotor blade lag hinge offset

M_a is the mass moment arm to CG from lag hinge of a rotor blade

m_b is the blade mass

I is the rotor blade lag inertia about the drag hinge

K is the rotor blade lag hinge stiffness

in rotating co-ordinates.

In fixed co-ordinates the frequency splits into lead and lag frequencies:

$$f_1 = \Omega - f$$

$$f_2 = \Omega + f$$

of which f_1 can be unstable.

The following data is also contained in the Denel Aviation document [47]:

$$h_o = 0.27 \text{ m}$$

$$M_a = 2.463 \text{ m}$$

$$m_b = 116.4 \text{ kg}$$

$$I = 1334 \text{ kg} \cdot \text{m}^2$$

$$K = 153821 \text{ Nm/rad}$$

The uncoupled blade frequencies are now determined for rotor speeds varying from 0 rad/sec to 28.8 rad/sec (275 rpm) in increments of 1.39 rad/sec and then plotted together with the first two uncoupled fuselage frequencies as shown in figure 4.5.3.1.

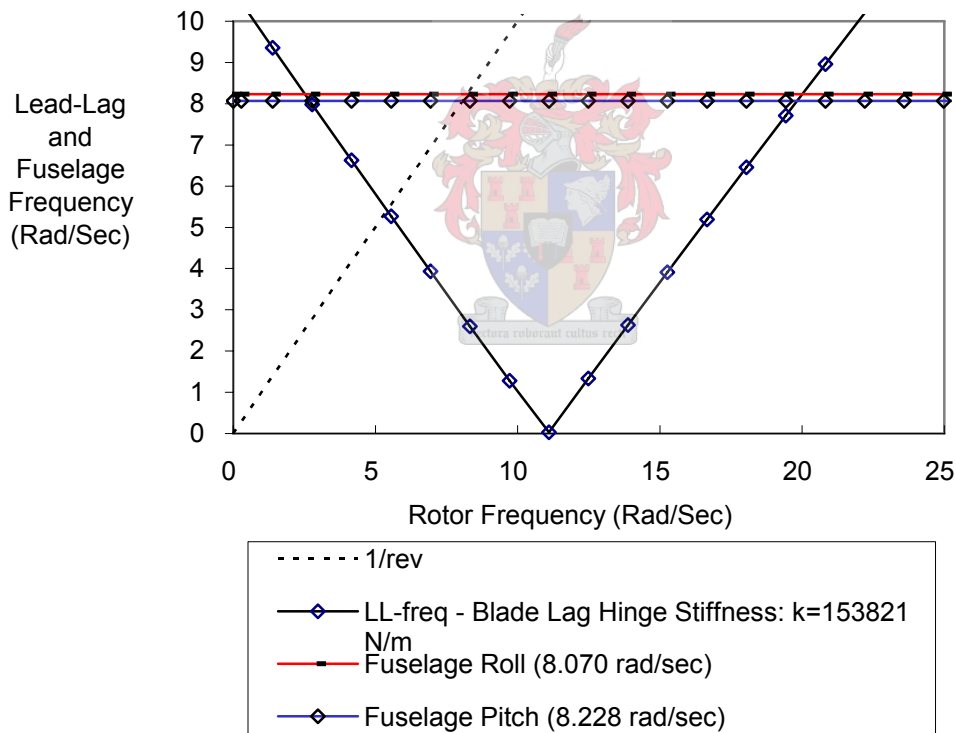


Figure 4.5.3.1 Comparison of uncoupled fuselage and blade frequencies

Figure 4.5.3.1 shows that the lag frequency and the fuselage frequencies intersect twice, once at approximately 3 rad/sec and again at 19.63 rad/sec. It is at the 19.63 rad/sec frequency where a possible instability / ground resonance may occur. The intersection at the 3 rad/sec will not cause an unstable situation [35 p. 382]. The reason for this is that, in general, resonances at below 40% normal rotor speed are acceptable as the rotor has little energy at these speeds and it is possible to run up the rotor through very low frequency resonance without a large amplitude motion building up [32 p. 668].

In figure 4.5.3.1 the rotor and support structure are uncoupled. When both systems are coupled, the natural frequencies of the complete system may have slightly different values. This is because the rotor influences the fuselage and visa versa. To determine the exact extent to which both structures influence each other a dynamic response analysis of the coupled system i.e. the complete helicopter model is required.

4.6 Dynamic Analyses of the Rooivalk Model

To perform any dynamic analysis of the helicopter model in DYMORE, three steps are required. In the first step, the fuselage is allowed to settle on its springs under the influence of gravity. A quasi-static analysis is done on the fuselage by constraining the revolte joint connecting the rotor to the fuselage (nodes 70, 71 and 72 in Appendix B) and applying the gravity vector to the fuselage. As the blade stops are not modelled on the rotor blades, the flapping hinges (nodes 79 and 80, 100 and 101, 121 and 122 as well as nodes 142 and 143 in Appendix B) are also constrained to prevent the blades from dropping onto the ground. The nodes of the lead-lag hinges and the pitch change mechanism are also constrained during this step and the rigid body rotation of the rotor is removed. In the second step, the fuselage nodes are constrained in the equilibrium position obtained in the first step. The rotor shaft attachment nodes and the hinge nodes on each blade are now unconstrained and the rotor is spun up to the specific speed at which the dynamic response of the helicopter model is to be investigated. This is done by a second quasi-static analysis based on the output of the first analysis of the first step. The third step is based on the output of the second static analysis and is the actual dynamic ground resonance analysis. All the nodes of the fuselage and rotor are now unconstrained and the rotor is spinning at 19.63 rad/sec (187.45 rpm). At this speed there may be a possibility of ground resonance as determined from figure 4.5.3.1. The output of the dynamic analysis consists of the time histories of a specified number of degrees of freedom of certain user-specified nodes. Various analyses are done in which the damping characteristics of the shock absorber, the tires and the lead-lag hinges are varied to determine their effect in terms of the ground resonance phenomenon.

4.6.1 Lower Static Line Analysis

In this dynamic analysis, the energy-decaying scheme of DYMORE is used with 3000 time steps. The helicopter is in the lower static line position (aircraft weight of 5600 kg) with the rotor spinning at 19.63 rad/sec. The entire system has 1590 degrees of freedom. The lead-lag hinge of one of the rotor blades is disturbed by applying a moment to the hinge, which results in the hinge being disturbed by 1 rad/sec in the direction of rotation. All springs and dampers in the tires, shock absorbers and lead-lag hinges are functioning at their specified operational values. As the Vibration Isolation System (VIS) that is implemented in the actual aircraft is not modelled in this simulation, this constitutes a single point failure in that the vibrations from the rotor are not damped but are transferred directly to the fuselage. To determine the effect of this single point failure, the time histories of the motion of the rotor attachment point, node 69 in Appendix B, in the global x, y and z-directions and the rotational motion of the lead-lag hinge on the first blade of the rotor (node 82 in Appendix B) are investigated.

The motion of the rotor shaft attachment point is well damped in the longitudinal and vertical directions with the motion in the x-direction not exceeding 1.14 cm forward of the equilibrium position of the aircraft. This can be attributed to the fact that the landing gear tires are constrained from moving in this direction by the springs representing the longitudinal tire stiffness. The y-direction motion is more heavily damped than the x-direction motion and does not exceed a maximum value of 3.45 cm vertically upwards. The springs and dampers of the landing gear shock absorbers combining with the vertical tire stiffness and tire damping cause the larger damping. The lateral motion in the positive z-direction shows the least amount of damping and this can be explained by the fact that the lateral motion is caused by the fuselage rocking on its

undercarriage. During this motion, damping is supplied by the shock absorbers and tires on one side of the aircraft under compression. Although this motion is poorly damped, its amplitude is small (less than 4 mm) and can, therefore be considered to be negligible.

The translational motion of the lead-lag hinge shows similar characteristics as those of the rotor shaft attachment point in that the longitudinal and vertical motion is well damped while the lateral motion shows less damping. This motion is also negligible, as, in all three cases the motion is less than 1 mm. The rotation of the lead-lag hinge is also well damped and does not exceed 0.008 rad or 0.46 degrees.

The single point failure of the Vibration Isolation System under the prescribed operational conditions (aircraft weight of 5600 kg and 187 rpm rotor speed) results in no indication of the ground resonance phenomenon.

4.6.2 Analysis with one Lead-Lag Damper inoperative

In this second dynamic analysis, the damping supplied by the main and tail landing gear shock absorbers and tires is retained while the damper in one of the lead-lag hinges of the rotor (node 123, 124 and 125 in Appendix B) is removed. This constitutes a dual point failure in that both the Vibration Isolation System and one lead-lag damper have failed. The analysis is again done using the energy-decaying scheme of DYMORE with 3000 time steps. The aircraft weight and rotor speed remains at 5600 kg and 187 rpm respectively and the lead-lag hinge, at node 82 in Appendix B, is again disturbed by 1 rad/sec in the direction of rotation. The time histories of the rotor shaft attachment point and the lead-lag hinge of the first rotor blade are again investigated.

The translational motion of the rotor shaft attachment point is identical to the motion of the first analysis. This is to be expected as the fuselage damping characteristics have not changed and, as such, the motion must remain the same.

The longitudinal translation of the lead-lag hinge on the first rotor blade is also nearly identical to the motion of the first analysis. The only difference is that in the first analysis, the motion is in the positive x-direction while in the second analysis the motion is in the negative x-direction. This is, most probably, caused by the lack of damping in the lead-lag hinge of the opposing rotor blade. The amplitude and damping characteristics remain the same.

The vertical motion of the first lead-lag hinge perfectly matches the motion seen in the first analysis in terms of direction, amplitude and damping as this motion is predominantly influenced by the vertical damping characteristics of the fuselage, which have not changed.

Although the z-direction translation of the first lead-lag hinge is similar to that of the first analysis, the initial amplitude of the motion has decreased due to the lack of lead-lag damping on the opposing rotor blade. The damping on the lead-lag hinge of the first blade has not changed and therefore the damping of the motion coincides with what was seen in the first analysis. Due to this, the rotation of the lead-lag hinge is also identical to the rotation of the first analysis.

The translation of the rotor shaft attachment point is identical to that of the first analysis and the first lead-lag hinge translation and rotation remains of the same order of magnitude. This motion can, therefore, again be considered as negligible.

The dual point failure of the Vibration Isolation System and one lead-lag damper under the prescribed operational conditions (aircraft weight 5600 kg and 187 rpm rotor speed) also results in no indication of the ground resonance phenomenon.

4.6.3 Analysis with no vertical Tire Damping

In this third analysis, the vertical damping provided by the main and tail landing gear tires is removed while the lead-lag, main landing gear and tail landing gear dampers are fully operational. This constitutes a multiple point failure in that the Vibration Isolation System and the damping in all three tires is lost. In this scenario it is, therefore, assumed that all three tires have become deflated. The number of time steps, analysis method, aircraft weight, rotor speed and lead-lag hinge disturbance are kept the same as in the first two analyses. The time histories of the motion of the rotor shaft attachment point and the lead-lag hinge of the first rotor blade are, once again, investigated. The result for the z-direction translation of the rotor shaft attachment point is shown in figure 4.6.3.1.

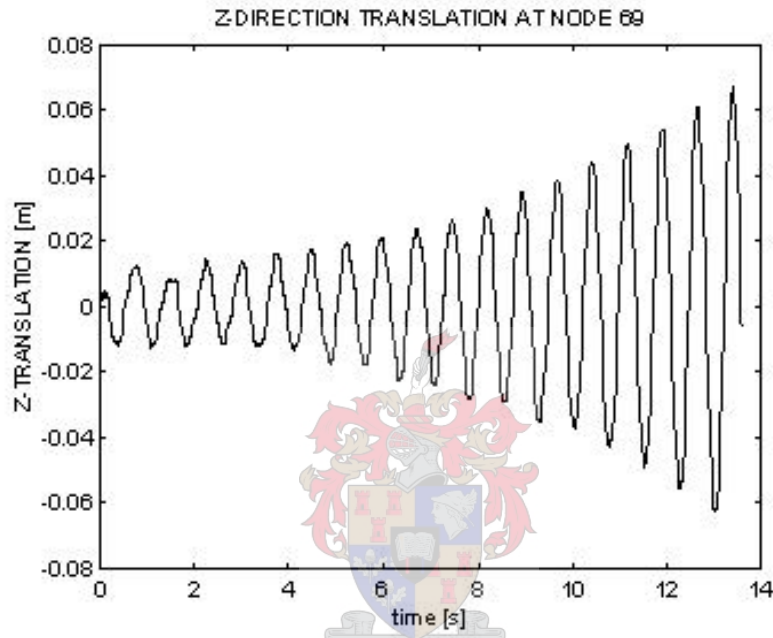


Figure 4.6.3.1 Translation of the rotor shaft attachment point (no Vibration Isolation System and no tire damping)

Removing the damping from all three landing gear tires changes the damping characteristics of the fuselage and, therefore, influences the translational motion of the rotor shaft attachment point. The initial amplitude of the motion in the x-direction is smaller than the amplitude seen in the first two analyses (between 7 and 15.5 mm in this analysis compared to between 9.8 and 11.4 mm in the first two analyses). This motion is, however, no longer highly damped. Damping is only provided by the landing gear shock absorbers, which causes only a slight reduction in the amplitude of the x-direction translation in the measured 14-second period. In the first two analyses, the amplitude decreased to less than 0.2 mm while there is still a 7 mm displacement in this analysis. The magnitude of the displacement is, however, still very small and can be considered to be negligible.

The initial amplitude of the y-translation of the rotor shaft attachment point is in the same order of magnitude as in the first two analyses (approximately 3 mm) but also shows less damping. As only the landing gear shock absorbers are providing the damping in this analysis, the amplitude of the motion is approximately 1 mm while it was practically zero in the first two analyses. The magnitude of this motion is, however, negligibly small.

The z-direction translation of the rotor shaft attachment point shown in figure 4.6.3.1 shows an increase in amplitude within 14 seconds, indicating an unstable situation. Removing the tire damping, therefore, gives rise to ground resonance instability at the given operational conditions.

As can be expected, the increasing rolling motion of the helicopter is associated with an increase in amplitude of the lead-lag motion of the rotor blades as indicated by the rotation of the lead-lag hinge of the first rotor blade shown in figure 4.6.3.2.

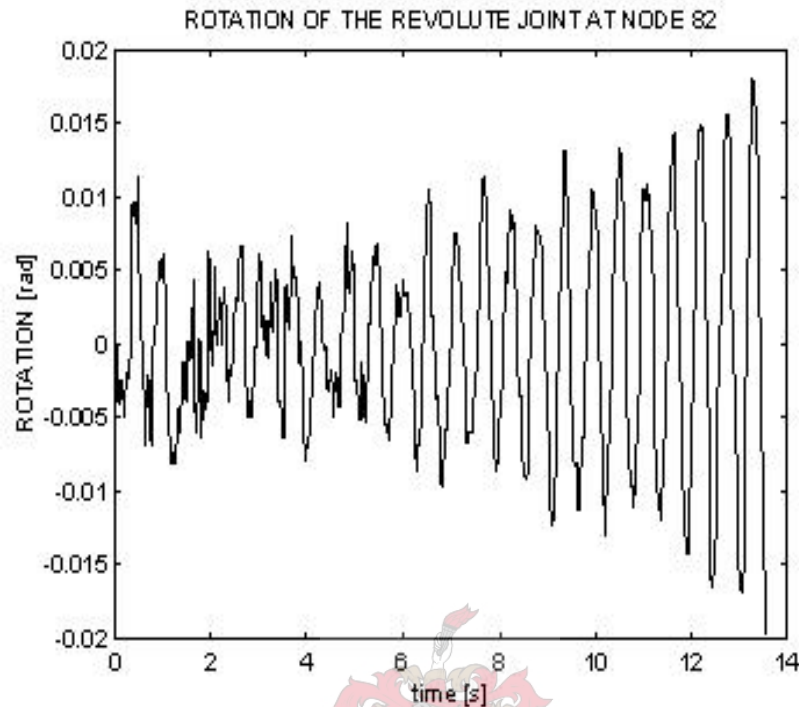


Figure 4.6.3.2 Rotation of the lead-lag hinge on the first rotor blade (no Vibration Isolation System and no tire damping)

The x- and y-translation of the lead-lag hinge on the first blade of the rotor again follows the motion of the rotor shaft attachment point in that, although its amplitude is smaller than in the first two analyses, it also shows less damping. The motion in the x-direction is again a lagging motion as was the case in the first analysis where all lead-lag dampers were also operational. The magnitude of both x- and y-translations is in the order of millimetres and can be regarded as negligible.

The multiple point failure of the Vibration Isolation System and all three tires, under the prescribed operational conditions (aircraft weight 5600 kg and 187 rpm rotor speed), indicates the onset of the ground resonance phenomenon.

4.6.4 Analysis with no vertical Tire Damping and no Shock Absorber Damping

The fourth analysis builds on the results of the third analysis in that all functional and operational conditions are kept the same but the shock absorber damping in the main and tail landing gear is also removed. This, again, represents a multiple point failure in that the Vibration Isolation System is inoperative, all three tires are deflated and all three shock absorbers are providing no damping. The time history of the motion of the rotor shaft attachment point in the z-direction is shown in figure 4.6.4.1.

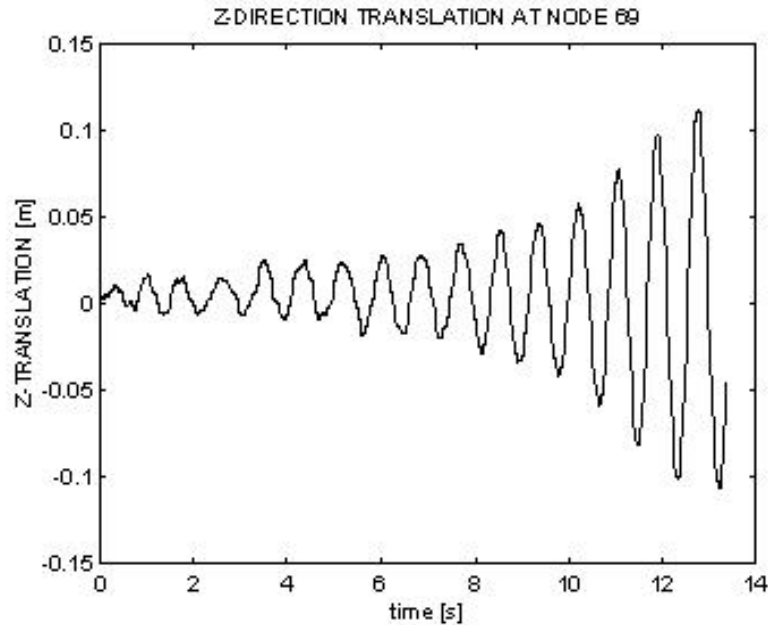


Figure 4.6.4.1 Translation of the rotor shaft attachment point (no Vibration Isolation System, no tire damping and no shock absorber damping)

As expected, the decrease in damping affects the translational motion of the rotor shaft attachment point in all three directions. The change in the initial x-direction displacement has increased from approximately 8 mm to approximately 6 cm. The motion also shows less damping, as is expected. Although there is a significant increase in the displacement and a decrease in damping, the magnitude of the motion is still relatively small and does not contribute to the ground resonance phenomenon.

The y-direction translation of the rotor shaft attachment point is affected in a similar fashion to that of the x-direction motion in that its magnitude has increased from a maximum displacement of 5 cm to 9 cm. The damping of the motion is also decreased, as expected. Again, the magnitude of the motion is still relatively small and shows no sign of instability.

The z-direction translation of the rotor shaft attachment point shows a significant instability in that the amplitude of the motion rapidly increases from zero to 12 cm within 14 seconds as shown in figure 4.6.4.1. This ground resonance instability is also reflected in the increasing rotation of the lead-lag hinge shown in figure 4.6.4.2.

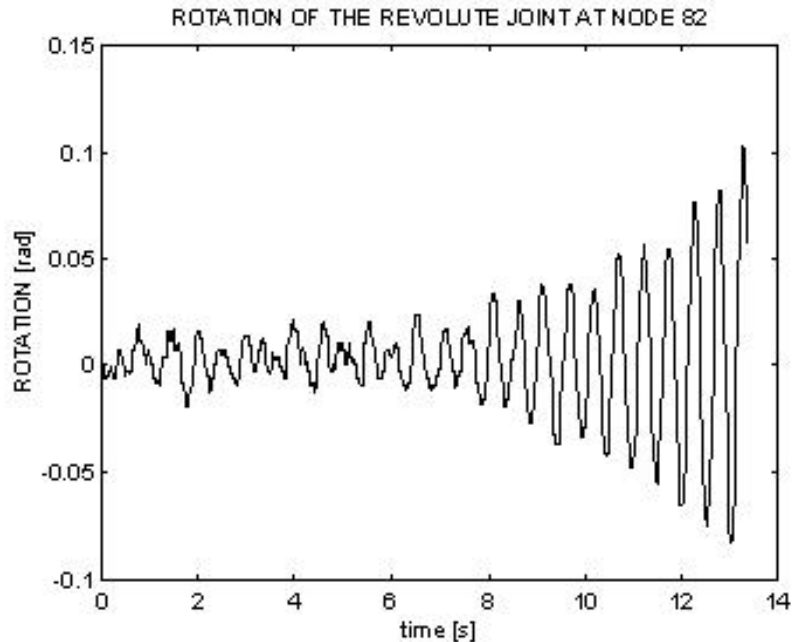


Figure 4.6.4.2 Rotation of the lead-lag hinge on the first rotor blade (no Vibration Isolation System, no tire damping and no shock absorber damping)

The scenario in which the fuselage provides no damping and only the lead-lag dampers of the rotor are operational, represents a multiple point failure, which leads to ground resonance instability. Under these operating conditions (aircraft weight 5600 kg and 187 rpm rotor speed) in which seven failures (Vibration Isolation System inoperative, three tires deflated and three shock absorbers providing no damping) are simulated, the first rolling mode frequency of the fuselage coincides with the lag frequency of the helicopter rotor blades and the coupling of these frequencies results in the helicopter becoming unstable.

4.7 Summary of DYMORE Analyses

As shown in paragraphs 4.5 and 4.6, the DYMORE software package is fully capable of analysing the ground resonance phenomenon on a conventionally articulated main rotor helicopter such as the Rooivalk. Both static and dynamic analyses are done on various components of the helicopter model to eventually define operational conditions in which ground resonance occurs. Static analyses are done to verify that the main rotor blades are identically modelled and to determine the fuselage uncoupled modes of vibration. Linking the first two fuselage modes to the blade lag frequency, results in the baseline operational conditions for the dynamic ground resonance analysis. The conditions are determined to be that the aircraft is operating at 5600 kg and the rotor is spinning at 187 rpm. In the subsequent dynamic analyses, various failure cases are evaluated, starting with a single point failure of the Vibration Isolation System. No indication of ground resonance is found. In the second dynamic analysis, a dual point failure of the Vibration Isolation System and a lead-lag damper is investigated. Again no indication of ground resonance is found. Two multiple point failures are then investigated in which ground resonance becomes evident. In these two cases, the main rotor is spinning at 187 rpm, which does not coincide with the worse case scenario predicted by Denel Aviation [47] of 275 rpm. As the rotor model is assumed to be accurate according to the Stellenbosch study [49], the only explanation for this discrepancy would be the fuselage model. In order to model the fuselage more accurately and reduce computational time, the Rooivalk model is re-designed in a new software package called MSC ADAMS.

5. Numerical Analysis with Interactive Motion Simulation Software: MSC ADAMS

5.1 General Description of the MSC ADAMS Software

MSC ADAMS (Automatic Dynamic Analysis of Mechanical Systems) Version 2005.0.0, Copyright 2004, MSC Software Corporation, Santa Ana, CA, U.S.A. is a family of interactive motion simulation software developed to analyze the complex behavior of mechanical assemblies. It allows for the testing of virtual prototypes and the optimization of designs for performance, safety and comfort without having to build and test numerous physical prototypes. The core package allows the user to import geometry from most CAD systems or to build a solid model of the mechanical system from scratch. A full library of joints and constraints is available for creating articulated mechanisms. Once the virtual prototype is complete, MSC ADAMS checks the model and then runs simultaneous equations for kinematic, static, quasi-static and dynamic simulations. Results can be viewed as graphs, data plots, reports or animations, which can be exported to other programs. The core MSC ADAMS package is supplemented by a wide range of extension modules such as ADAMS/FLEX, which can be used to evaluate flexible control surfaces i.e. the ailerons, the rudder and the elevator on a fixed-wing aircraft. Other modules are tailored for the automotive, aerospace and rail industries and include templates for building simulation models with various pre-built assemblies and sub-assemblies that can be incorporated into specific models. It is also possible to create user-defined assemblies and sub-assemblies for models that the program does not cater for.

The MSC ADAMS portfolio of software products is broadly classified in terms of four main groups, which are the core products, the extension products, the industry-specific products and the CAD interface products. The core products, which are ADAMS/VIEW, ADAMS/SOLVER and ADAMS/POST-PROCESSOR form the basics for all of the other MSC ADAMS products and provide a general-purpose modelling environment, a high-powered solver and a post-processing environment. The extension products extend the modelling capabilities offered by the core products by including descriptions for part flexibility (ADAMS/FLEX) or by allowing analyses for vibration (ADAMS/VIBRATION), amongst others. Industry-specific products are tailored to assist engineers in building and testing automotive, aerospace or rail designs by providing both standard and customized templates and test suites, which are common within each industry. There are nine industry-specific products, one of which is ADAMS/AIRCRAFT.

5.2 ADAMS/AIRCRAFT

This software package allows the user to build a complete, parameterized model of a new aircraft by defining its landing gear layout, wheel arrangement and other vital characteristics in the ADAMS/AIRCRAFT landing gear module. The module templates provided by the software are based on fixed-wing aircraft and it is, therefore, necessary to create new design templates for a helicopter airframe configuration.

5.2.1 Rooivalk Fuselage Model

5.2.1.1 Tail Landing Gear Single-Post Suspension Template

To create a customized template in ADAMS/AIRCRAFT, a topology consisting of hard points, parts, attachments and parameters that define subsystems is first created for the template. Hard points are elements that define all key locations in the model. They are the most elementary building blocks that are used to parameterize locations and orientations for higher-level entities. Hard point locations define most parts as well as attachments and are only defined by their co-ordinate locations and do not have orientations. Once the hard points have been defined, two types of parts are created, based on these locations. General parts, such as pistons, are rigid

parts that are defined by their location, orientation, mass, inertia and centre of gravity. Geometry can, also, be added to these parts. ADAMS/AIRCRAFT uses either geometry-based or user entered information to determine the mass properties for general parts. Mount parts are mass-less parts that attach to other parts. Attachments, such as joints, and parameters that tell ADAMS/AIRCRAFT how the parts react in relation to each other, complete the template.

For the Rooivalk model, rear landing gear shock absorber template, the major role of the template is classified as suspension. The upper and lower cylinder of the shock absorber are created by using five hard points, two defining the top and bottom of the upper cylinder, two defining the top and bottom of the lower cylinder and one that defines the spring/damper attachment point. The upper- and lower cylinder are created as geometry-based general parts, constructed of steel. Two sub-frames are defined at each end of the shock absorber. These sub-frames are intermediate parts, which ultimately connect the shock absorber to the fuselage in such a way that only two connections to the aircraft subsystem are required. A single oleo element containing a spring and a damper is then created, based on the spring and damper characteristics supplied by Denel Aviation [42]. The spring and damper are defined by property files in terms of force-displacement and force-velocity characteristics in the form of lookup-tables, which can be modified as required. Both components are attached between the spring/damper attachment hard point and the top of the lower cylinder and a translational joint is added between the upper and lower cylinder. Two mount parts and fixed links are created on the upper and lower sub-frame to eventually attach to the fuselage. For the assembly process to be successful, input communicators are added to the mounts. Communicators are ADAMS/AIRCRAFT elements that allow the tail landing gear shock absorber subsystem to exchange information with the fuselage subsystem in terms of topological data, parameter variables and location. The corresponding output communicators, of the same name, on the fuselage, supply this information. The template is then saved as a tail landing gear subsystem as shown in Appendix D.

5.2.1.2 Main Landing Gear Trailing Arm Suspension Template

For the Rooivalk main landing gear template, the major role of the template is again chosen as suspension, as was done for the tail landing gear shock absorber. The main suspension parts are the main strut, the trailer arm, the upper and lower shock cylinder with the spring and damper, various joints, two sub-frames and output communicators.

5.2.1.2.1 Main Landing Gear Main Strut

The main strut is defined by means of four hard points, one at the bottom of the strut and three at the top of the strut. One of the three top hard points is located at the centre point of the strut while the other two define points that are located just inboard and outboard of the centre hard point. These two points are used to define a construction frame (local co-ordinate system) of which the z-axis lies on the line connecting the two points. This axis later becomes the axis of rotation of a revolute joint, which connects the main strut to a sub-frame part, which, in turn, will be connected to the fuselage. In defining the hard points and construction frame, the co-ordinates of the left-hand main strut are used. By selecting the type of these elements to be "left", ADAMS/AIRCRAFT automatically creates the hard points and construction frame on the right-hand main strut. The main strut is then created as a geometry-based general part of steel construction. Additional geometry is added to the top of the strut by adding a link part between the inboard and outboard upper hard points.

5.2.1.2.2 Main Landing Gear Trailing Arm

The trailing arm consists of two components, the trailing arm itself and a secondary strut to which the bottom of the main landing gear shock absorber is attached. The trailing arm is defined by three hard points, which are the main strut lower hard point, a secondary strut attachment hard point and an inboard axle hard point. It is also created as a geometry-based general part constructed of steel and has added geometry in terms of a wheel axle attached to it. The

secondary strut is created in the same manner as the trailing arm by means of two hard points defining the top and bottom of the secondary strut. Again, only the left-hand hard points of both the trailing arm and the secondary strut are defined while the corresponding hard points on the right-hand side of the main landing gear are automatically generated by ADAMS/AIRCRAFT.

5.2.1.2.3 Main Landing Gear Shock Absorbers

The main landing gear shock absorber is attached to the secondary strut by means of a spherical joint and will eventually be connected to the fuselage with a revolute joint. The upper and lower cylinders are created in a similar manner to the upper and lower cylinders of the tail landing gear shock absorber. The major difference is that a construction frame is defined at the top of the upper cylinder of which the z-axis represents the reference axis for the revolute joint attachment. Two further construction frames are defined at the bottom of the upper cylinder and at the top of the bottom cylinder. The shock cylinder parts are created as geometry-based general parts, again constructed of steel and the Rooivalk-specific spring and damper are added between the two cylinders. A translational joint, between the upper and lower cylinder is also added.

5.2.1.2.4 Main Landing Gear Joints

To define the joints of the main strut, trailing arm and shock absorber, two construction frames are created. The first construction frame is located between the main strut upper hard point, the main strut lower hard point and the trailing arm end point and is used to define the rotation of the main strut and the trailing arm components. The second construction frame is located between the top hard point of the upper cylinder of the shock absorber, the attachment point between the shock absorber and the secondary strut and the attachment point between the secondary strut and the trailing arm. This construction frame is used to define the rotation of the shock absorber and the secondary strut components. A revolute joint is then created between the main strut and the trailing arm while a spherical joint attaches the shock absorber and the secondary strut. One further revolute joint is also created at the top of the main strut and a fixed joint is created at the top of the shock absorber. Both joints attach to a separate sub-frame.

5.2.1.2.5 Main Landing Gear Sub-frames

The main strut sub-frame is created from four hard points that define the corner points of the sub-frame. The two left-hand hard points are aligned with the outboard main strut hard point in the cross-sectional plane of the left-hand main strut. Equally, the other two hard points are aligned with the outboard hard point of the right-hand main strut and are aligned in the cross-sectional plane of this main strut. A sub-frame outline, which joins the four sub-frame hard points, is then added. The sub-frame for the shock absorbers is created in an identical manner. Two sub-frame attachment points are now created, one on each sub-frame, situated at the centre of the sub-frame outline geometry. A reference construction frame, a mount part and a fixed joint are also created at these points.

5.2.1.2.6 Main Landing Gear Communicators

The mount parts on the main landing gear sub-frames automatically create input communicators, which, when matched with the identical output communicator on the fuselage, connect the two structures. To connect the wheels to the trailing arm wheel axle, an output communicator is created that matches the input communicator of the main wheels. A reference construction frame is located at the inboard wheel axle hard point and determines the spin axis of the wheel around the local z-axis. The rotation of the wheel is defined as positive for a forward moving aircraft. The output communicator is situated at the outboard point of the wheel axle. The main landing gear trailing arm suspension template is now saved as a subsystem and is connected to the main wheel subsystem template, which is contained in the ADAMS/AIRCRAFT template data base. The two subsystems are connected to each other as can be seen in Appendix E.

5.2.1.3 Rigid Fuselage Template

Two hard points and two construction frames are created at the origin of the global co-ordinate system, which are used to position the airframe structure. A further 16 hard points define the end points of the beams that make up the structure. 15 rigid beams are then created as general parts and joined by fixed joints. One revolute joint allows for movement of the tail landing gear main strut in relation to the main fuselage structure. Its motion is governed by a construction frame of which the z-axis lies in the negative y-direction of the global axis system. Another construction frame is created and is located at the outermost point of the tail landing gear wheel axle, which is a geometry-based part of the landing gear strut. The z-axis of this local co-ordinate system represents the spin axis of the tail wheel. Two further construction frames are created at the centre of gravity location and the rotor hub attachment point. The latter reference frame is used to define the orientation of the revolute joint, which will allow the rotor to spin in the appropriate direction.

As a full aircraft test rig will ultimately control the simulation, it is, therefore, important that proper communication must be established between the airframe subsystem and the test rig, through communicators. Also, to have ADAMS/AIRCRAFT automatically attach the landing gear properly during the assembly process, additional communicators, which communicate with the landing gear subsystems, must be created. The first two output communicators are created at the global co-ordinate system's origin, which communicate the airframe geometry and the aircraft origin reference marker to the test rig. A third output communicator is created and attached to the centre of mass position beam upper node so that the capability to mount the test rig's manoeuvre controller parts to the airframe is provided. Two further output communicators communicate the location of the fuselage nose tip and the fuselage reference line to the test rig. Four output communicators are created on the rigid airframe and are located at the attachment points of the main landing gear main strut and oleo sub-frames as well as the upper and lower attachment points of the tail landing gear shock absorber. These output communicators match the input communicators on the relevant subsystems and are used to mount the main landing gear and tail landing gear shock absorber to the fuselage in the correct position. The tail wheel is mounted to the tail landing gear wheel axle by means of three output communicators relating mount, location and orientation to the input communicator of the same name in the tail wheel subsystem. The rigid airframe template is now saved as a subsystem and is connected to the tail wheel subsystem template, which is contained in the ADAMS/AIRCRAFT template data base. The two subsystems are connected to each other as can be seen in Appendix F.

5.2.1.4 Full Fuselage Assembly

To create the Rooivalk fuselage model, an assembly is created in the ADAMS/AIRCRAFT standard interface. The rigid airframe, the tail landing gear single post suspension, the main landing gear trailing arm suspension, the main landing gear tires and the tail landing gear tire subsystems are opened in the standard interface and combined into a new full aircraft assembly. The body subsystem, front and rear suspension subsystems as well as the front and rear wheel systems are defined from the relevant open Rooivalk model subsystems and linked to the full aircraft test rig. The subsystems are then assembled by ADAMS/AIRCRAFT into a single assembly as shown in Appendix G.

5.2.2 Static Analysis of the MSC ADAMS Fuselage Model

5.2.2.1 Modifications to the Rigid Fuselage Model

In order to perform a static analysis of the rigid fuselage vibration modes, the fuselage assembly shown in Appendix G is adapted to communicate with a full-aircraft test rig that performs the analysis. The modifications that are required involve adding a second rigid body representing the rotor assembly, adding a general airframe part to the centre beam of the fuselage and adding communicators that are required by the test rig. The rigid rotor system is added to the rigid

fuselage model by creating a geometry-based general part, at the top of the main rotor attachment beam, in the shape of a small cylinder of 545.8 kg mass, as can be seen in Appendix H. The cylinder is attached to the main rotor beam by means of a fixed joint. A general airframe part, which is attached to the centre fuselage beam, at the bottom of the main rotor beam, is required to establish communication between the test rig and the fuselage model. General analyses that can be done in ADAMS/AIRCRAFT make use of fixed wing aircraft templates in the form of shell models stored in a shared data base. The supplied fuselage models have all of the required communicators embedded in them so that the test rig can communicate with these models and visa versa. This is done by means of a general part called “Airframe”, which constitutes the physical fixed wing aircraft model. In terms of the Rooivalk fuselage model, these communicators must be created individually on a geometry-based cylindrical part, which is also called “Airframe” and is situated at the bottom of the main rotor beam, which can also be seen in Appendix H. Twelve input communicators that relay information about the fuselage aggregate mass, airframe geometry, simulation duration and ground plane reference are created on the airframe, which receive information from the test rig. A further 45 output communicators are also created on the airframe part, which supply information relating to the aircraft geometry, pilot inputs, attachment points and user defined points to the test rig. Once the two geometry-based cylinders and communicators have been added to the Rooivalk fuselage model, the static analysis can be executed.

5.2.2.2 Modes of Vibration

Any ground static analysis that is performed by ADAMS/AIRCRAFT is executed in two parts. The first part involves a ground static attitude or balance simulation in which the fuselage model is allowed to settle on its undercarriage under the influence of gravity while the second part constitutes the actual simulation itself. Both parts of the analysis are governed by a, user-defined, balance/simulation duration and the number of time steps to be used in the defined time. The correct choice of these parameters determines the successful convergence of the simulation to be performed. For the Rooivalk fuselage model a balance duration of 5 seconds with 25 time steps is found to be suitable when considering the mass and balance data used in the DYMORE program. A road data file, which is contained in the shared road template data base of MSC ADAMS, is selected to represent the ground surface on which the helicopter rests. For the static analysis a three-dimensional flat road surface is chosen. The following mass and balance information that is also used in the DYMORE model is entered in an aircraft loading configuration table:

Additional mass:	5054.24 kg
Position of additional mass: Node 66	(6.67, 0.0, 3.17 (m))
Ixx:	5647.84 m ² kg
Iyy:	26 775.1 m ² kg
Izz:	22 591.5 m ² kg

The balance simulation is now successfully executed, resulting in the fuselage configuration shown in Appendix H. The sphere at the upper point of the centre of gravity beam, just ahead of the main rotor beam represents the additional mass defined in the aircraft loading configuration file. The eigenvalue analysis, which is subsequently performed, shows that there is no deformation of the structure for the first eleven eigenvalues. The following eight eigenvalues have only real parts while eigenvalues 20 to 26 have an imaginary part. The first mode shape occurs at a frequency of 15.560 rad/sec and is a pitching mode. The first rolling mode occurs at 18.784 rad/sec and is followed by two pitching modes at 20.099 rad/sec and 45.588 rad/sec and a yawing mode at 1111.213 rad/sec (Appendix I). When comparing the pitching and rolling mode of the fuselage model to the uncoupled blade frequency determined in figure 4.5.3.1, it can be seen that the lead-lag and the fuselage pitch/roll frequencies intersect at a rotor frequency of approximately 29 rad/sec (276.93 rpm) and 32 rad/sec (305.58 rpm) respectively as shown in figure 5.2.2.2.

ROTATION VS LEAD-LAG FREQUENCY

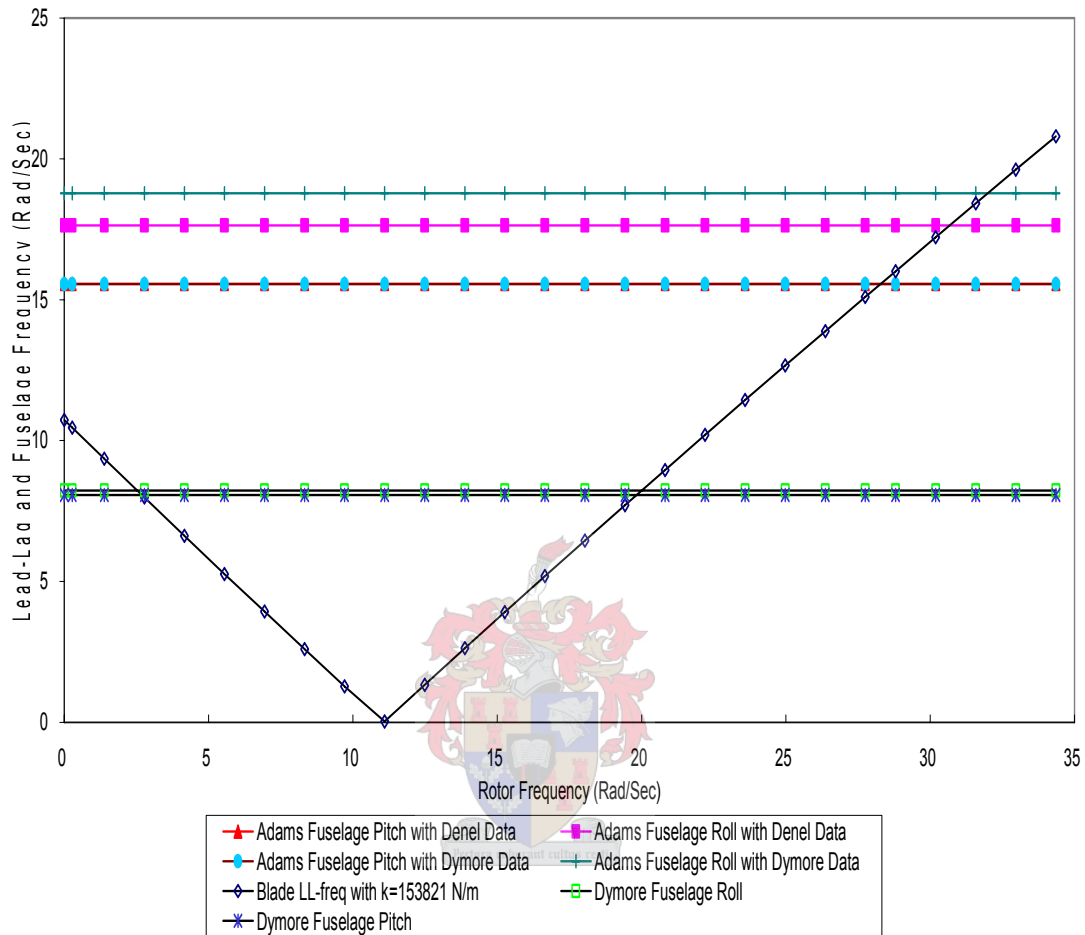


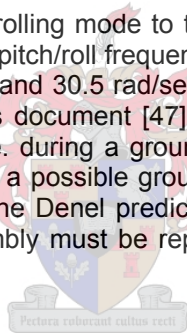
Figure 5.2.2.2 MSC ADAMS uncoupled fuselage and blade frequencies

When using the DYMORE data in the MSC ADAMS fuselage model, the frequencies at which a possible ground resonance may occur (29 and 32 rad/sec) are significantly higher than those in the original DYMORE model (19.63 rad/sec). The possible reason for this is twofold. Firstly, the rigid beams of the original DYMORE model are modelled in such a way that their total combined weight is 12.312 kg, which makes them practically massless. In the MSC ADAMS model, the general parts that make up the fuselage are constructed of steel and must, therefore, have a certain mass. Although this mass is kept to a minimum in that each rigid beam weighs 1 kg, the combined mass of the MSC ADAMS rigid beams amounts to 15 kg. The tail landing gear shock absorber is also constructed of steel and weighs 77.39 kg while the main landing gear structure weighs 476.87 kg. Added to this are the two main wheels (91.62 kg) and the tail wheel (9.52 kg), which adds up to a total combined weight of 670.4 kg. The MSC ADAMS fuselage model is, therefore, 658 kg heavier than the original DYMORE model. Secondly, the tire models used in ADAMS/AIRCRAFT are realistic models of actual aircraft tires, which incorporate vertical damping of the tire. In the original DYMORE model, the helicopter's tires were modelled by springs. This simplification has a direct influence on the vibration modes as the vertical damping of the tires influences the natural frequency of the fuselage structure.

The increase in mass and the vertical damping of the landing gear tires in the MSC ADAMS model is, however, deemed acceptable as both factors make the model more realistic than the DYMORE model. The original model assumed a total aircraft weight of 5600 kg, which coincides with the basic aircraft weight given in the Denel technical drawings [38]. Technical documentation also supplied by Denel [48], however, indicates that the Rooivalk actual basic weight is 5672 kg. Under normal operating conditions, the weight of the basic operating fluids (98 kg), the weight of the pilots (180 kg) and the fuel must also be considered. If it is assumed that the aircraft under investigation has 300 kg of fuel on board, the total operating weight is 6250 kg. This means that the real aircraft would be operating at 650 kg above the weight assumed in the original DYMORE model. The added aircraft weight of the MSC ADAMS fuselage model (658 kg), therefore, represents a more realistic weight for the fuselage model. The vertical damping in the tires also contributes to a more realistic tire model for the analysis.

Additional to the increase in weight and the vertical tire damping, actual mass and balance information supplied by Denel [48] is incorporated into the fuselage model. The centre of mass is moved slightly backward to a position behind the main rotor beam as can be seen in Appendix J. Another static analysis is performed, which shows a slight shift in the eigenvalues. The first pitching mode shape of the fuselage model remains the same as in the first analysis and occurs at a frequency of 15.562 rad/sec. There is, however, a slight change in the frequency of the first rolling mode, which now occurs at 17.638 rad/sec. The second and third pitching modes occur at 18.613 rad/sec and 44.741 rad/sec respectively and the first yawing mode now has a frequency of 1026.899 rad/sec. These mode shapes are shown in Appendix K.

Again comparing the first pitching and rolling mode to the uncoupled blade frequency, it can be seen that the lead-lag and the fuselage pitch/roll frequencies now intersect at a rotor frequency of approximately 29 rad/sec (276.93 rpm) and 30.5 rad/sec (292.21 rpm) as is also shown in figure 5.2.2.2. In the Denel blade frequencies document [47], the calculations are done for the worst case scenario for ground resonance i.e. during a ground run-up with flat pitch at 275 rpm. The MSC ADAMS fuselage model indicates a possible ground resonance at 276.93 rpm and 292.21 rpm, which compares favourably with the Denel prediction. In order to verify this, however, the rigid body representing the rotor assembly must be replaced with a full model of the helicopter main rotor system.



5.2.3 MSC ADAMS Main Rotor Model

The Rooivalk main rotor system is constructed from five individual components i.e. the main rotor hub and the four identical flexible blades. The rotor system is classified as a propulsion subsystem in ADAMS/AIRCRAFT and is attached to the main rotor beam of the rigid fuselage at node 69 as was done in the original DYMORE model.

5.2.3.1 Main Rotor Hub

5.2.3.1.1 Hard Points

The main rotor hub topology is defined by 26 hard points. Two hard points define the top and bottom of the main rotor shaft, which is inclined at 5 degrees from the vertical towards the nose of the aircraft. Three sets of four hard points define the position of the flap hinges, the lead-lag hinges and the pitch hinges to which each of the four rotor blades will be attached. Four hard points are used to define a sub-frame attachment part at the bottom of the rotor spin axis while the remaining 8 hard points define the end points of the geometry-based parts used to define the rotor hub structure.

5.2.3.1.2 Construction Frames

Construction frames are used to orientate the geometry-based parts that make up the main rotor hub and to define the axis of rotation of the revolute joints that are used in the model. The orientation construction frames allow the entire rotor hub to be tilted at an angle of 5 degrees while the rotation construction frames define the motion about their respective z-axes. Of the 34 construction frames that are defined for the main rotor hub, 21 are used for orientation purposes and 13 define revolute joints. These joints are used to describe the motion of the four flap hinges, the four lead-lag hinges and the four pitch change hinges as well as the rotor spin axis of the main rotor shaft. This last construction frame is orientated in such a way that the rotor spins around the negative z-axis i.e. in a clock-wise direction when viewed from above.

5.2.3.1.3 General Parts

A single geometry-based steel cylinder weighing 16 kg is created for the rotor shaft while four sets of three steel cylinders, all of 10 cm diameter, are used between the top of the rotor shaft and the flap hinges. Each of these cylinders weighs 3.2 kg and is constructed to allow for the cross-sectional mass property changes that were implemented in the original DYMORE model. Single cylinders are incorporated between the flap hinges, the lead-lag hinges and the pitch hinges, giving a total of 21 rigid parts of a total weight of 80 kg. A single massless sub-frame part, similar to those used in the tail landing gear shock absorber is created using the four corner hard points at the bottom of the rotor shaft. This sub-frame allows for the attachment of the rotor hub and eventually the entire main rotor structure to the top of the rotor attachment beam (node 69) of the rigid fuselage structure.

5.2.3.1.4 Attachments and Communicators

Most of the rigid cylinders and the sub-frame are attached by means of fixed joints except for the lead-lag components, which are attached to the rotor centre structure by means of a bushing. The stiffness and damping characteristics supplied by Denel [39] are incorporated into the bushing by modifying the property file of a general bushing found in the ADAMS/AIRCRAFT shared template directory. A fixed joint is also used for the flap hinge as the droop stops are not modelled and a simple revolute joint would cause the blades to fall to the ground during the balance simulation. One revolute joint is created between the bottom of the rotor shaft and the sub-frame attachment part to facilitate the rotation of the rotor around the z-axis of the spin axis construction frame.

Two input communicators are created on the main rotor hub, one of which receives balance duration information from the full aircraft test rig while the other receives attachment information from the rigid fuselage model to attach the rotor hub in the correct position. No output communicators are required for the main rotor hub as the main rotor blades are attached directly to the hub by means of the pitch change mechanism joints on the outermost points of the main rotor hub. The complete hub is shown in Appendix L.

5.2.3.2 Main Rotor Blade

The four identical rotor blades are each defined by ten hard points, which represent the end points of nine beam elements. The length of these beam elements is equal to the distance between the blade nodes of the original DYMORE model (node 84 to 96, 105 to 117, 126 to 138 and 147 to 159 in Appendix B). Each beam element is defined in terms of its mass and mass moments of inertia in a local axis system attached to the element. The local axis systems are defined by construction frames that also define the blade twist of main rotor blades. The beam elements are joined by fixed joints, which make the blades rigid. Although the blades are flexible in reality and should, therefore, be modelled by flexible beam elements, ADAMS AIRCRAFT has only one flexible short beam of 50 cm length in its shared data base. The dimensions of this beam and its stiffness characteristics vary greatly from the characteristics of the Roivalk main rotor blade and cannot be used for the rotor blade model. The flexible beam elements that are

required to model the blade would have to be developed in a finite element model such as MSC NASTRAN and imported into ADAMS AIRCRAFT as modal neutral files. As the flexible beam elements cannot be developed or changed within the ADAMS AIRCRAFT software package, the main rotor blades are, initially, assumed to be rigid. These rigid blades are then attached to the pitch hinges of the main rotor hub at nodes 84, 105, 126, and 147 of Appendix B. The full main rotor model is shown in Appendix M.

5.2.4 Dynamic Analysis of the full Rooivalk Model with Rigid Blades

The full ADAMS AIRCRAFT Rooivalk model shown in Appendix N is developed by creating subsystems from the templates designed for the fuselage, main landing gear structure, main landing gear tires, tail landing gear shock absorber, the tail landing gear tire and the main rotor. These subsystems are combined into a full aircraft assembly in the ADAMS AIRCRAFT standard interface. Communicators in each of the subsystems relay position information to allow the subsystems to attach in the correct configuration. Once all of the subsystems are attached, the full aircraft assembly is ready for a ground static attitude analysis. The analysis is performed in the same manner as the static analysis described in paragraph 5.2.2 with the major difference that the full rotor model is attached to the fuselage and is rotating at 275 rpm. A balance duration of 10 seconds with 2000 time steps and a simulation time of 20 seconds with 2000 time steps is chosen. The balance simulation is included in the results. No disturbance of the main rotor lead-lag hinge is included in the simulation as the disturbance of the helicopter is supplied by the tail landing gear impacting with the ground when the helicopter model moves from its design position (fuselage centre line parallel to the ground with the tail wheel in the air) to its balance position (all three wheels on the ground). Twelve analyses are done, ranging from a single point failure of the Vibration Isolation System (VIS) to a multiple point failure of the VIS, main landing gear, tail landing gear and a lead-lag damper. The results are summarised in Appendix O.

In analysis 12, the damping of all three tires is reduced to 0.001% of their original value. At the same time the damping of all three shock absorbers is also reduced to 0.001% of the fully functional value and the lead-lag damping on one of the rotor blades is reduced by 20%. As can be seen in Appendix P, there is a slight increase in the pitching motion of the aircraft as well as the rotation of the lead-lag hinge. Both increases in amplitude may indicate the onset of the ground resonance phenomenon where the first uncoupled pitching frequency of the fuselage is matched to the blade frequency at 275 rpm. In order to verify this, further analyses are done to determine whether the increase in amplitude of the pitching and lead-lag motion occurs at other rotor speeds as well.

In the first analysis, the rotor speed is reduced to 250 rpm while keeping the aircraft configuration the same as in analysis 12. At 250 rpm the amplitude of the rolling motion of the aircraft centre of gravity reduces to approximately 0.00075 rad while the pitching motion is undamped with negligible amplitude as can be seen in Appendix Q. Appendix Q also shows that the lead-lag velocity is also no longer increasing, which implies that ground resonance does not occur at a rotor speed of 250 rpm. In the second analysis, the rotor speed is increased to 350 rpm and analysis 12 is repeated. Again no indication of ground resonance is found in terms of the aircraft centre of gravity roll and pitch motion or the lead-lag motion of the rotor blade (Appendix R). In order to determine where the upper boundary for ground resonance ends, analysis 12 is repeated while progressively reducing the rotor speed. In this way it is determined that at approximately 320 rpm there is no increase in the rolling motion of the aircraft centre of gravity while there is a slight increase in the pitching and lead-lag motion (Appendix S).

The ground resonance region for the Rooivalk model is, therefore, determined to lie between 275 rpm and 320 rpm. At 275 rpm the uncoupled fuselage pitching frequency coincides with the main rotor blade frequency and an increasing pitching motion of the helicopter is observed. As can be seen in figure 5.2.2.2, the first uncoupled fuselage roll frequency and the main rotor blade frequency intersect at approximately 30.5 rad/sec (292.21 rpm) rotor speed, which lies within the ground resonance rotor speed range. In order to determine the helicopter model's reaction at 292

rpm, analysis 12 is again repeated at this speed. As can be seen in Appendix T, there is a steady increase in both the rolling and pitching motion of the helicopter model. The frequency of the first fuselage rolling mode coincides with the frequency of the main rotor blade. The interaction of the first fuselage pitching frequency and main rotor blade frequency remain evident and is responsible for the increasing pitching motion. As can be expected, the growing rolling and pitching motion of the helicopter model is accompanied by an increase in amplitude of the lead-lag motion of the rotor blade.

It can now be concluded that the ground resonance phenomenon for the Rooivalk model occurs between 275 rpm and 320 rpm, at an aircraft weight of 6258 kg, with tire and shock absorber damping reduced to 0.001% and the lead-lag damping on a single blade reduced by 20%. At 292 rpm rotor speed the phenomenon is most pronounced. In order to determine whether or not a further disturbance of any lead-lag hinge on the main rotor could influence this conclusion, the first 12 analyses are re-investigated without the balance simulation being part of the results. In order to excite the helicopter model into a ground resonance state, the lead-lag hinge on one of the main rotor blades is disturbed by a point torque of 45 kN-meter acting on the hinge. This results in a lead change in velocity of approximately 0.5 rad/sec in the direction of rotation of the rotor as can be seen in Appendix U. The results are summarised in Appendix V.

The twelve analyses performed with the lead-lag disturbance of one rotor blade follow the same pattern as the first twelve analyses with the ground resonance phenomenon only becoming apparent in analysis 12. In this analysis there is no increase in the rolling motion of the helicopter model but there is an increase in its pitching motion. This increase is not as pronounced as in the first batch of analyses, which is to be expected as the lead-lag disturbance is not as severe as the disturbance in pitch during the first analyses. The second batch of analyses does, however, confirm that the ground resonance phenomenon becomes evident at 275 rpm with the helicopter model in the configuration described in analysis 12. This supports the previous conclusion that ground resonance occurs between 275 rpm and 320 rpm at an aircraft weight of 6258 kg with the tire and shock absorber damping reduced to 0.001% and the lead-lag damping of one blade reduced by 20%. The ground resonance phenomenon, again, is most evident at 292 rpm as shown in Appendix W.

5.2.5 Refinement of the MSC ADAMS Main Rotor Model

The results achieved with the rigid blade rotor model compare favourably with the predicted worse case scenario predicted in Denel Aviation documentation [47]. This indicates that assuming the rotor blades to be rigid is a valid simplification of the helicopter model. Previous ground resonance analyses [17, 27, 28] have also shown this to be true. In reality, however, the blades are not rigid and this allows the blade to bend and twist under various applied loads. Incorporating the bending stiffness, the torsional stiffness and the shear stiffness of the blades into the main rotor model allows for the accurate modelling of the main rotor blade as is seen in the DYMORE model [49].

In an attempt to increase the accuracy of the MSC ADAMS main rotor blade model, the fixed joints connecting the nine beam elements of each blade are replaced with bushings. The stiffness characteristics of the real rotor blade, as supplied by Denel Aviation [37] and incorporated in the DYMORE model are now incorporated into each bushing by modifying the property file of a general bushing found in the ADAMS AIRCRAFT shared template directory, as was done for the four lead-lag bushings of the main rotor hub. The new blade model template is now stored as a subsystem and is then combined with the fuselage, main landing gear and tail landing gear subsystems into a new full aircraft assembly. The initial configuration of the helicopter is that of a single point failure of the Vibration Isolation System as was done for the first analysis of Appendix O. When using a balance-duration of 10 seconds with 2000 time steps and a simulation time of 20 seconds with 2000 time steps, the simulation fails to converge. Due to the specified rotor spin-up time of 1 second that was used in the first dynamic analysis, the blade sections are displaced at greater angles than is allowed in the MSC ADAMS simulation. The rotor spin-up time is now

gradually increased from 1 second to 20 seconds but the simulation still fails. For each of the incremental increases in rotor spin-up, the length of the balance time and the number of time steps is varied from 5 seconds to 40 seconds and 1000 to 3000 time steps respectively. After 102 simulation attempts the simulation still fails. The best result that could be achieved is a simulation failure after 6.9 seconds balance time at a rotor spin-up time of 15 seconds and using 2500 time steps.

In an example of modelling a nonlinear deformation given in the MSC ADAMS help file [50], the nonlinear deformation of a spin-up cantilever beam is described. In this example it is stated that the modal formulation of a flexible body in MSC ADAMS is inherently linear. The premature linearization assumption prevents MSC ADAMS from recognizing the stiffening of the beam due to centrifugal forces. When the nonlinear effects are not modelled, MSC ADAMS can only predict that the beam will collapse. The example shows that the cantilever beam deforms unrealistically because MSC ADAMS assumes linear deformations and the simulation fails at approximately 10 seconds due to divergence of the beam. Premature linearization may, therefore, also prevent the successful simulation of the helicopter rotor blade model with the stiffness characteristics of the blade modelled with bushings. In order to simulate the nonlinear behaviour of the rotor blade, it must be modelled with short flexible segments that behave linearly. These flexible segments cannot be created in MSC ADAMS and have to be designed in a finite element package such as MSC NASTRAN and then imported into MSC ADAMS as modal neutral files.



6. Conclusions and Recommendations

6.1 Conclusions

6.1.1 Multi-body Dynamics Software Packages and the Ground Resonance Phenomenon

Multi-body dynamics software packages are effective tools in emulating and analysing the ground resonance phenomenon on a conventionally articulated main rotor helicopter. This is made possible by powerful software packages that have been specifically developed for aircraft design and testing. The technological advances in terms of computing power and speed make modelling and analysis of helicopter ground resonance a viable alternative to actual, full aircraft testing. Two packages that are well suited to the task are DYMORE and MCS ADAMS.

6.1.1.1 The DYMORE Software Package

As shown in chapter 4.5 and 4.6, the DYMORE software package is fully capable of analysing the ground resonance phenomenon on a conventionally articulated main rotor helicopter such as the Rooivalk Combat Support Helicopter. Both static and dynamic analyses can be performed to define operational conditions in which ground resonance may occur.

The four main rotor blades can be identically modelled with stiffness and inertia data provided by the aircraft manufacturer, which is then directly supplied to the program. Not using the CROSEC pre-processing module does not affect the accuracy of the blade model significantly. The CROSEC model does, however, provide a more complete model of the blade elasticity.

6.1.1.2 The MSC ADAMS Software Package

MSC ADAMS and, in particular, ADAMS AIRCRAFT is an effective tool to analyse the complex behaviour of mechanical systems such as conventionally articulated main rotor helicopters of which the Rooivalk Combat Support Helicopter is a prime example. Although ADAMS AIRCRAFT is designed to analyse fixed-wing aircraft, new design templates of a helicopter airframe configuration can, quite easily, be created. Both static and dynamic analyses can be performed in order to define the operational conditions in which ground resonance may occur.

6.1.2 Operational Conditions in which Ground Resonance may occur

Specific operational conditions, in which ground resonance is predicted to occur, can clearly be identified by using multi-body dynamics software packages. This is because, once a model has been built in these packages, it is relatively easy to change the aircraft mass, the main rotor speed, the damping characteristics of landing gear shock absorbers / tires or the damping characteristics of the lead-lag dampers on the main rotor blades. Each of these changes represents a different operational condition for which the ground resonance phenomenon can be investigated. Both the DYMORE and the MSC ADAMS software packages have this capability.

6.1.2.1 The DYMORE Model

The DYMORE model predicts that ground resonance on the Rooivalk will occur at an aircraft operating mass of 5600 kg at 187 rpm rotor speed with no Vibration Isolation System and no vertical damping of the main and tail landing gear tires. Removing the damping from all three landing gear tires changes the damping characteristics of the fuselage and, therefore, influences the translational motion of the rotor shaft attachment point. The lateral translation of the rotor shaft attachment point shows an increase in amplitude from 0 cm to 7 cm within 14 seconds, indicating an unstable situation. Removing the tire damping, therefore, gives rise to ground resonance instability at the given operational conditions. As can be expected, the increasing

rolling motion of the helicopter is associated with an increase in amplitude of the lead-lag motion of the rotor blades.

Removing the damping in all three tires and all three landing gear shock absorbers, under the same operating conditions of 5600 kg aircraft weight and 187 rpm rotor speed, creates a scenario where the fuselage provides no damping and only the lead-lag dampers of the main rotor are operational. This increases the ground resonance instability. The lateral translation of the rotor shaft attachment point shows a significant instability in that the amplitude of the motion rapidly increases from zero to 12 cm within 14 seconds. This ground resonance instability is also reflected in the increasing rotation of the lead-lag hinges.

6.1.2.2 The MSC ADAMS AIRCRAFT Model

The ADAMS AIRCRAFT model predicts that ground resonance on the Rooivalk will occur between 275 rpm and 320 rpm, at an aircraft weight of 6258 kg, with the tire and shock absorber damping reduced to 0.001 % of the fully operational values and the lead-lag damping on a single blade reduced by 20 %. At 292 rpm rotor speed the phenomenon is most pronounced.

6.1.2.3 Differences between the two Models

When using the DYMORE data in the MSC ADAMS fuselage model, the frequencies at which a possible ground resonance may occur are significantly higher than those in the original DYMORE model. The reason for this is that the MSC ADAMS fuselage model is 658 kg heavier than the original DYMORE model and the tire models used in MSC ADAMS are more realistic than those used in the DYMORE model. The added weight represents a more realistic weight for the fuselage model. The vertical damping in the tires also contributes to a more realistic tire model for the analysis.

6.1.3 Number of Failure Cases required for possible Ground Resonance

No single point failure should cause ground resonance on a conventionally articulated main rotor helicopter such as the Rooivalk Combat Support Helicopter. Both the DYMORE and ADAMS AIRCRAFT model predict that ground resonance on the Rooivalk Combat Support Helicopter can only occur in extreme cases of multiple point failures. As such failures are highly unlikely to occur in normal flight operations this implies that the aircraft must sustain extreme battle damage before ground resonance becomes a problem. With such damage it is also unlikely that the aircraft will be capable of sustaining flight or executing a normal landing. It, therefore, seems that the Rooivalk Combat Support Helicopter should not easily encounter ground resonance. Both the DYMORE and the MSC ADAMS models indicate this.

6.1.3.1 The DYMORE Model

The DYMORE model predicts that no single point failure, such as the loss of the Vibration Isolation System, will cause ground resonance on the Rooivalk Combat Support Helicopter. A four-point failure with complete loss of the Vibration Isolation System and all tire damping is required before ground resonance can occur.

6.1.3.2 The MSC ADAMS AIRCRAFT Model

The ADAMS AIRCRAFT model predicts that no single-point failure, such as the loss of the Vibration Isolation System, will cause ground resonance on the Rooivalk Combat Support Helicopter. A seven point failure with a complete loss of the Vibration Isolation system, a drastic reduction in tire and shock absorber damping as well as a 20 % reduction in the lead-lag damping of a single main rotor blade is required before ground resonance can occur.

6.2 Recommendations

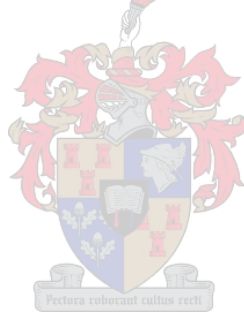
6.2.1 Improvements to the Main Rotor Model

To improve the rotor model used in ADAMS AIRCRAFT, the rotor blades should be accurately modelled in a finite element program and then imported as modal neutral files. The blade must be modelled with short, flexible sections that behave linearly in order to satisfy the linear deformation assumption of MSC ADAMS. To do so more accurate information relating to blade materials and exact construction of the blades is required, which was not available for this research project. Lead-lag stiffness information must also be as accurate as possible.

6.2.2 Verification of Data

In order to further verify the conclusions reached in this research project, the results of the analyses should be compared to actual ground test data obtained from the actual aircraft. This data could be used to further improve the accuracy of the model. Unfortunately, no such data was available for this research project.

The data provided by Denel Aviation is based on the Rooivalk EDM pre-production aircraft. Although no major changes have been made to the production aircraft in terms of the airframe, the rotor head or the rotor blades, it would be advantageous to use data from a production aircraft. This would increase the accuracy of the model and make it representative of the production aircraft used by the South African Air Force.



References

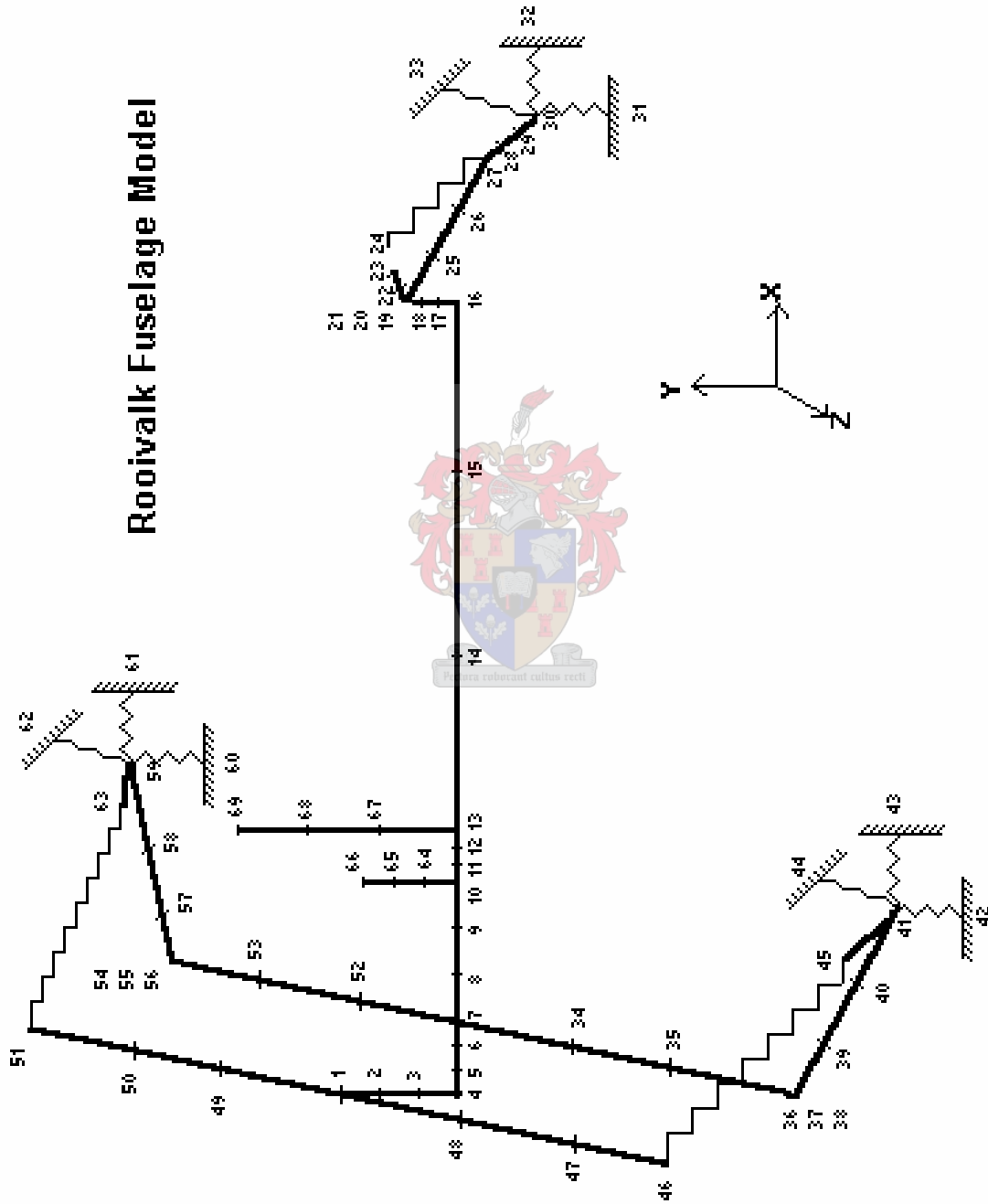
1. R. P. Coleman, A. M. Feingold, Theory of self-excited mechanical oscillations of helicopter rotors with hinged blades, NACA Report 1351, 1958.
2. R. E. Donham, S. Y. Cardinale and I. B. Sachs, Ground and air resonance characteristics of a soft in-plane rigid rotor system. Journal: American Helicopter Society, Volume 14, Issue 4, 1969.
3. R. T. Lytwyn, W. Miao and W. Woitch, Airborne and ground resonance of hinge-less rotors. Journal: American Helicopter Society, Volume 16, Issue 2, 1969.
4. W. G. Bousman, D. L. Sharpe and R. A. Ormiston, An experimental study of techniques for increasing the lead-lag damping of soft in-plane hinge-less rotors, 32nd Annual National V/STOL Forum of the American Helicopter Society, Washington DC, May 1976.
5. D. H. Hodges, An aeromechanical stability analysis for bearing-less rotor helicopters. Journal: American Helicopter Society, Volume 24, Issue 1, 1979.
6. S. P. Dawson, An experimental investigation of the stability of a bearing-less model rotor in hover. Journal: American Helicopter Society, Volume 28, Issue 4, 1983.
7. H. L. Price, Avoidance of ground resonance. Journal: Aircraft Engineering, Volume 32, Issue 377, 1960.
8. R. F. Ganiev and I. G. Pavlov, On the theory of ground resonance of helicopters. Journal: Prikladnaya Mekhanika, Volume 9, Issue 5, 1973.
9. M. N. Nahas, Helicopter ground resonance – A spatial model analysis. Journal: Aeronautical Journal, Volume 88, Issue 877, 1984.
10. P. P. Friedman, Coupled helicopter rotor/body aeromechanical stability comparison of theoretical and experimental results. Journal: Journal of Aircraft, Volume 22, Issue 2, 1985.
11. D. M. Tang, Influence of nonlinear blade damping on helicopter ground resonance instability. Journal: Journal of Aircraft, Volume 23, Issue 2, 1986.
12. O. A. Bachau and N. K. Kang, Multibody formulation for helicopter structural dynamic analysis. Journal: Journal of the American Helicopter Society, Volume 38, Issue 2, 1993.
13. Author unknown, Super-Cobra and Huey updates. Paper presented at the American Helicopter Society 59th annual forum, 6 to 8 May 2003.
14. E. Roberts Wood, Structural dynamics analysis of the RAH – 66 Comanche helicopter (1998).
15. Salvatore P. Rafanello, Modelling the coupled rotor/fuselage response of the H-3 Sea King utilizing the NPS full nonlinear response. Master of Science in Aeronautical Engineering, March 1999.
16. Author unknown, Westland Helicopters Expand Software. Mechanical Dynamics press release, May 2002.

17. L. Momtarrubio and I. Sharfe, Influence of landing gear on helicopter ground resonance. Journal: Canadian Aeronautics and Space Journal, Volume 48, Issue 2, June 2002.
18. O. A. Bauchau, Dymore Users Manual, Center of Excellence in Rotorcraft Technology, Rensselaer Polytechnic Institute, Troy, New York, 23 November 1994.
19. T. L. Ciastula and P. D. MacMahon, Electronics aids testing of British helicopter. Journal: British Communications and Electronics, Volume 2, Issue 7, 1955.
20. R. Schroeder, Influence of dampers on ground resonance systems by the example of the DFVLR rotor test stand. Journal: Zeitschrift fuer Flugwissenschaften und Weltraumforschung, Volume 2, Issue 2, 1978.
21. G. Seitz and T. Krysinski, Overview of Tiger dynamics validation program. Annual Forum Proceedings – American Helicopter Society, Volume1, 1992.
22. C. S. Robinson, Modelling and analysis of helicopter ground resonance utilizing symbolic processing and dynamic simulation software. Naval Postgraduate School, Monterey, California, USA, March 1997.
23. D. L. Kunz, Nonlinear analysis of helicopter ground resonance. Journal: Real World Applications, Volume 3, Issue 3, 2002.
24. M. Yang and I. Chopra, Vibration prediction for a rotor system with faults using a coupled rotor-fuselage model. Journal: Journal of Aircraft, Volume 41, Issue 2, 2004.
25. F. Gandhi and E. Hathaway, Optimized aero-elastic coupling for the alleviation of helicopter ground resonance. Pennsylvania State University, USA, 1998.
26. S. J. Kim and C. Y. Yun, Performance comparison between piezo-electric and elastomeric lag dampers on the ground resonance stability of a helicopter. Journal: Journal of Intelligent Material Systems and Structures, Volume 12, Issue 4, 2001.
27. H. Kang, Rotor blade lag damping using imbedded chord-wise absorbers. Pennsylvania State University Graduate School, Department of Aerospace Engineering, August 2001.
28. G. Kowaleczko and Z. Dzygadło, Effect of free-play in rotor blade hinges on the nonlinear ground resonance of a helicopter. Journal: Aircraft Engineering and Aerospace Technology – An International Journal, Volume 74, Issue 6, 2002.
29. J. S. Petriei, G. A. Lesieutre and E. C. Smith, Helicopter blade lag damping using embedded fluid elastic inertial dampers. Proceedings of the 45th AIAA/ASME/ASCE/AHS/ASC Structures, Structural Dynamics and Material Conference, Palm Springs, California, USA, April 2004.
30. Y. Zhao, Y. T. Choi and N. M. Wereley, Semi-active damping of ground resonance in helicopters using magnetorheological dampers. Journal: Journal of the American Helicopter, Volume 49, Issue 4, October 2004.
31. C. Lewis and J. H. Darbo, Helicopter ground resonance. Journal: Flight Safety Information Journal, 2 May 2006.
32. W. Johnson, Helicopter Theory, Princeton University Press, 1980.
33. H. R. Harrison and T. Nettleton, Advanced Engineering Dynamics, 1997.

34. O. W. Eshbach, Handbook for Engineering Fundamentals, 1953.
35. A. R. S. Bramwell, Helicopter Dynamics, Department of Aeronautics, The City University, London, 1976.
36. O. A. Bachau and N. J. Theron, Energy decaying scheme for nonlinear elastic multi-body systems. Journal: Computers & Structures, Volume 59, Issue 2, 1996.
37. Author unknown, Title unknown, Aerospatiale document no. 332.A.04.3621, Date unknown.
38. Author unknown, Title unknown, Denel Aviation technical drawing no. 08A0011D001 Sheet 3, Frame 9 of 28 and frame 12 of 28, Date unknown.
39. H. Clark, Ground Resonance Info, Denel Aviation Fax, 21 May 1996.
40. B. P. Flannery, S. A. Teutolsky and W.T. Vetterling, Numerical Recipes. The Art of Scientific Computing, Cambridge University Press, Cambridge, 1990.
41. Author unknown, MLG Formal Calculation, Denel Aviation Document, Project 21215-OP4, 19 Sep 1987.
42. Author unknown, TLG Formal Calculation, Denel Aviation Document, Project 21220-OP4, 23 Oct 1987.
43. Jandel Scientific Tablecurve Version 2.14, Computer Software, AISN Software, 1989,1990.
44. Author unknown, Title unknown, Extract from document: Section 8.4: Ground Resonance of the "Advanced Chinook" Tandem Helicopter, Date unknown.
45. W. Remesperger and E. Kokott, Basic Theory for Calculating the Operation of Hydraulic Shock Absorbers, Communication to A.T.Z. from the Remensperger and Kern Laboratory, Apparate- und Maschinenbau, Suderburg, Kr Uelzen, 1951.
46. R. R. Craig, Jr, Mechanics of Materials, Second Edition, John Wiley & Sons, 1999.
47. H. Clark, Calculation of Blade Frequencies, Denel Aviation Fax, 5 November 1996.
48. H. Clark, Mass and Balance Info, Denel Aviation Fax, 25 November 1996.
49. O.W.J. ten Heggeler, Composite Beam Modelling of the 332A.04.11.0024.01 Rotor Blade, into a Ground Resonance Analysis of the Rooivalk Helicopter, July 1997.
50. MSC ADAMS help \ flex \ tutorials \ flex_nonlin.pdf. MSC ADAMS help file, MSC Software Corporation, 2004

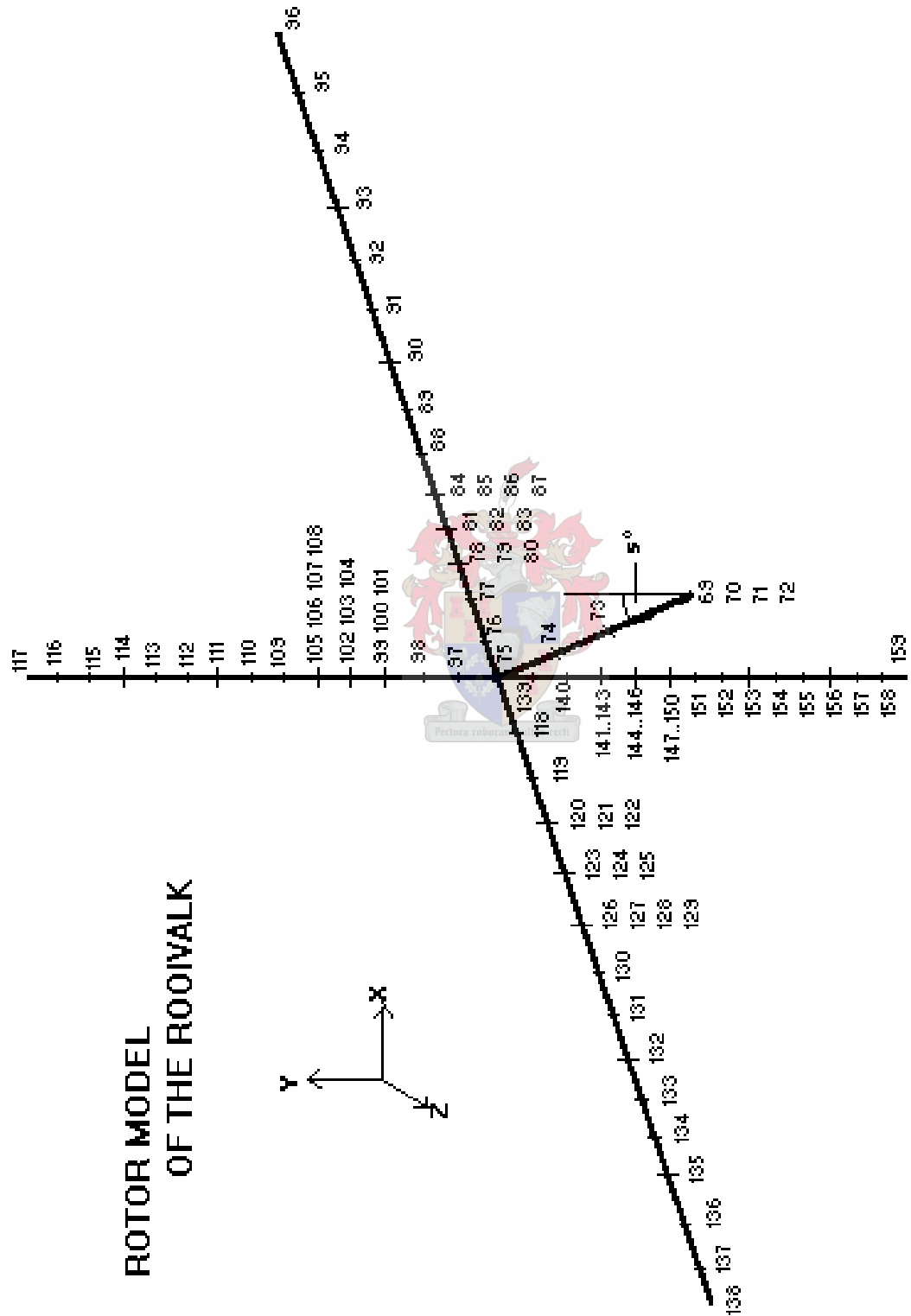
Appendix A

DYMORE Roovalk Fuselage Model



Appendix B

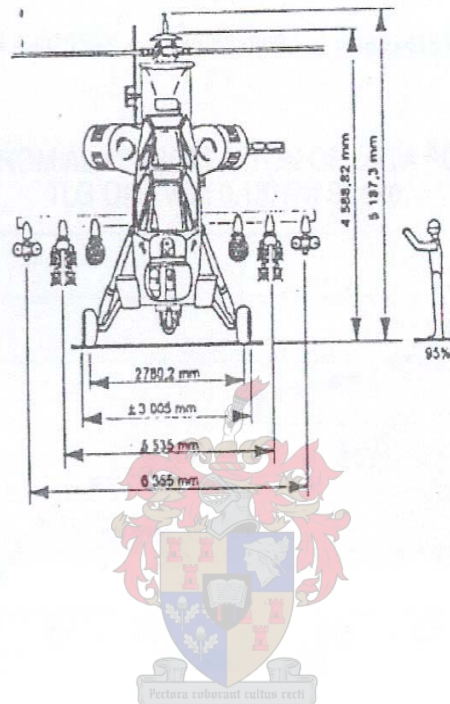
DYMORE Roovalk Rotor Model



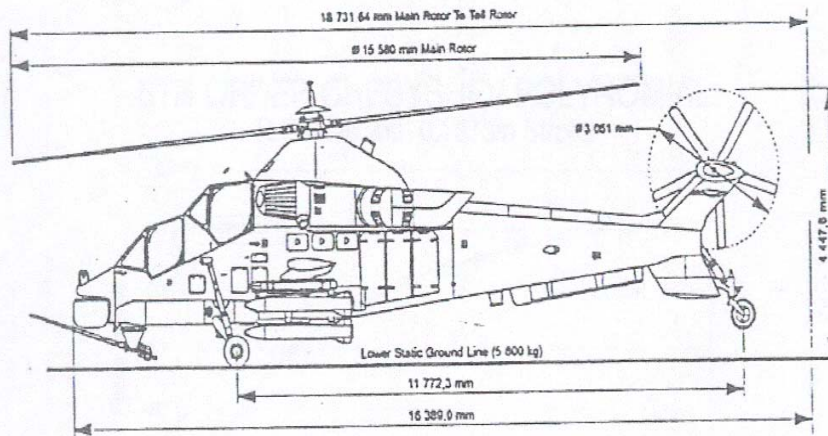
Appendix C

Rooivalk Information Sheet

Front View Dimensions:

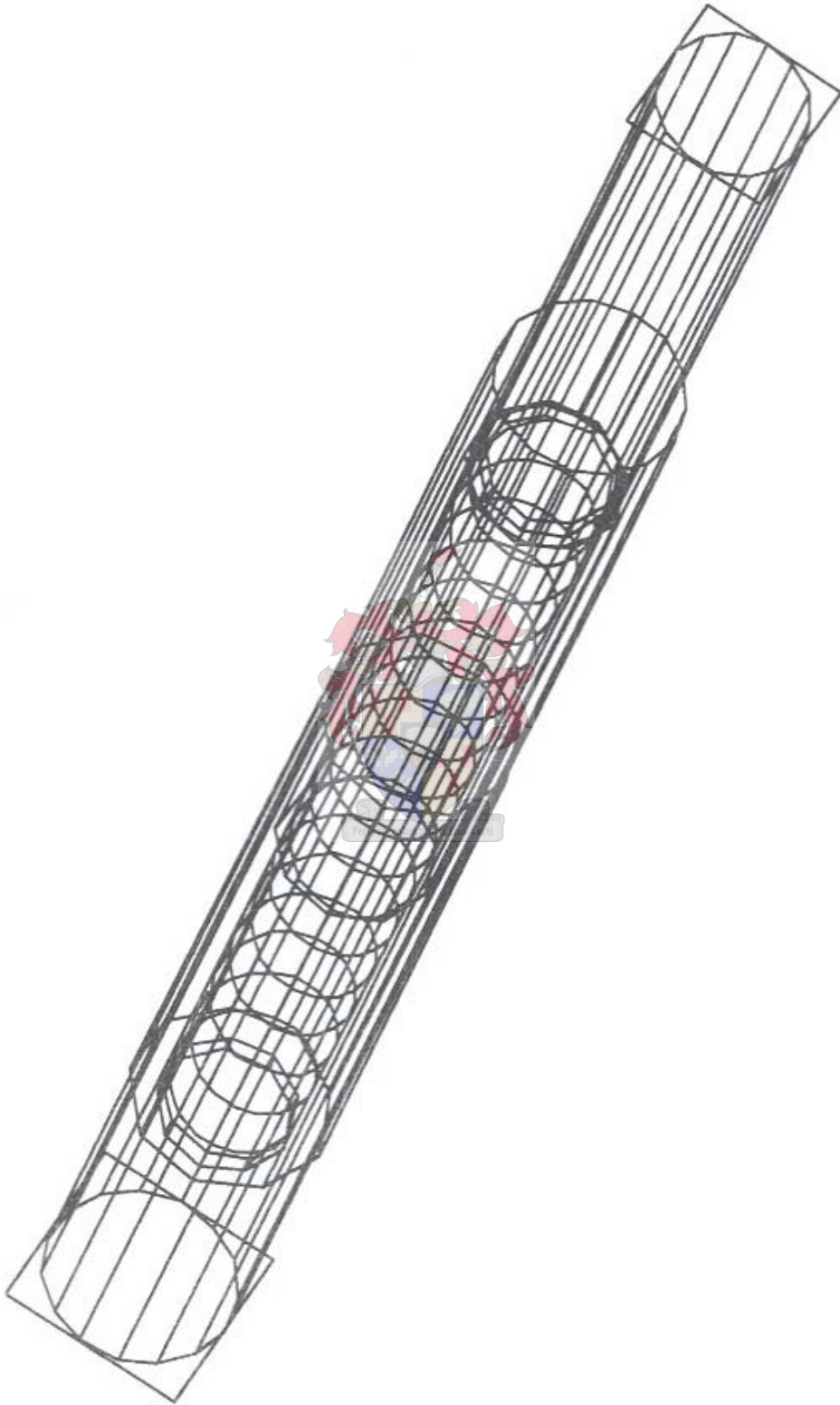


Side View Dimensions:



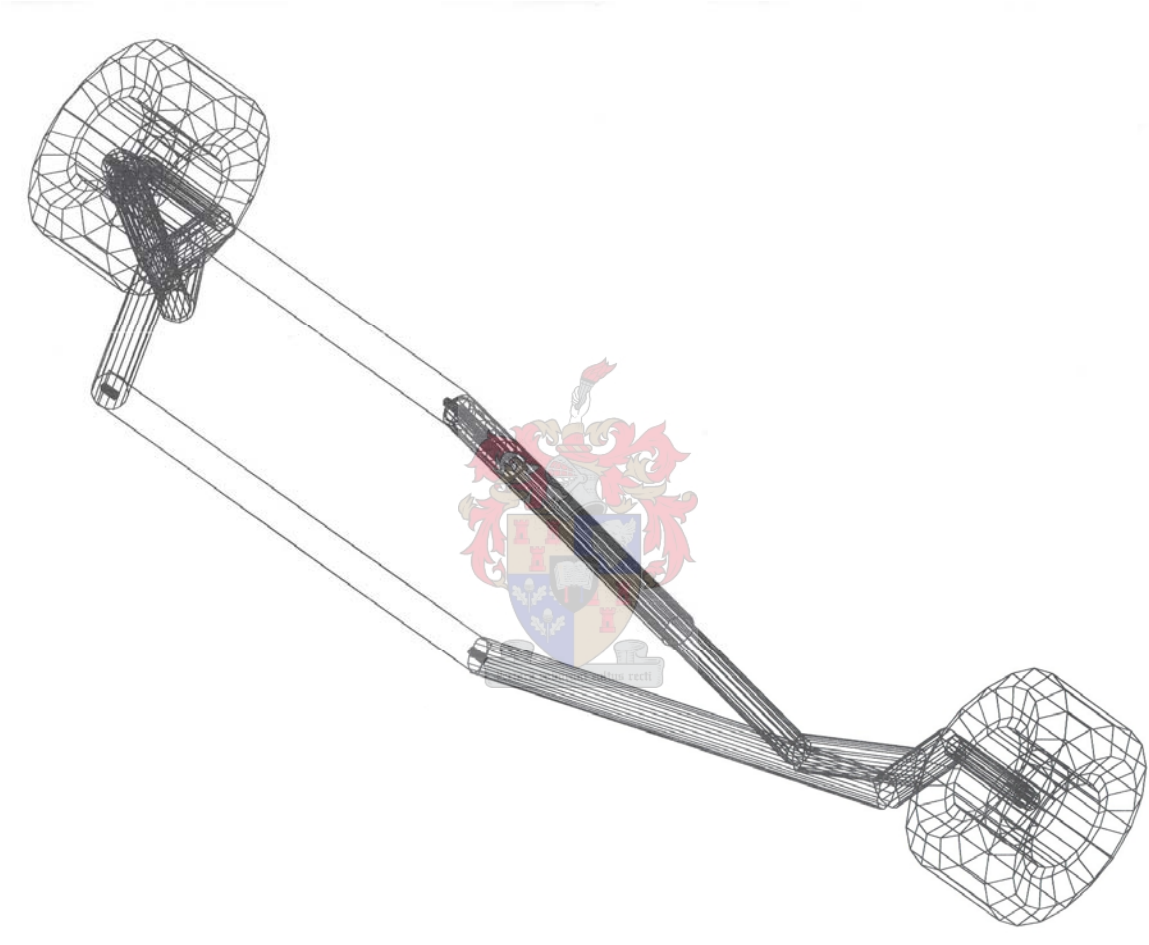
Appendix D

ADAMS Rooivalk Tail Landing Gear Shock Absorber Model



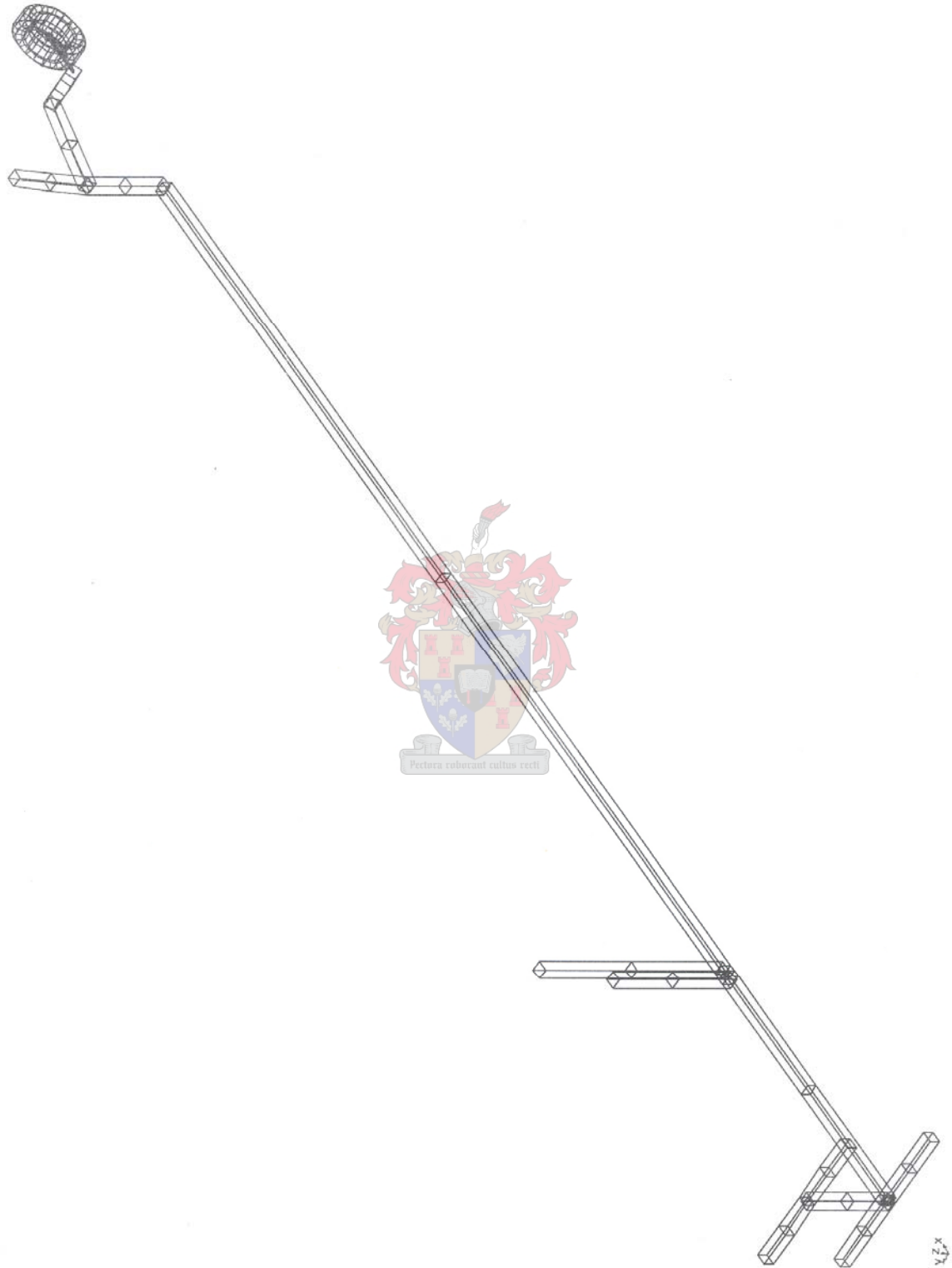
Appendix E

ADAMS Rooivalk Main Landing Gear Structure Model



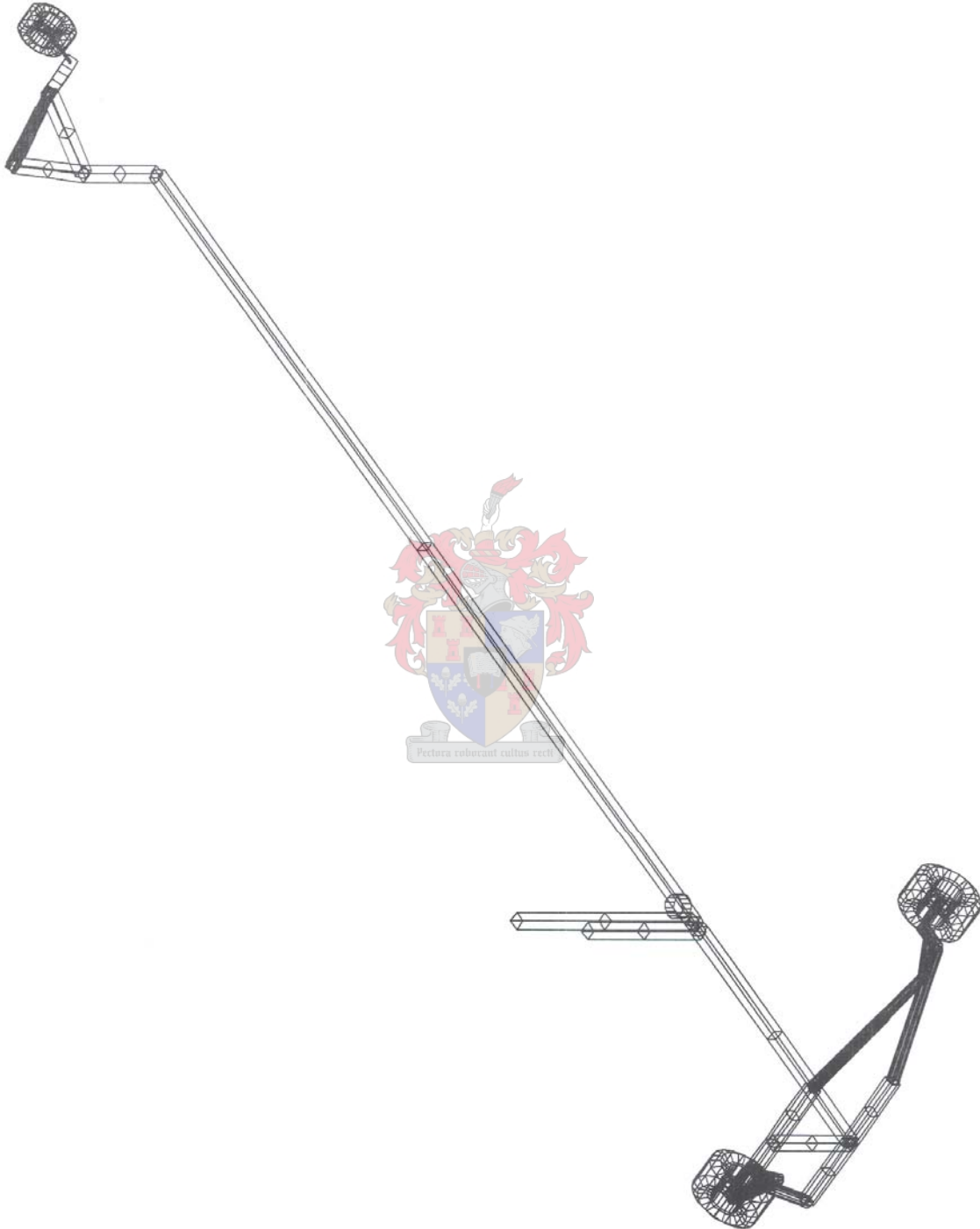
Appendix F

ADAMS Rooivalk Rigid Fuselage with Tail Wheel Assembly Model



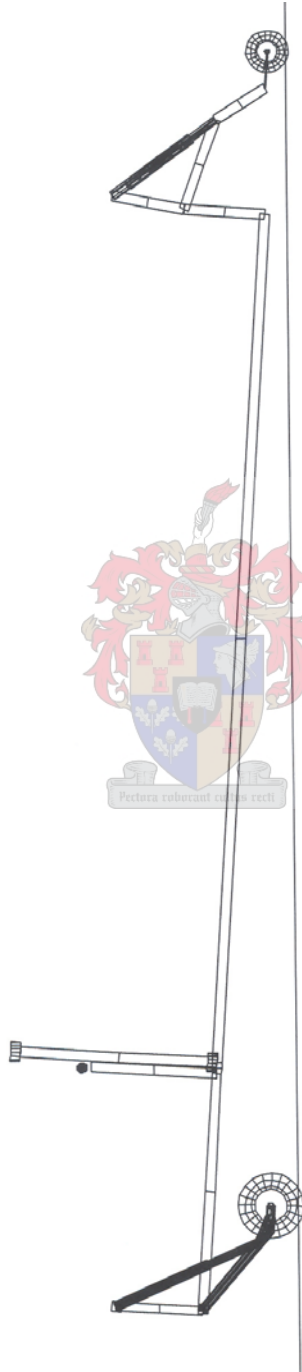
Appendix G

ADAMS Rooivalk Rigid Fuselage Assembly Model




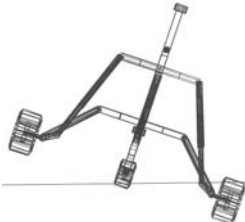

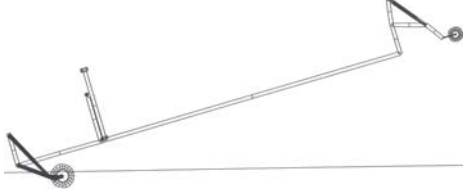
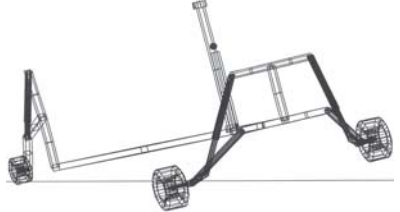
Appendix H

ADAMS Rooivalk Fuselage Model (Rigid Rotor Body) in Equilibrium Configuration



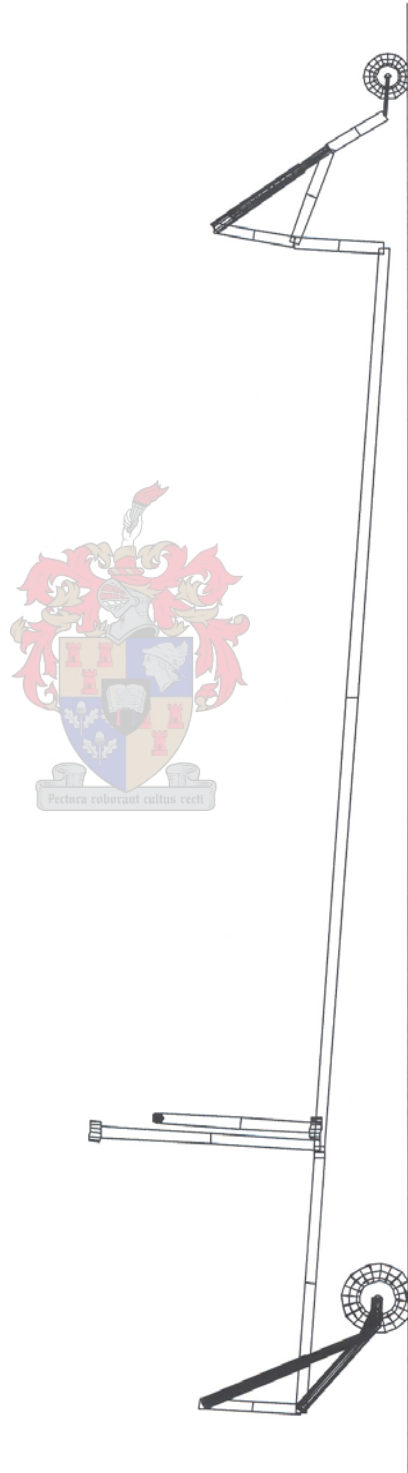
Appendix I

ADAMS Roivalk Fuselage Model Mode Shapes (Data used in DYMORE)

Mode No	Frequency	Mode Shape
1	15.560 rad/sec	
2	18.784 rad/sec	
3	20.099 rad/sec	
4	45.588 rad/sec	
5	1111.213 rad/sec	

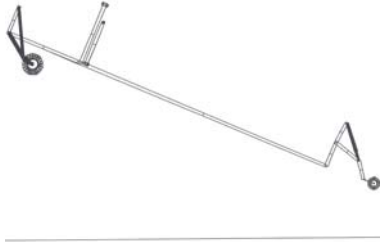
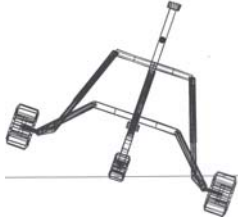
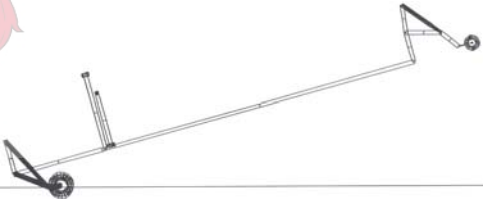
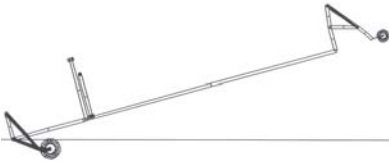
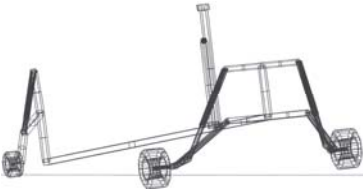
Appendix J

ADAMS Roivalk Fuselage Model in Balance Position (Denel Data)



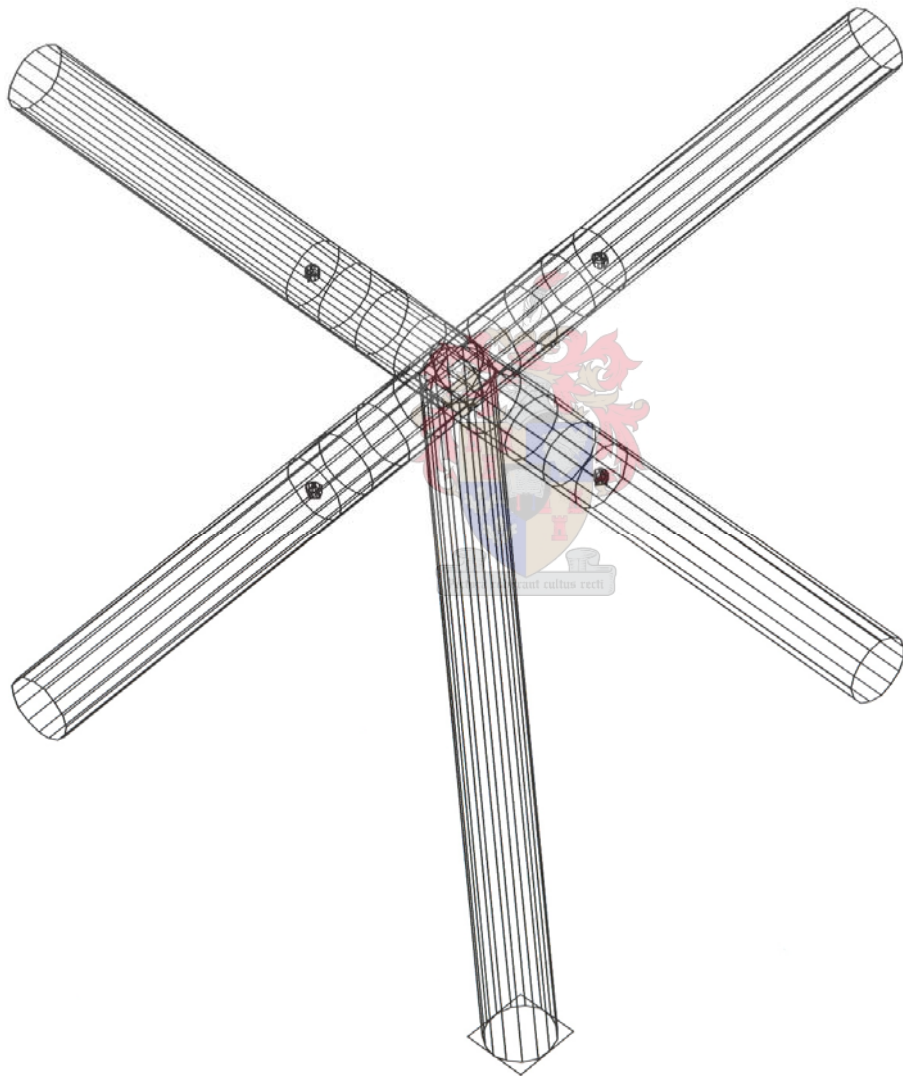
Appendix K

ADAMS Rooivalk Fuselage Model Mode Shapes (Denel Data)

Mode No	Frequency	Mode Shape
1	15.562 rad/sec	
2	17.638 rad/sec	
3	18.613 rad/sec	
4	44.741 rad/sec	
5	1026.899 rad/sec	

Appendix L

MSC ADAMS Main Rotor Hub



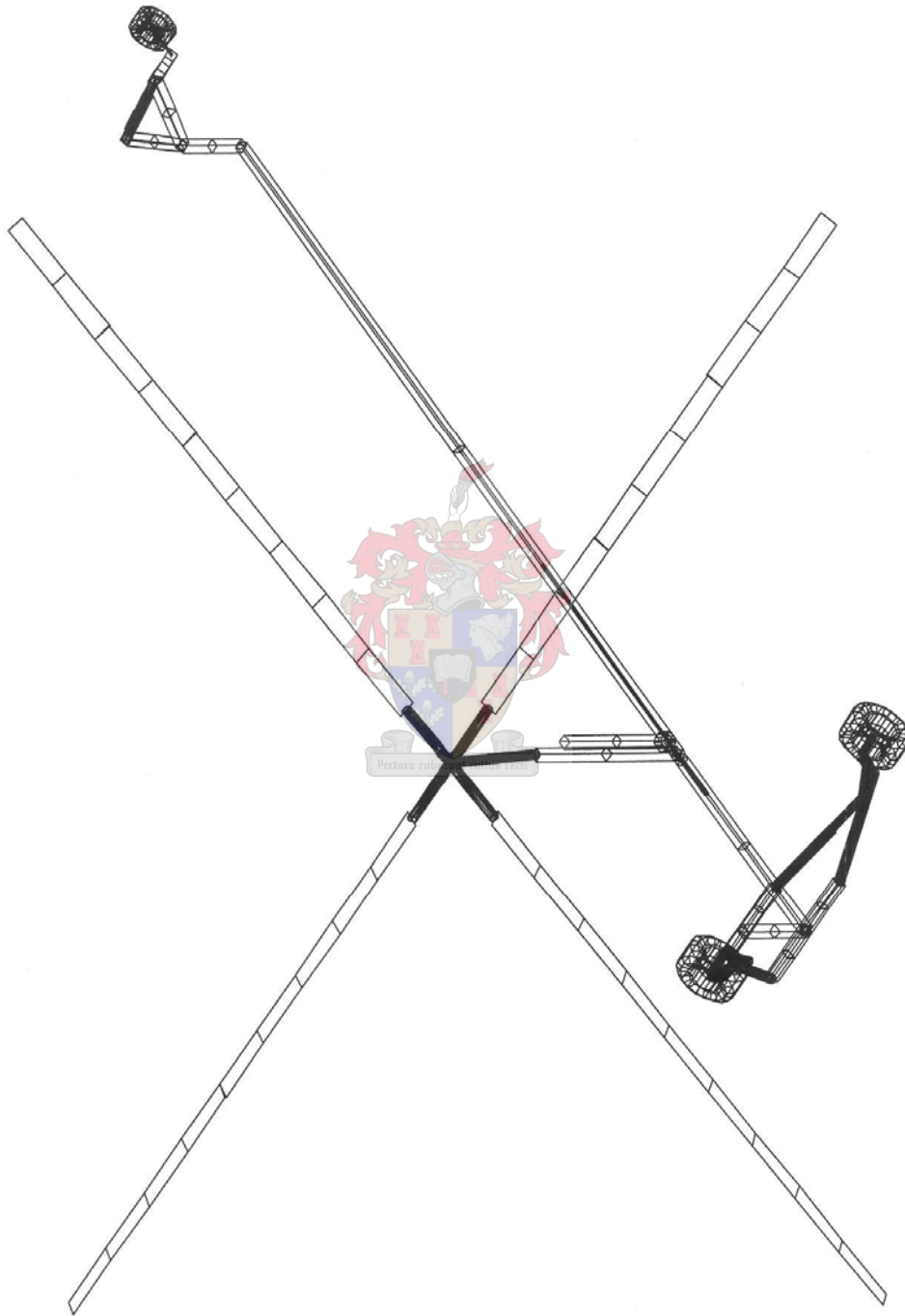
Appendix M

MSC ADAMS Main Rotor



Appendix N

ADAMS AIRCRAFT Roivalk Model

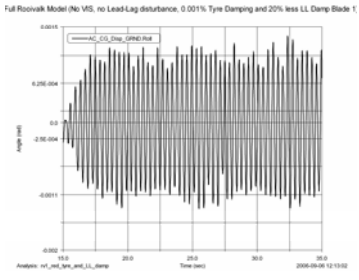
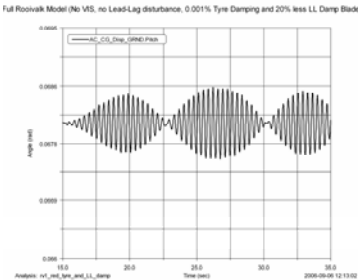
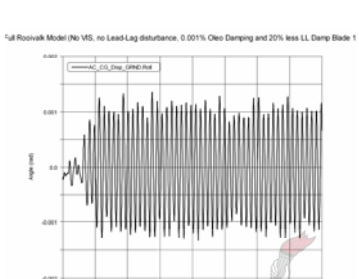
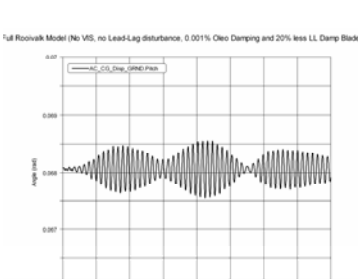
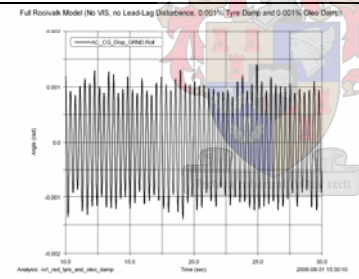
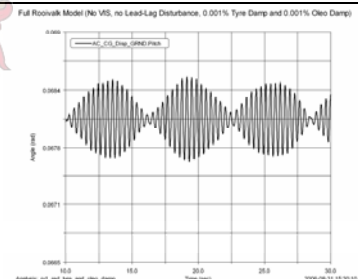
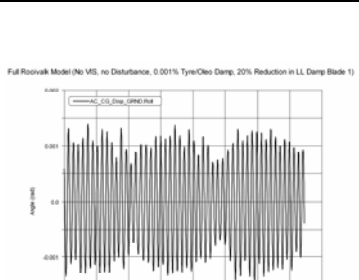
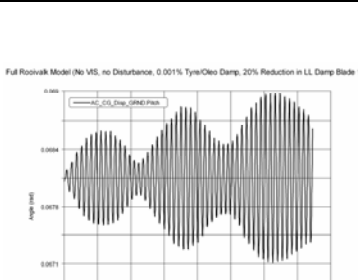


Appendix O

Dynamic Analysis of ADAMS AIRCRAFT Rooivalk Model with Rigid Blades rotating at 275 RPM with no Lead-Lag Disturbance

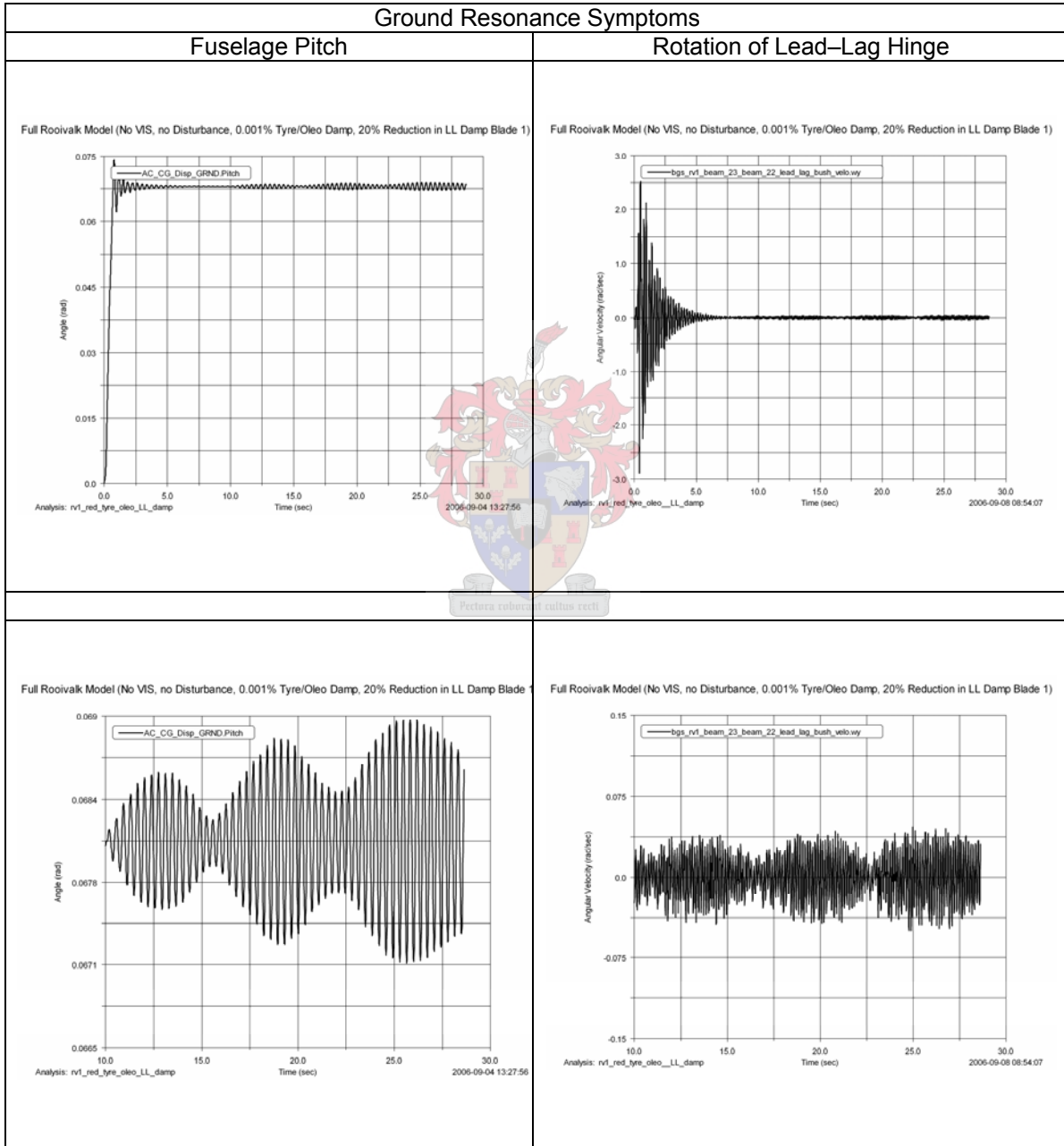
Analysis No	Failure Case	Ground Resonance Symptoms		Comments
		Fuselage Roll	Fuselage Pitch	
1	No VIS			No Ground Resonance Symptoms
2	No VIS, Lead-Lag Damping 20% Reduced			No Ground Resonance Symptoms
3	No VIS, 0.001% Main Landing Gear Shock Absorber Damping			No Ground Resonance Symptoms
4	No VIS, 0.001% Main Landing Gear Tire Damping			No Ground Resonance Symptoms

Analysis No	Failure Case	Ground Resonance Symptoms		Comments
		Fuselage Roll	Fuselage Pitch	
5	No VIS, 0.001% Tail Landing Gear Shock Absorber Damping			No Ground Resonance Symptoms
6	No VIS, 0.001% Tail Landing Gear Tire Damping			No Ground Resonance Symptoms
7	No VIS, 0.001% Main Landing Gear and Tail Landing Gear Tire Damping			No Ground Resonance Symptoms
8	No VIS, 0.001% Main Landing Gear and Tail Landing Gear Shock Absorber Damping			No Ground Resonance Symptoms

Analysis No	Failure Case	Ground Resonance Symptoms		Comments
		Fuselage Roll	Fuselage Pitch	
9	No VIS, 0.001% Total Landing Gear Tire Damping, 20% Decrease in Lead-Lag Damping	 <p>Full Rooivalk Model (No VIS, no Lead-Lag disturbance, 0.001% Tyre Damping and 20% less LL Damp Blade 1)</p>	 <p>Full Rooivalk Model (No VIS, no Lead-Lag disturbance, 0.001% Tyre Damping and 20% less LL Damp Blade 1)</p>	No Ground Resonance Symptoms
10	No VIS, 0.001% Total Landing Gear Shock Absorber Damping, 20% Decrease in Lead-Lag Damping	 <p>Full Rooivalk Model (No VIS, no Lead-Lag disturbance, 0.001% Oleo Damping and 20% less LL Damp Blade 1)</p>	 <p>Full Rooivalk Model (No VIS, no Lead-Lag disturbance, 0.001% Oleo Damping and 20% less LL Damp Blade 1)</p>	No Ground Resonance Symptoms
11	No VIS, 0.001% Total Landing Gear Tire and Shock Absorber Damping	 <p>Full Rooivalk Model (No VIS, no Lead-Lag disturbance, 0.001% Tyre Damp and 0.001% Oleo Damp)</p>	 <p>Full Rooivalk Model (No VIS, no Lead-Lag disturbance, 0.001% Tyre Damp and 0.001% Oleo Damp)</p>	No Ground Resonance Symptoms
12	No VIS, 0.001% Total Landing Gear Tire and Shock Absorber Damping, 20% Decrease in Lead-Lag Damping	 <p>Full Rooivalk Model (No VIS, no Disturbance, 0.001% Tyre/Oleo Damp, 20% Reduction in LL Damp Blade 1)</p>	 <p>Full Rooivalk Model (No VIS, no Disturbance, 0.001% Tyre/Oleo Damp, 20% Reduction in LL Damp Blade 1)</p>	Ground Resonance Symptoms in Pitch

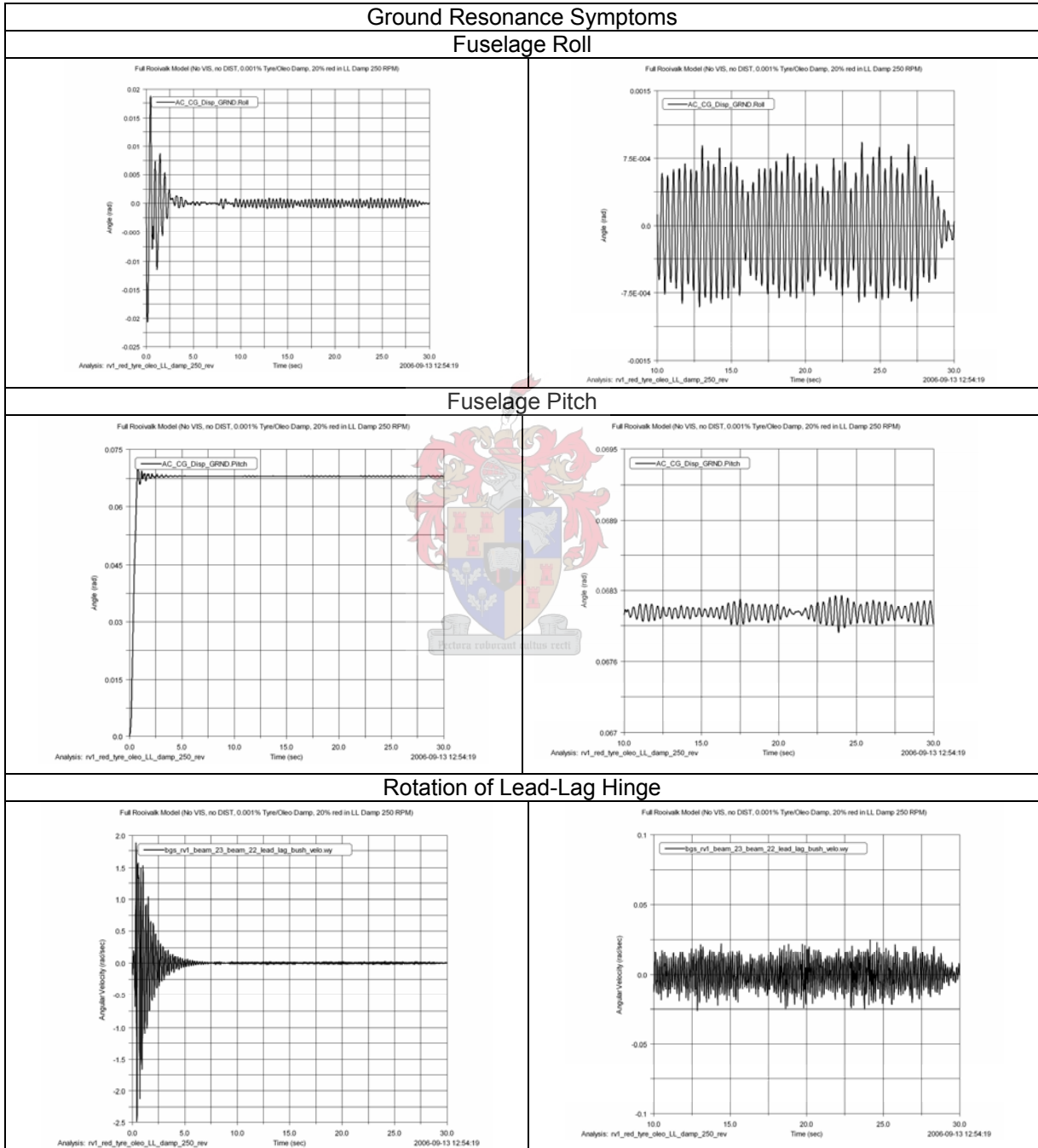
Appendix P

Dynamic Analysis of ADAMS AIRCRAFT Rooivalk Model with Rigid Blades rotating at 275 RPM with no Lead-Lag Disturbance, no VIS, 0.001% Total Landing Gear Tire and Shock Absorber Damping and a 20% Decrease in Lead-Lag Damping



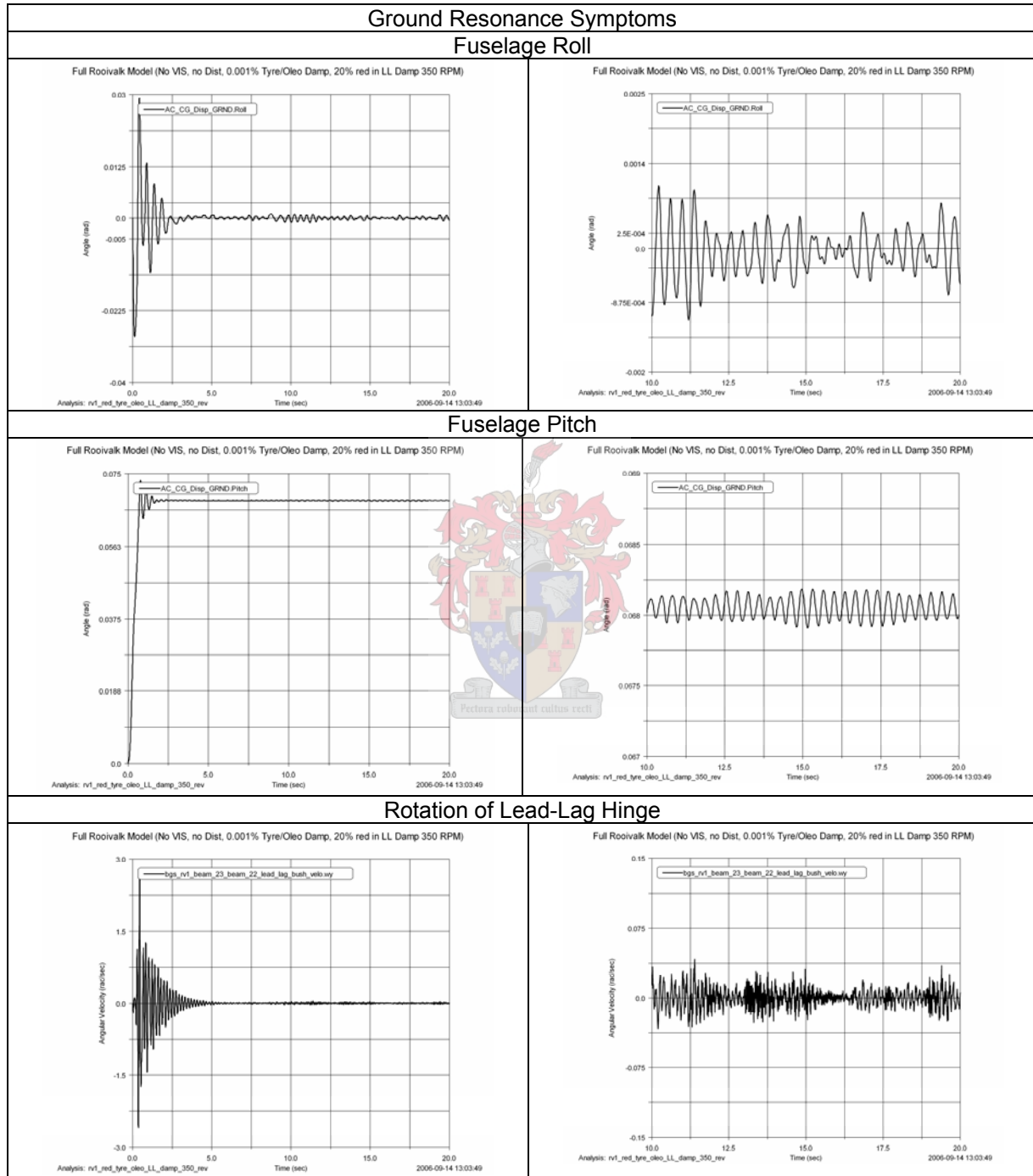
Appendix Q

Dynamic Analysis of ADAMS AIRCRAFT Rooivalk Model with Rigid Blades rotating at 250 RPM with no Lead-Lag Disturbance, no VIS, 0.001% Total Landing Gear Tire and Shock Absorber Damping and a 20% Decrease in Lead-Lag Damping



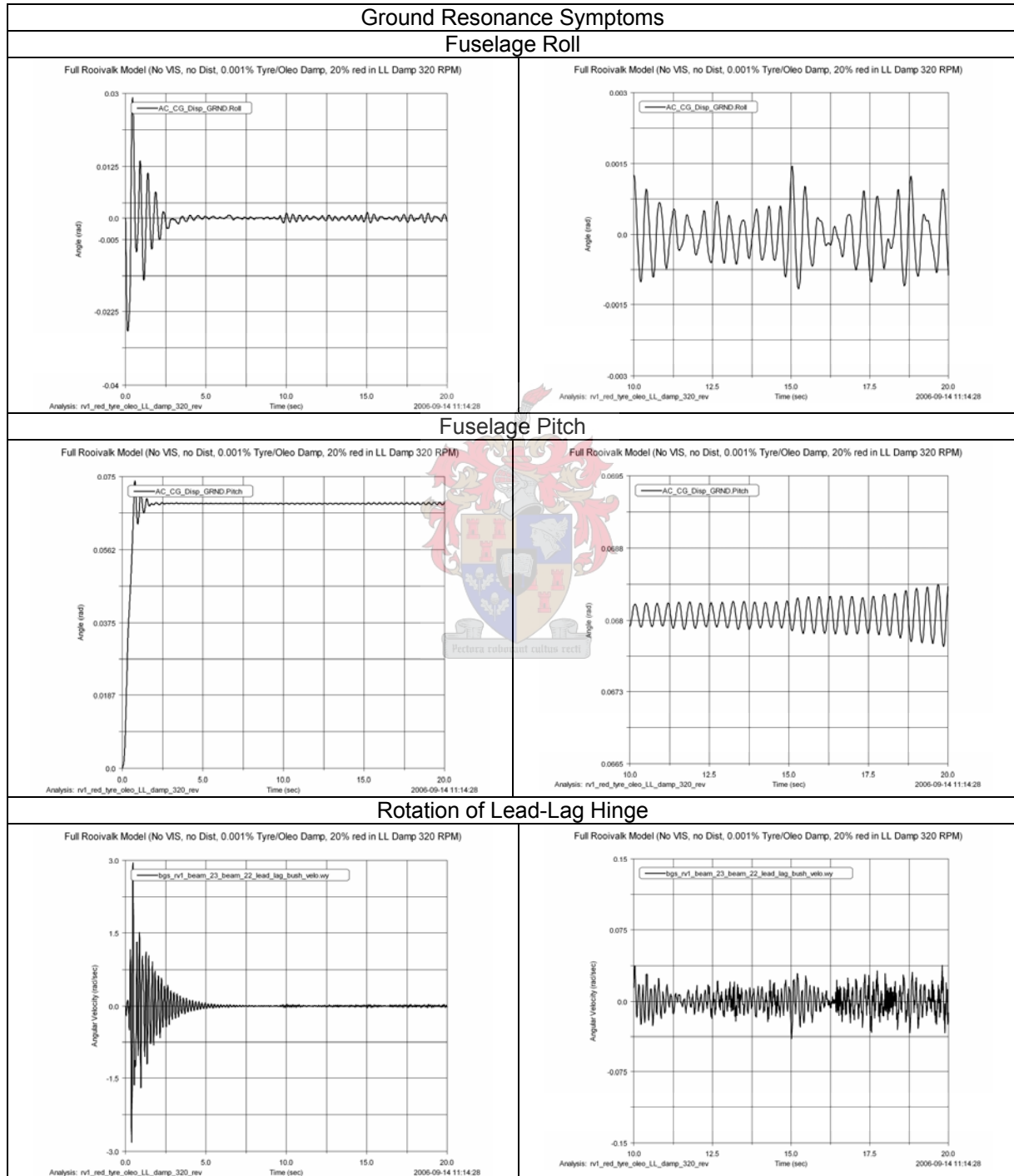
Appendix R

Dynamic Analysis of ADAMS AIRCRAFT Roovalk Model with Rigid Blades rotating at 350 RPM with no Lead-Lag Disturbance, no VIS, 0.001% Total Landing Gear Tire and Shock Absorber Damping and a 20% Decrease in Lead-Lag Damping



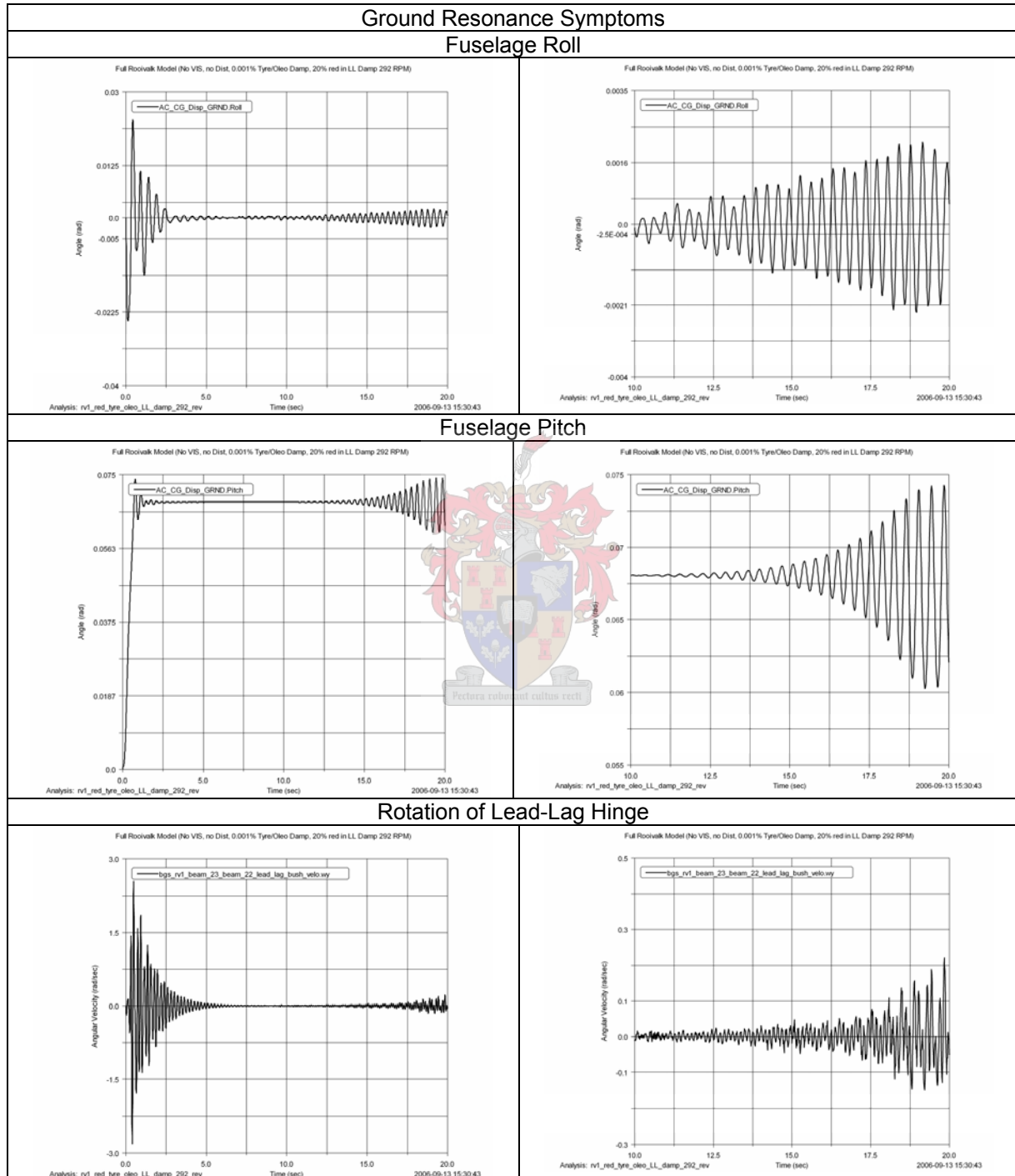
Appendix S

Dynamic Analysis of ADAMS AIRCRAFT Rooivalk Model with Rigid Blades rotating at 320 RPM with no Lead-Lag Disturbance, no VIS, 0.001% Total Landing Gear Tire and Shock Absorber Damping and a 20% Decrease in Lead-Lag Damping



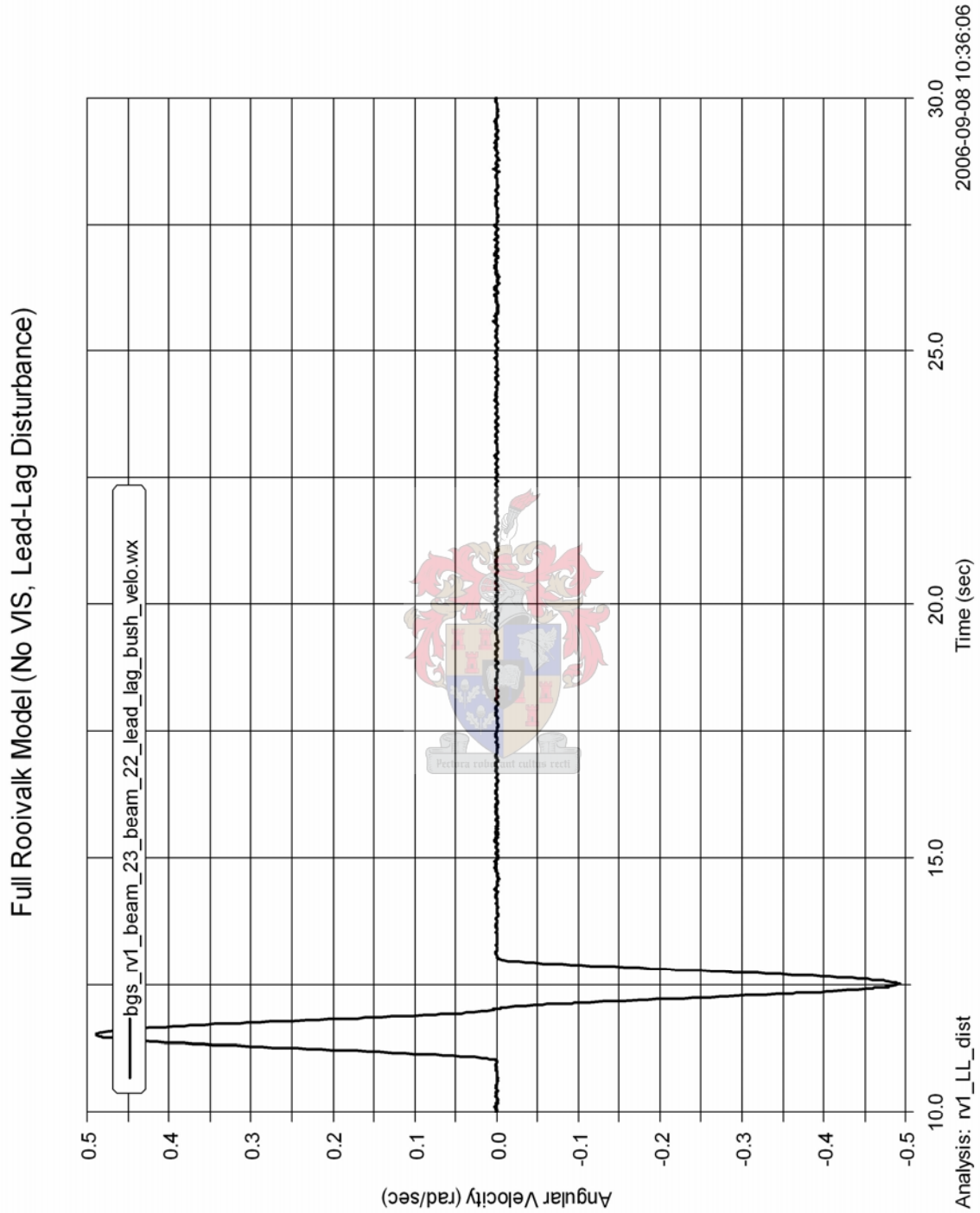
Appendix T

Dynamic Analysis of ADAMS AIRCRAFT Roovalk Model with Rigid Blades rotating at 292 RPM with no Lead-Lag Disturbance, no VIS, 0.001% Total Landing Gear Tire and Shock Absorber Damping and a 20% Decrease in Lead-Lag Damping



Appendix U

Lead-Lag Disturbance of Main Rotor Blade by a 45 kN-meter Point Torque



Appendix V

Dynamic Analysis of ADAMS AIRCRAFT Roovalk Model with Rigid Blades rotating at 275 RPM with a 45 kN-meter Point Torque Lead-Lag Disturbance

Analysis No	Failure Case	Ground Resonance Symptoms		Comments
		Fuselage Roll	Fuselage Pitch	
1	No VIS			No Ground Resonance Symptoms
2	No VIS, Lead-Lag Damping 20% Reduced			No Ground Resonance Symptoms
3	No VIS, 0.001% Main Landing Gear Shock Absorber Damping			No Ground Resonance Symptoms
4	No VIS, 0.001% Main Landing Gear Tire Damping			No Ground Resonance Symptoms

Analysis No	Failure Case	Ground Resonance Symptoms		Comments
		Fuselage Roll	Fuselage Pitch	
5	No VIS, 0.001% Tail Landing Gear Shock Absorber Damping			No Ground Resonance Symptoms
6	No VIS, 0.001% Tail Landing Gear Tire Damping			No Ground Resonance Symptoms
7	No VIS, 0.001% Main Landing Gear and Tail Landing Gear Tire Damping			No Ground Resonance Symptoms
8	No VIS, 0.001% Main Landing Gear and Tail Landing Gear Shock Absorber Damping			No Ground Resonance Symptoms

Analysis No	Failure Case	Ground Resonance Symptoms		Comments
		Fuselage Roll	Fuselage Pitch	
9	No VIS, 0.001% Total Landing Gear Tire Damping, 20% Decrease in Lead-Lag Damping			No Ground Resonance Symptoms
10	No VIS, 0.001% Total Landing Gear Shock Absorber Damping, 20% Decrease in Lead-Lag Damping			No Ground Resonance Symptoms
11	No VIS, 0.001% Total Landing Gear Tire and Shock Absorber Damping			No Ground Resonance Symptoms
12	No VIS, 0.001% Total Landing Gear Tire and Shock Absorber Damping, 20% Decrease in Lead-Lag Damping			Ground Resonance Symptoms in Pitch

Appendix W

Dynamic Analysis of ADAMS AIRCRAFT Rooivalk Model with Rigid Blades rotating at 292 RPM with a Lead-Lag Disturbance of Main Rotor Blade by a 45 kN-meter Point Torque, no VIS, 0.001% Total Landing Gear Tire and Shock Absorber Damping and a 20% Decrease in Lead-Lag Damping

